12-18-2014

Photoionization of Fullerens and Atoms Confined in Fullerenes

Mohammad Hadigheh Javani

PHOTOIONIZATION OF FULLERENS AND ATOMS CONFINED IN FULLERENES

by

MOHAMMAD HADIGHEHJAVANI

Under the Direction of Professor Steven T. Manson

ABSTRACT

The photoionization cross sections of small fullerenes (C_{28}, C_{32}, C_{40}, C_{44}, and C_{50}), and the outer and near-outer shells of atoms (noble gases, alkaline earth) confined endohedrally inside a C_{60} molecule are calculated employing a time-dependent local density approximation formulation. Plasmon and confinement resonances are found to be a general feature of these cross sections, and dramatic interchannel coupling effects, significantly increasing the atomic cross sections, are exhibited in all cases in the vicinity of the C_{60} plasmons. Hybridization effects, the mixing of the atomic and cage bound state wave functions, are also found, but no systematics of the hybridization present themselves. Also, in the case of Ar@C_{60}, Inter-atomic Columbic decay (ICD) has been found and studied.

INDEX WORDS: Photoionization, Noble gas, Fullerene, Endohedrally, TDLDA, ICD

PHOTOIONIZATION OF FULLERENS AND ATOMS CONFINED IN FULLERENES

by

MOHAMMAD HADIGHEHJAVANI

A Dissertation Submitted in Partial Fulfillment of the Requirements for the Degree of

Doctor of Philosophy

in the College of Arts and Sciences

Georgia State University

2014

PHOTOIONIZATION OF FULLERENS AND ATOMS CONFINED IN FULLERENES

by

MOHAMMAD HADIGHEHJAVANI

Committee Chair: Steven T. Manson

Committee: Xiaochun He

Murad Sarsour

Vadym Apalkov

Michael Crenshaw

Electronic Version Approved:

Office of Graduate Studies

College of Arts and Sciences

Georgia State University

December 2014

DEDICATION

I dedicate my dissertation work to my family and many friends. A special feeling of gratitude to my parents, and my lovely wife whose words and prays always encourage and help me in tough situations.

ACKNOWLEDGEMENTS

I would like to gratefully and sincerely thank Dr. Manson for his guidance, understanding, patience, and most importantly, his friendship during my graduate studies at Georgia State University. His mentorship was paramount in providing a well rounded experience consistent my long-term career goals. He encouraged me to not only grow as a theoretical physicist but also as an instructor and an independent thinker. I am not sure many graduate students are given the opportunity to develop their own individuality and self-sufficiency by being allowed to work with such independence. For everything you've done for me, Dr. Manson, I thank you.

TABLE OF CONTENTS

LIST OF TABLES

LIST OF FIGURES

INTRODUCTION

The study of the photoionization of systems composed of atoms entrapped in fullerene molecules, termed endohedral fullerenes [1], is an increasingly active field of inquiry [2,3,4]. From a technological point of view, there is the promise of applications in a wide range of areas, including quantum computing [5], drug delivery [6], photovotaic materials [7], and hydrogen storage [8], to cite a few. In addition, these studies allow us to understand how a trapped atom responds to an external stimulus, in this case the fullerene cage. Most of the investigations that have been performed have been theoretical [2,3,4], but recently experimental studies have been reported [9,10,11].

Theoretical studies have been carried out using several different models for the interaction of the enclosed atom with the surrounding fullerenes [2,4], and these models have been incorporated in a variety of theoretical techniques [2,3,4,12,13,14,15,16,17,18]. A number of different confined systems have been looked at in these various theoretical studies. In this research, we report on a systematic study of the photoionization of the outer and near outer shells of the noble gas atoms (He, Ne, Ar, Kr and Xe), small alkaline earth (Be, Mg, and Ca) confined in the C_{60} fullerene, and also, small fullerenes C_n (n=28, 32, 40, 44, and 50). The aim is to elucidate the similarities and differences of the effects of confinement across the different sets of atoms and fullerenes.

In the following chapters, extensively, discussion of the theory and calculational methodology are presented. Next a detailed account of the results are presented and discussed.

1. COLLISIONS AND PHOTOIONIZATION

1.1 Introduction

One of the methods to probe microscopic quantum system is through collisions, and we can explore some of the properties of such systems by this method. Atoms, ions, molecules, and clusters are

microscopic quantum systems; atoms are the simplest types of these systems. We need tools to probe these microscopic quantum systems which can be electromagnetic radiation,$h\nu$, particles such as e^-, e^+, n, α, atom, ion, or molecule. If we investigate the system by light, it is called spectroscopy, and the term collisions is used when the system is studied by bombarding with particles. And the important question is that, "if there is any relation between spectroscopy and collisions?"

Consider a system in an excited state; it can decay through a radiative channel and emit light. A quantum system can also absorb the light, and the result of this absorption can be the excitation of the quantum system, or transition to continuum states of the system that is called photoionization. In some cases a bound to bound transition can take place at the same energy as a bound to continuum transition, and in such cases we have resonance.

The "probability" of photoelectron emission, or a bound to continuum transition, is generally known as the photoionization cross section. The direction of the photoelectron with respect to the direction of the incident electromagnetic radiation and the direction of the polarization of the light can be measured, and it is called as angular distribution. By measuring these two properties we have the complete set of compatible observables for photoelectron process. This is now a very powerful tool which is called as "photoelectron spectroscopy" to study condensed matter and surface analyses.

Generally, what we are doing is measuring the transition matrix element,$\langle\psi_f|T|\psi_i\rangle, where\ T$ is the transition matrix operator that is the physical interaction between the quantum system and the probe that is responsible for this transition. The main questions are how the initial and final states are described, and also how the interaction is represented. In quantum systems we cannot have exact solution for that, so in order to have solution for these quantum systems, one has to make approximations for all of them, such as, initial states, final states, and transition operator. All these processes are done to find the value of the matrix elements which will be a measure of the probability amplitude, and the square of that gives the transition probability.

Now to answer the question that how the photoionization and scattering are related to each other, we should take a close look at each of the processes individually,

Photoionization: In photoionization process the photon or electromagnetic wave is absorbed by the target (the simplest target is an atom) and an excited state is formed; a continuum state consisting of an ion and an electron,

$$h\nu + A \rightarrow e + A^{+}. \quad \textbf{(1.1)}$$

Electron-ion scattering/Radiative recombination: Radiative recombination is the electron-ion scattering process that is the inverse process of photoionization. An electron impinges on a positive ion and recombines to form a neutral target, with the excess energy being emitted in the form of a photon,

$$e + A^{+} \rightarrow h\nu + A. \quad \textbf{(1.2)}$$

A related process is electron-ion elastic scattering,

$$e + A^{+} \rightarrow e + A^{+}. \quad \textbf{(1.3)}$$

In this process, the initial state is completely different from the initial state of the photoionization process, but the final states can be exactly the same. So how are these two processes related?

In order to find the relation between photoionization and elastic electron-ion scattering we need to investigate symmetry in atomic processes, which in this case the symmetry is time reversal symmetry. In electron-ion scattering, a beam of mono-energetic electrons is shot at an ion, as a target, so the position of the target and the direction of the electron beam are known, in other words the entrance channel is unique. The scattered particles could go essentially in any direction, although the probabilities of finding particles in any direction are not the same. While in photoionization an atom has absorbed photon and knocked out an electron in to the continuum, and this electron is detected by detector. Therefore we have unique direction for the photoelectron, or the exit channel is unique. So, the boundary conditions for scattering and photoionization are different.

For photoionization, the boundary condition is called the *ingoing* boundary condition, where we have an outgoing plane wave in a specified direction representing the photoelectron. On the other hand, relevant to electron-ion collisions, there are *outgoing* boundary conditions which describes as a plane wave, an incident electron in a specified direction. First we will talk about collisions, and then, using time reversal symmetry we can easily have photoionization formalism.

1.2 Collisions (scattering)

Incident mono-energetic electrons are represented by plane waves and the asymptotic wave function, including the scattering, is [19]

$$\psi_{\vec{k}_i}(\vec{r}; r \to \infty) \to A\left[e^{i\vec{k}.\vec{r}} + \frac{f(\hat{\Omega})}{r} e^{ikr}\right]. \quad \textbf{(1.4)}$$

Because in the time-dependent Schrödinger equation the stationary states are represented by $e^{-i\omega t}$, the net phase for spherical wave is $(kr - \omega t)$, so the surface of constant phase propagates outward since

$$\delta(kr - \omega t) = 0 \ \to \ \frac{\delta r}{\delta t} = \frac{\omega}{k} > 0 \ , \quad \textbf{(1.5)}$$

the scattering wave functions can be represented by a sum of products of radial wave functions and spherical harmonics of the form

$$R_{k,l}\, Y_{lm}\,(\theta, \phi), \quad \textbf{(1.6)}$$

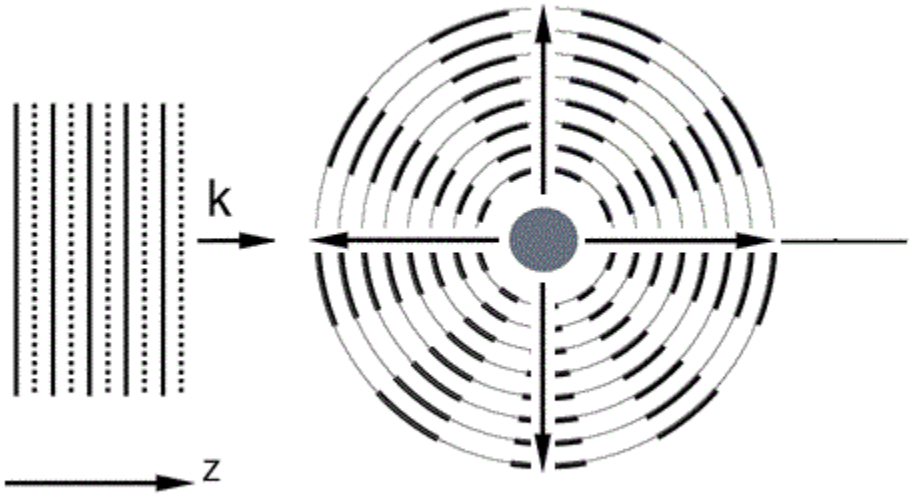

Figure1.1 Outgoing wave boundary conditions relevant to scattering

with the radial wave functions governed by

$$R'' + \frac{2}{r}R' - \frac{l(l+1)}{r^2}R + \frac{2\mu}{\hbar^2}[E - V(r)]R = 0\,. \tag{1.7}$$

If $R_{k,l} = \frac{y_{k,l}}{r}$ the differential equation can be written as,

$$\left[-\frac{\hbar^2}{2m}\frac{d^2}{dr^2} + \left\{V(r) + \frac{l(l+1)}{2mr^2}\right\} - E\right] y_{k,l}(r) = 0\,. \tag{1.8}$$

To get an idea how to solve the complete differential equation, let's solve the differential equation for two special cases. First, since we know the solution for $V(r) = 0$ (that can be considered as a spherical potential), which is the free particle or plane wave,

$$V(r) = 0 \;\rightarrow \left[-\frac{\hbar^2}{2m}\frac{d^2}{dr^2} + \left\{\frac{l(l+1)}{2mr^2}\right\} - E\right] y_{k,l}(r) = 0\,. \tag{1.9}$$

Second, if $l = 0$, the s-wave case,

$$l = 0\,, \left[-\frac{\hbar^2}{2m}\frac{d^2}{dr^2} - E\right] y_{k,l=0}(r) = 0\,, \tag{1.10}$$

$$l = 0\,, \left[\frac{d^2}{dr^2} + k^2\right] y_{k,l=0}(r) = 0 \quad where \quad k = \frac{\sqrt{2mE}}{\hbar}\,. \tag{1.11}$$

The solution is

$$y_{k,l=0}(r) = rR_{k,l=0}(r) = Ne^{\pm ikr}\,, \tag{1.12}$$

$$R_{k,l=0}(r) = N\frac{e^{\pm ikr}}{r} \rightarrow N\frac{\sin(kr)}{r}.$$

Since $\frac{\cos(kr)}{r}$ is undefined when $\rightarrow 0$, we pick the sin part only, and the normalization constant will be $\sqrt{2/\pi}$, so

$$R_{k,l=0}(r) = \sqrt{2/\pi}\frac{\sin(kr)}{r}\,. \tag{1.13}$$

This is the s-wave (*l*=0) solution for the free particle (*V*=0). Then, we have to go from special case to general case,

$$R'' + \frac{2}{r}R' - \frac{l(l+1)}{r^2}R + \frac{2\mu}{r^2}[E - V(r)]R = 0. \tag{1.14}$$

Again the radial equation for free particle is:

$$V(r) = 0 \rightarrow R'' + \frac{2}{r}R' + \left\{k^2 - \frac{l(l+1)}{r^2}\right\}R(r) = 0 \quad , \quad k = \frac{\sqrt{2mE}}{\hbar}\,, \tag{1.15}$$

for all values of *l* including *l*=0. If we consider the solution for the radial differential equation of the free particle to be

$$R_{k,l}(r) = N\,r^l\,\xi_{k,l}(r)\,, \tag{1.16}$$

then, substituting in the above equation,

$$\xi''_{k,l}(r) + (2l+1)r^{-1}\xi'_{k,l}(r) + k^2\xi_{k,l}(r) = 0\,. \tag{1.17}$$

Now, by making one more differentiation with respect to r, the recursion relation is

$$\xi'_{k,l}(r) = -r\,\xi_{k,l+1}(r). \tag{1.18}$$

So, by having the solution for *l*=0, the solutions for the higher values of *l* can be calculated.

In other words, we can introduce an operator that can calculate the solution for any *l*,

$$\xi_{k,l+1} = -\frac{1}{r}\frac{d}{dr}\xi_{k,l} \rightarrow \xi_{k,l} = \left(-\frac{1}{r}\frac{d}{dr}\right)^{l}\xi_{k,0} \ . \quad \textbf{(1.19)}$$

The solution for l=0 is

$$R_{n,l=0}(r) = \sqrt{2/\pi}\frac{\sin(kr)}{r} \rightarrow \xi_{k,0} = \frac{R_{n,0}}{N} = \sqrt{2/\pi}\frac{sin(kr)}{rN} \ , \quad \textbf{(1.20)}$$

and the solution for any value of l is

$$\xi_{k,l} = \left(\frac{1}{r}\frac{d}{dr}\right)^{l}\xi_{k,0} \rightarrow \xi_{k,l} = \left(\frac{1}{r}\frac{d}{dr}\right)^{l}\sqrt{2/\pi}\frac{Sin(kr)}{rN} \ , \quad \textbf{(1.21)}$$

$$R_{k,l}(r) = \sqrt{2/\pi}\ \frac{(-1)^{l}}{k^{l}}r^{l}\ \left(\frac{1}{r}\frac{d}{dr}\right)^{l}\frac{Sin(kr)}{r} \quad l = 0,1,2,\dots \ , \quad \textbf{(1.22)}$$

$$\frac{1}{r}\frac{d}{dr}\left(\frac{Sin(kr)}{r}\right) = \frac{1}{r}\left(\frac{k\,cos(kr)}{r} - \frac{sin(kr)}{r^{2}}\right) . \quad \textbf{(1.23)}$$

Asymptotically ($r \rightarrow \infty$), the second term vanishes,

$$\frac{1}{r}\frac{d}{dr}\left(\frac{Sin(kr)}{r}\right) \sim \frac{1}{r}\frac{k\,cos(kr)}{r} = \frac{k\ sin\ (\frac{\pi}{2} - kr)}{r^{2}} = \frac{(-1)k\ sin\ (kr - \frac{\pi}{2})}{r^{2}} \ . \quad \textbf{(1.24)}$$

Since the effect of the operator $\frac{1}{r}\frac{d}{dr}$ is known, to get the l^{th} solution we have to do it l times, so the asymptotic radial solution for V=0 (special case of spherical symmetry) and any value of l is

$$R_{k,l}(r) = \frac{\sqrt{2/\pi}k\ sin\ (kr - l\frac{\pi}{2})}{r} , \quad \textbf{(1.25)}$$

i.e., the non-zero angular momentum gives the asymptotic solution a phase shift with respect to the *l=0* solution.

But what if we have spherical potential not equal to zero? If V≠0 the arguments inside parentheses have further shifted by another phase shift $\delta_l(k)$ which will depend on orbital angular momentum quantum number, l, and energy, k. It is called scattering phase shift, and since this quantity is the only part of the solution that carries the effect of potential, all the physical information about the collision dynamics will be contained in it. For more information, see Appendix A.

For the case that has shown in figure1.1 the asymptotic scattering solution (1.3) can be expanded in spherical waves. We can expand $e^{i\vec{k}.\vec{r}}$ in spherical harmonics as

$$e^{i\vec{k}.\vec{r}} = \sum_{l=0}^{\infty} \sum_{m=-l}^{+l} c_{l,m} Y_l^m(\theta,\phi) j_l(kr). \quad \textbf{(1.26)}$$

If we chose $\vec{k}$ to be in the z-direction, which makes sense owing to the azimuthally symmetry of the problem, $e^{i\vec{k}.\vec{r}} = e^{ikrcos\theta} = e^{i\rho\mu}$, where $\rho = kr$, and $\mu = cos\theta$, so that

$$e^{i\rho\mu} = \sum_{l=0}^{\infty} \sum_{m=-l}^{+l} a_l P_l(\mu) j_l(\rho)\,. \quad \textbf{(1.27)}$$

We know the solution for radial part $R_{k,l}(r) = \frac{\sqrt{2/\pi}k\ sin\ (kr - l\frac{\pi}{2} + \delta_l(k))}{r}$ and angular part, $P_l(\mu)$, so the only thing that should be determined the coefficient a_l. To calculate this coefficient the orthogonality relation of the $P_l(\mu)$ is used,

$$\int_{-1}^{1} e^{i\rho\mu}\, P_{l'}(\mu) d\mu = \sum_{l=0}^{\infty} a_l \left[\int_{-1}^{1} P_l(\mu) P_{l'}(\mu) d\mu\right] j_l(\rho)\,,$$

$$\int_{-1}^{1} e^{i\rho\mu}\, P_l(\mu) d\mu = a_l \left[\frac{2}{2l+1}\right] j_l(\rho)\,, \quad \textbf{(1.28)}$$

which can be integrated by parts to obtain,

$$\int_{-1}^{1} e^{i\rho\mu} P_l(\mu) d\mu = \frac{e^{i\rho} - (-1)^l e^{-i\rho}}{i\rho} - O(\rho^2) \sim \frac{e^{i\rho} - 1}{i\rho} l e^{-i\rho} i\rho = \frac{e^{i\rho} - (e^{i\pi})^l e^{-i\rho}}{i\rho}$$

$$= e^{i\frac{\pi}{2}} \left[\frac{e^{i\rho} e^{-il\frac{\pi}{2}} - e^{il\frac{\pi}{2}} e^{-i\rho}}{i\rho}\right] = i^l \left[\frac{e^{i\rho} e^{-il\frac{\pi}{2}} - e^{il\frac{\pi}{2}} e^{-i\rho}}{i\rho}\right] = i^l \left[\frac{2i\ sin\left(\rho - \frac{l\pi}{2}\right)}{i\rho}\right], \quad \textbf{(1.29)}$$

and by knowing the asymptotic form of spherical Bessel function, the coefficient a_l can be determined,

$$j_l(\rho \to \infty) = \frac{\sin(\rho - \frac{l\pi}{2})}{\rho}\,, \quad \textbf{(1.30)}$$

$$a_{l=} i^l (2l+1). \quad \textbf{(1.31)}$$

So that

$$e^{i\rho\mu} = \sum_{l=0}^{\infty} i^l(2l+1)P_l(\mu)j_l(\rho) = \sum_{l=0}^{\infty} i^l(2l+1)P_l(cos\theta)j_l(kr). \quad \textbf{(1.32)}$$

By using the identity

$$P_l(\vec{u}.\vec{v}) = \frac{4\pi}{2l+1}\sum_{m=-l}^{+l} Y_{l,m}^*(\vec{v})Y_{l,m}(\vec{u}), \quad \textbf{(1.33)}$$

the equation (1.32) can be written as

$$e^{i\vec{k}.\vec{r}} = 4\pi\sum_{l=0}^{\infty} i^l\, j_l(kr)\left[\sum_{m=-l}^{+l} Y_{l,m}^*(\hat{k})Y_{l,m}(\hat{e}_r)\right], \quad \textbf{(1.34)}$$

which is the first part of the asymptotic relation of scattering (1.3). We know that we can use Schrödinger equation for solving scattering problem therefore

$$H\psi_{\vec{k}}(\vec{r}) = E\psi_{\vec{k}}(\vec{r}) = \frac{\hbar^2k^2}{2m}\psi_{\vec{k}}(\vec{r});\;\; E>0\,, \quad \textbf{(1.35)}$$

and the solution for (1.35) is

$$\psi_{\vec{k}}(\vec{r}) = \sum_{l=0}^{\infty}\sum_{m=-l}^{+l} c_{l,m}(k)Y_{l,m}(\hat{e}_r)R_{l,m}(k,r). \quad \textbf{(1.36)}$$

These two ways of writing the solution, (1.3) and (1.36) are the equal, so that we can write

$$\psi_{\vec{k}}(\vec{r}; r\to\infty) \to A\left[\sum_{l=0}^{\infty} i^l(2l+1)P_l(cos\theta)j_l(kr) + \frac{f(\Omega)}{r}e^{ikr}\right] =$$

$$A\left[\sum_{l=0}^{\infty}\sum_{m=-l}^{+l} i^l(2l+1)\left\{\sqrt{\frac{4\pi}{2l+1}}Y_{l,m}(\theta)\delta_{m,0}\right\}\frac{\sin\left(kr-\frac{l\pi}{2}\right)}{kr} + \frac{f(\Omega)}{r}e^{ikr}\right]$$

$$= A\left[\sum_{l=0}^{\infty}\sum_{m=-l}^{+l} i^l\sqrt{4\pi(2l+1)}Y_{l,m}(\theta)\delta_{m,0}\frac{e^{i(kr-\frac{l\pi}{2})} - e^{-i(kr-\frac{l\pi}{2})}}{2ikr} + \frac{f(\Omega)}{r}e^{ikr}\right]. \quad \textbf{(1.37)}$$

In equation (1.36) the radial part is the solution of radial Schrödinger equation (1.14), and for the asymptotic region with the potential the solution is

$$R_l(k, r \to \infty) \to A_l(k)\frac{sin\left[kr-\frac{l\pi}{2}+\delta_l(k)\right]}{r} =$$

$$\sum_{l=0}^{\infty}\sum_{m=-l}^{+l} c_{l,m}(k)A_l(k)\frac{e^{i(kr-\frac{l\pi}{2}+\delta_l(k))} - e^{-i(kr-\frac{l\pi}{2}+\delta_l(k))}}{2ir}Y_{l,m}(\hat{e}_r). \quad \textbf{(1.38)}$$

Then equating coefficients of e^{-ikr} in (1.37) and (1.38), we find

$$c_{l,m}(k) = \frac{A(k)}{kA_l(k)}i^l\sqrt{4\pi(2l+1)}e^{+i\delta_l(k)}\delta_{m0}\,. \quad \textbf{(1.39)}$$

If this coefficient is substituted in (1.38) then the scattering amplitude can be easily calculated as a function of $\delta_l(k)$

$$f(k,\theta) = \frac{1}{2ik}\sum_{l=0}^{\infty}(2l+1)\left[e^{2i\delta_l(k)}-1\right]P_l(cos\theta)\,. \quad \textbf{(1.40)}$$

1.2.1 Boundary conditions

Scattering boundary conditions

For scattering, the incident wave is given by

$$\psi_{inc}(\vec{r}; r \to \infty) \to \sum_l i^l(2l+1)P_l(cos\theta)\frac{\sin\left(kr-\frac{l\pi}{2}\right)}{kr}, \quad \textbf{(1.41)}$$

$$\psi_{inc}(\vec{r}; r \to \infty) \to \sum_l i^l(2l+1)P_l(cos\theta)\frac{e^{\mathrm{i}\left(kr-\frac{l\pi}{2}\right)} - e^{-\mathrm{i}\left(kr-\frac{l\pi}{2}\right)}}{2ikr}, \quad \textbf{(1.42)}$$

$$\psi_{inc}(\vec{r}; r \to \infty) \to \sum_l (2l+1)P_l(cos\theta)\frac{e^{ikr} - e^{-\mathrm{i}kr}(-1)^l}{2ikr}. \quad \textbf{(1.43)}$$

Then, we can write the incident wave as

$$\psi_{inc}(\vec{r}; r \to \infty) \to \frac{1}{2ikr}\sum_l (2l+1)\left[P_l(cos\theta)e^{ikr} - P_l(-cos\theta)e^{-ikr}\right]. \quad \textbf{(1.44)}$$

The total wave function, which is the sum of the incident wave and the scattered wave, can be written in the same format as (1.44), but with the scattering phase shift; therefore, the total wave function is

$$\psi_{total} = \psi_{incident} + \psi_{scattered},$$ **(1.45)**

$$\psi_{total}(\vec{r}; r \to \infty) \to \frac{1}{2ikr}\sum_{l} c_l(2l+1)\left[P_l(cos\theta)e^{i(kr+\delta_l)} - P_l(-cos\theta)e^{-i(kr+\delta_l)}\right].$$ **(1.46)**

The question is that what the coefficients c_l are, or what is the boundary condition by which c_l can be determined? If the incident wave function (1.44) is subtracted from total wave function (1.46) the scattered wave function will be the result and from that the c_l can be calculated,

$$\begin{aligned}\psi_{scattered} &= \psi_{total} - \psi_{incident} \\ &= \frac{1}{2ikr}\sum_{l}(2l+1)P_l(cos\theta)e^{ikr}\left(1 - c_l e^{i\delta_l}\right) + (2l+1)P_l(-cos\theta)e^{-ikr}\,(1 \\ &\quad - c_l e^{i\delta_l})\ .\end{aligned}$$ **(1.47)**

Also we can get scattered wave function by substituting the scattering amplitude (1.40) in

$$\psi_{scattered} = \left(\frac{f(\Omega)}{r}\right)e^{ikr},$$ **(1.48)**

$$\psi_{scattered} = \left(\frac{e^{ikr}}{r}\right)\left[\frac{1}{2ik}\sum_{l=0}^{\infty}(2l+1)\left[e^{2i\delta_l(k)} - 1\right]P_l(cos\theta)\right].$$ **(1.49)**

And by comparing (1.47) and (1.49) the coefficient c_l can be determined as

$$c_l = e^{i\delta_l}.$$ **(1.50)**

This is the solution with outgoing wave boundary conditions,

$$\begin{aligned}&\psi_{total}(\vec{r}; r \to \infty) \to \tfrac{1}{2ikr}\textstyle\sum_l e^{i\delta_l}(2l+1)\left[P_l(cos\theta)e^{i(kr+\delta_l)} - P_l(-cos\theta)e^{-i(kr+\delta_l)}\right] = \\ &\frac{1}{2ikr}\sum_{l}(2l+1)\left[P_l(cos\theta)e^{ikr} - P_l(-cos\theta)e^{-ikr}\right] \\ &\quad + \frac{e^{ikr}}{r}\left\{\frac{1}{2ik}\sum_{l=0}^{\infty}(2l+1)\left[e^{2i\delta_l(k)} - 1\right]P_l(cos\theta)\right\},\end{aligned}$$ **(1.51)**

and the time dependent total wave function is

$$\psi_{\vec{k}}(\vec{r}; r \to \infty, t) \to A\left[e^{i\vec{k}.\vec{r}} + \frac{f(\Omega)}{r}e^{ikr}\right]e^{-i\omega t}, \qquad \omega = \frac{E}{\hbar}.$$ **(1.52)**

This solution includes a plane wave is in the z direction plus outgoing spherical waves.

Photoionization boundary conditions

As seen in figure1.2, for photoionization, in this case an atomic system, absorbs electromagnetic radiation, a photon, and ejects a photoelectron in a continuum state. In this situation, the exit channel is unique and we have no net flux of electrons prior to the absorption of the photon. This final state wave function for the photoionization process is almost exactly the same as scattering wave function but with time reversal. This suggests that we can make a connection between these two processes with time reversal symmetry.

In classical mechanics, the equations of motion are symmetric with respect to $t \rightarrow -t$. In other words, the laws of classical mechanics work equally well under the transformation $t \rightarrow -t$ and this is known as time reversal symmetry. But now, what is time reversal symmetry in quantum mechanics?

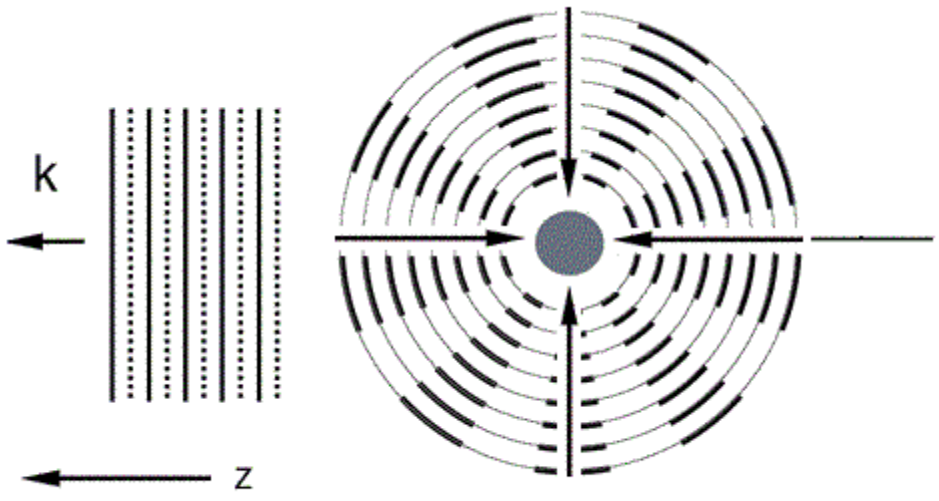

Figure 1.2 Incoming wave boundary conditions relevant to photoionization

There are uncertainty relations between generalized position and momentum and also between time and energy. Since there is no operator for time in quantum mechanics, the foundation of the time and energy uncertainty principle is completely different from what we have in position and momentum. So, what exactly is meant by time reversal in quantum mechanics? The time evolution operator is given by

$$|\alpha, t_0 = 0; t = \delta t\rangle = \left[1 - i\frac{H}{\hbar}\delta t\right]|\alpha\rangle. \quad \textbf{(1.53)}$$

The time reversed state is $\Theta|\alpha\rangle$ and

$$\left[1 - i\frac{H}{\hbar}\delta t\right]\Theta|\alpha\rangle = \Theta\left[1 - i\frac{H}{\hbar}(-\delta t)\right]|\alpha\rangle\,. \quad \textbf{(1.54)}$$

Since

$$\left[1 - i\frac{H}{\hbar}\delta t\right]\Theta = \Theta\left[1 - i\frac{H}{\hbar}(-\delta t)\right], \quad \textbf{(1.55)}$$

$$\Theta - i\frac{H}{\hbar}\delta t = \Theta - \Theta i\frac{H}{\hbar}(-\delta t) \rightarrow iH\Theta = -\Theta iH\,. \quad \textbf{(1.56)}$$

The $i = \sqrt{-1}$ can be cancelled from both side, and if Θ is linear operator and

$$\Theta i = i\Theta \rightarrow H\Theta = -\Theta H. \quad \textbf{(1.57)}$$

Operating on both sides on an arbitrary eigenstate of the Hamiltonian,

$$H\Theta\,|\mathrm{E_n}\rangle = -\Theta H\,|\mathrm{E_n}\rangle = -\Theta \mathrm{E_n}|\mathrm{E_n}\rangle = -E_n\Theta|E_n\rangle, \quad \textbf{(1.58)}$$

$$H(\Theta\,|\mathrm{E_n}\rangle) = -E_n(\Theta\,|\mathrm{E_n}\rangle)\,. \quad \textbf{(1.59)}$$

Thus $\Theta\,|\mathrm{E_n}\rangle$ is also eigenstate of Hamiltonian but with the eigen value $-E_n$. Consider a free particle with eigenvalue E_n. If the time reversal operator operates on that, we have free particle with negative energy, and that is not correct. So the time reversal operator is not linear operator. If Θ is anti-linear operator,

$$\Theta i = -i\Theta \rightarrow H\Theta = \Theta H, \quad \textbf{(1.60)}$$

$$H\Theta\,|\mathrm{E_n}\rangle = \Theta H\,|\mathrm{E_n}\rangle = \Theta \mathrm{E_n}|\mathrm{E_n}\rangle = E_n\Theta|E_n\rangle\,, \quad \textbf{(1.61)}$$

$$H(\Theta\,|\mathrm{E_n}\rangle) = E_n(\Theta\,|\mathrm{E_n}\rangle)\,. \tag{1.62}$$

In other words, Θ is an *anti-linear operator*. So when time reversal operator in quantum mechanics operate in addition to $t \to -t$ we must have $i \to -i$ [20].

Consider collision and photoionization as one dimensional problem:

$$\psi_I(x) = Ae^{ikx} + Be^{-ikx} \qquad \psi_{III}(x) = Fe^{ikx} + Ge^{-ikx}$$

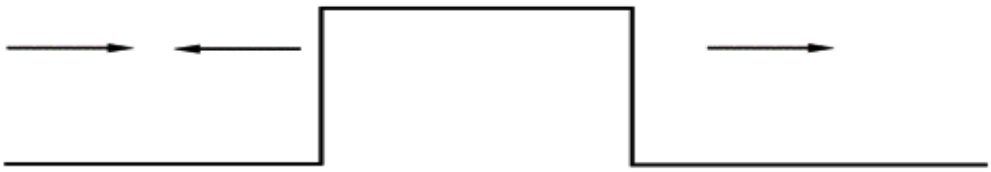

Figure1.3 Collision process in one dimension

In this case (collision), figure1.3, the electron comes from left ($A \neq 0$), i.e., the entrance channel is unique. The incident electron can be reflected ($B \neq 0$) or transmitted ($F \neq 0$), but in region *III* there is no wave coming from right to left ($G=0$). In other words $G=0$ is the boundary condition for this process where the electron is moving from left to right.

1.3 Photoionization

In photoionization, an atomic system absorbs electromagnetic radiation and by this absorption a continuum electron is created. In this case for this emitted electron there is a unique exit channel. Assuming the electron escapes to the left in figure1.4, since there is no free electron in the initial state it can be simulated by the dashed arrows so that there is no electron flux in initial state.

In this case, the unique exit channel leads to $A \neq 0$, and as a result of initial state simulation the *B* and *G* coefficients also are not zero, but since there is no wave coming from left to right in region *III* the coefficient *F* would be zero. So $F=0$ is the boundary condition for photoionization.

$$\psi_I(x) = Ae^{ikx} + Be^{-ikx} \qquad \psi_{III}(x) = Fe^{ikx} + Ge^{-ikx}$$

Figure1.4 photoionization in one dimension

So in a collision the outgoing wave is in the final state, and in photoionization the ingoing wave is in the initial state. Now we can say that these two states are connected to each other by the time reversal symmetry.

To calculate the total wave function for the photoionization process, we operate with the time reversal operator on the total scattering wave function which conforms to outgoing boundary conditions to obtain the solution with ingoing boundary conditions,

$$\psi_{total}(\vec{r}; r \to \infty) \to \frac{1}{2ikr}\sum_l c_l(2l+1)\left[P_l(cos\theta)e^{i(kr+\delta_l)} - P_l(-cos\theta)e^{-i(kr+\delta_l)}\right].$$

In this case we choose $c_l = e^{-i\delta_l}$ since the time reversal operator involves complex. This choice is called ingoing boundary condition,

$$\psi_{total}(\vec{r}; r \to \infty) \to \frac{1}{2ikr}\sum_l e^{-i\delta_l}(2l+1)\left[P_l(cos\theta)e^{i(kr+\delta_l)} - P_l(-cos\theta)e^{-i(kr+\delta_l)}\right]$$

$$= \frac{1}{2ikr}\sum_l (2l+1)\left[P_l(cos\theta)e^{i(kr)} - P_l(-cos\theta)e^{-i(kr+2\delta_l)}\right]. \qquad \textbf{(1.63)}$$

The incident plane wave in scattering, as $r \to \infty$ is

$$e^{ikz} \to \frac{1}{2ikr}\sum_l (2l+1)\left[P_l(cos\theta)e^{ikr} - P_l(-cos\theta)e^{-ikr}\right]. \qquad \textbf{(1.64)}$$

By subtracting the plane wave function from total wave function, the scattered wave function can be calculated (note that this scattered wave function is calculated with ingoing boundary condition).

$$\psi_{scattered} \to (\frac{e^{-ikr}}{r})\left[\frac{1}{2ik}\sum_{l=0}^{\infty}(2l+1)\left[e^{-2i\delta_l(k)}-1\right]P_l(-cos\theta)\right] \quad \textbf{(1.65)}$$

So the total wave function, with the ingoing wave boundary condition, is

$$\psi_{total}^{ingoing\ B.C.} \to$$

$$\frac{1}{2ikr}\sum_{l}(2l+1)\left[P_l(cos\theta)e^{ikr}-P_l(-cos\theta)e^{-ikr}\right] \quad \textbf{(1.66)}$$

$$-\frac{e^{-ikr}}{r}\left[\frac{1}{2ik}\sum_{l}(2l+1)\left\{e^{-2i\delta_l}-1\right\}P_l(-cos\theta)\right].$$

Now to get photoionization total wave function relevant to photoionization, we operate with the time reversal operator on (1.66), first ($i \to -i$),

$$\psi_{total}^{ingoing\ B.C.} \to e^{-ikz}+\frac{e^{ikr}}{r}\left[\frac{1}{2ik}\sum_{l}(2l+1)\left\{e^{2i\delta_l}-1\right\}P_l(-cos\theta)\right]. \quad \textbf{(1.67)}$$

We get the time dependent wave function by multiplying the total wave function with $e^{-i\omega t}$,

$$\psi_{total}^{ingoing\ B.C.}(r;r\to\infty,t) \to \left\{e^{-ikz}+\frac{e^{ikr}}{r}\left[\frac{1}{2ik}\sum_{l}(2l+1)\left\{e^{2i\delta_l}-1\right\}P_l(-cos\theta)\right]\right\}e^{-i\omega t}\ , \quad \textbf{(1.68)}$$

Then to complete operating time reversal operator we should change *t* to –*t* in (1.68),

$$\psi_{total}^{ingoing\ B.C.}(r;r\to\infty,t) \to \left\{e^{-i(kz-\omega t)}+\frac{e^{(ikr+\omega t)}}{r}\left[\frac{1}{2ik}\sum_{l}(2l+1)\left\{e^{2i\delta_l}-1\right\}P_l(-cos\theta)\right]\right\}. \quad \textbf{(1.69)}$$

The first term is the plane wave which is moving from left to right, representing the emitted photoelectron, and in the second term the numerator of the ratio is the ingoing wave and all the angles should be measured with respect to the unique exit channel, so by changing $z \to -z$ we have the correct picture of photoionization,

$$\psi_{total}^{photoionization}(r; r \to \infty, t) \to \left\{ e^{i(kz+\omega t)} + \frac{e^{(ikr+\omega t)}}{r} \left[\frac{1}{2ik} \sum_{l} (2l+1)\{e^{2i\delta_l} - 1\} P_l(cos\theta) \right] \right\}. \quad \textbf{(1.70)}$$

Thus the solution of photoionization comes from the solution of collision though the time reversal symmetry [21,22].

2.OSCILLATOR STRENGTH, PHOTOIONIZATION CROSS SECTION, AND ANGULAR DISTRIBUTION

2.1 Introduction

In the photoionization process the transition takes place from bound state to a continuum state, and this transition is effected due to the interaction between the electromagnetic field and quantum atomic system. The matrix element for photoionization is given generally as

$$\langle \psi_f | T | \psi_i \rangle \quad \textbf{(2.1)}$$

where $|\psi_i\rangle$is the initial state wave function, $|\psi_f\rangle$ is the final state wave function and T is the transition operator. This matrix element is the probability amplitude for the transition from an initial state to the final state, and

$$\left| \langle \psi_f | T | \psi_i \rangle \right|^2 \quad \textbf{(2.2)}$$

gives us transition probability, and this will be proportional to the intensity of absorption. To calculate the matrix element, we need to obtain the initial and final state wawe functions, and the transition operator. And by knowing matrix element, in addition to photoionization cross section, the angular distribution and spin-polarization parameters of the photoelectron emission can be calculated.

For initial state one can use the Independent Particle Approximation (IPA), Hartre- Fock (HF) for non-relativistic self-consistent calculation, Dirac-Fock (DF) for relativistic self consistent calculation, Multi Configuration Hartree-Fock (MCHF) or multi-configuration Dirac-Fock (MCDF) if electron correlation is taken into account for non-relativistic or relativistic calculation, or Local Density Approximation (LDA) that we will talk about it in the next chapter.

It has been discussed above that the asymptotic form of the final state wave function for a non-relativistic free photoelectron wave function according to ingoing wave boundary condition is

$$|\psi_f\rangle \rightarrow e^{ikz} - \frac{e^{-ikr}}{r}\sum_l (2l+1)P_l(-cos\theta)\left(\frac{e^{-2i\delta_l}-1}{2ik}\right). \quad \textbf{(2.3)}$$

If an electromagnetic wave is incident along the z-axis with polarization along the x-axis, the photoelectron direction, defined by $\vec{k}$, makes angle of θ with respect to polar axis (z axis) as shown in figure 2.1. The angular distribution of photoelectrons is determined, in the dipole approximation, by a single parameter known as the asymmetry parameter, β.

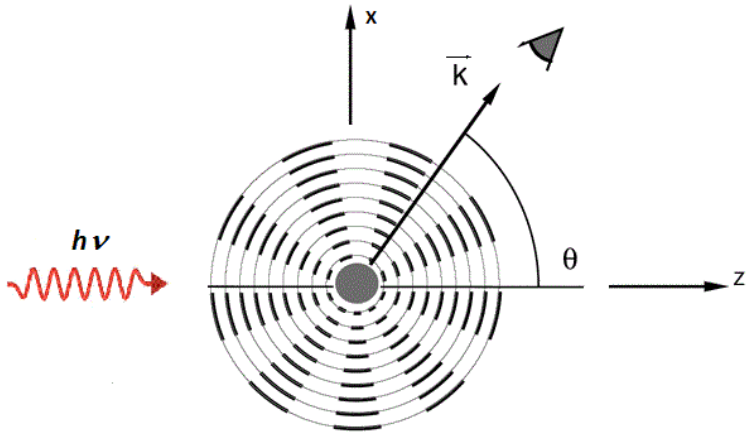

Figure2.1 Photoionization and angle of the ejected photoelectron

2.2 Photoionization cross section

In the photoabsoption process, an atomic system absorbs a photon which excites the system. For a single-electron system, the Hamiltonian including the interaction with the electromagnetic field is given by [23,24,25],

$$H = \left\{\frac{1}{2m}\left(\vec{p} - \frac{q}{c}\vec{A}(\vec{r},t)\right).\left(\vec{p} - \frac{q}{c}\vec{A}(\vec{r},t)\right) + q\phi(\vec{r},t) - \frac{Ze^2}{r}\right\}, \quad \textbf{(2.4)}$$

$$= \left\{\frac{1}{2m}\left(\vec{p}^2 - \frac{q^2}{c^2}\left[\vec{A}(\vec{r},t)\right]^2\right) - \frac{i\hbar q}{c}\left(\vec{\nabla}.\vec{A}(\vec{r},t) + \vec{A}(\vec{r},t).\vec{\nabla}\right) + q\phi(\vec{r},t) - \frac{Ze^2}{r}\right\}. \quad \textbf{(1.5)}$$

In a weak field, i.e. few photons, the quadratic term can be ignored compared to the linear term (see Appendix B). Then, using Coulomb gauge, $\vec{\nabla}.\vec{A} = 0$,

$$H = \left\{\frac{1}{2m}(\vec{p}^2) - \frac{Ze^2}{r} - \frac{iq\hbar}{mc}\vec{A}(\vec{r},t).\nabla\right\} = \left\{\frac{1}{2m}(\vec{p}^2) - \frac{Ze^2}{r} + \frac{q}{mc}\vec{A}(\vec{r},t).\vec{p}\right\} = H_0 + \lambda H', \quad \textbf{(1.6)}$$

where,

$$H' = -\frac{iq\hbar}{mc}\vec{A}(\vec{r},t).\nabla = \frac{q}{mc}\vec{A}(\vec{r},t).\vec{p}\,, \quad \textbf{(2.7)}$$

and λ is the perturbation order parameter, $q = -e$ is the electron charge, m is the mass of the electron, and c is the speed of light. By using first order perturbation and Fermi golden rule the expression for transition rate (transition probability per unit time) for photoabsorption resulting in a transition from initial state $|i\rangle$ to a final continuum state $|f\rangle$ effected by the transition perturbation operator is

$$\left[W_{fi}\right]_{\hat{k}_f}^{\hat{\varepsilon}} = \left(-\frac{qA_0(\omega)}{mc}\right)^2 \left|\left\langle f\left|e^{i\vec{k}.\vec{r}}\hat{\varepsilon}.\vec{\nabla}\right|i\right\rangle\right|^2 \times 2\pi\delta(\omega - \omega_{fi}), \quad \textbf{(2.8)}$$

to an excellent approximation. This transition rate is calculated for the particular case, the electromagnetic wave is polarized along vector $\hat{\varepsilon}$ and the electron is ejected along vector $\vec{k}$, we may have unpolarized wave or possibility for the electron to eject in different angle.

Differential cross section is defined as $\frac{Energy\ absorbed\ per\ unit\ time\ \ in\ i\to f}{Energy\ flux\ of\ the\ electromagnetic\ radiation}$.

$$\left[\frac{d\sigma}{d\Omega}\right]_{\hat{k}_f}^{\hat{\varepsilon}} = \frac{\hbar\omega \times \left[W_{fi}\right]_{\hat{k}_f}^{\hat{\varepsilon}}}{I(\omega)}\ . \quad \textbf{(2.9)}$$

By using the Maxwell equations and applying coulomb gage the intensity, $I(\omega)$, can be calculated.

$$\vec{A}(\vec{r},t) = A_0(\omega)\hat{\varepsilon}\cos\left(\vec{k}.\vec{r} - \omega t\right), \quad \textbf{(2.10)}$$

$$\vec{E}(\vec{r},t) = -\vec{\nabla}\phi - \frac{1}{c}\frac{\partial\vec{A}}{\partial t}\ , \quad \textbf{(2.11)}$$

$$\vec{H}(\vec{r},t) = \vec{\nabla}\times\vec{A}\ , \quad \textbf{(2.12)}$$

$$I(\omega) = \left\langle\left|\frac{c}{4\pi}\ \vec{E}\times\vec{H}\right|\right\rangle = \frac{\omega^2}{2\pi c}A_0^2(\omega)\,. \quad \textbf{(2.13)}$$

And by substituting (2.8) and (2.13) in (2.9), and also use the fine structure constant ($\alpha = \frac{e^2}{\hbar c}$), the differential cross section is

$$\left[\frac{d\sigma}{d\Omega}\right]_{\hat{k}_f}^{\hat{\varepsilon}} = \frac{4\pi^2\alpha\hbar^2}{m^2\omega}\left|\left\langle f\left|e^{i\vec{k}.\vec{r}}\hat{\varepsilon}.\vec{\nabla}\right|i\right\rangle\right|^2\delta(\omega-\omega_{fi})\,. \tag{2.14}$$

We can write the relation in terms of energy also,

$$\left[\frac{d\sigma}{d\Omega}\right]_{\hat{k}_f}^{\hat{\varepsilon}} = \frac{4\pi^2\alpha\hbar^3}{m^2\omega}\left|\left\langle f\left|e^{i\vec{k}.\vec{r}}\hat{\varepsilon}.\vec{\nabla}\right|i\right\rangle\right|^2\delta(E-E_{fi})\,. \tag{2.15}$$

Along the $\vec{k}$ vector there may be other degenerate states with the transition $i \to f$, so there is not a unique transition. Therefore the differential cross section should be multiplied by the number of states that have the transition with the same energy (See Appendix C), so,

$$\left[\frac{d\sigma}{d\Omega}\right]_{\hat{k}_f}^{\hat{\varepsilon}} = \frac{4\pi^2\alpha\hbar^3}{m^2\omega_{fi}}\left|\left\langle f\left|e^{i\vec{k}.\vec{r}}\hat{\varepsilon}.\vec{\nabla}\right|i\right\rangle\right|^2\left(\frac{L}{2\pi}\right)^3\left(\frac{mk}{\hbar^2}\right)\,. \tag{2.16}$$

Now, the matrix elements can be calculated and substituted in (2.15). In first Born approximation the final state can be approximated as a plane wave so that

$$M = \left\langle f\left|e^{i\vec{k}.\vec{r}}\hat{\varepsilon}.\vec{\nabla}\right|i\right\rangle = \int dV\left(\frac{1}{\sqrt{L^3}}e^{i\vec{k}_f.\vec{r}}\right)\left\{e^{i\vec{k}.\vec{r}}\hat{\varepsilon}.\vec{\nabla}\right\}\psi_i(\vec{r})\ . \tag{2.17a}$$

Since $\hat{\varepsilon}$ is orthogonal to $\hat{k}$

$$M = \frac{-i}{\sqrt{L^3}}\left[\hat{\varepsilon}.\vec{k}_f\right]\int\psi_i(\vec{r})e^{i(\vec{k}-\vec{k}_f).\vec{r}}dV\ . \tag{2.17b}$$

And if the angle between $\vec{k}_f$ and $\hat{\varepsilon}$ is γ, then $\hat{\varepsilon}.\vec{k}_f = k_f\cos\gamma$ so that

$$M = \left\langle f\left|e^{i\vec{k}.\vec{r}}\hat{\varepsilon}.\vec{\nabla}\right|i\right\rangle = \frac{-i\,k_f}{\sqrt{L^3}}\cos\gamma\int\psi_i(\vec{r})e^{i(\vec{k}-\vec{k}_f).\vec{r}}dV\ . \tag{2.17c}$$

If (2.17c) is substituted into (2.16) the size of the box will be cancelled, and the result is independent of L. The integral in (2.17c) is proportional to the Fourier Transform of the initial state wave function. If the initial state is describes by a hydrogenic 1s wave function, $\psi_{1s} = \frac{1}{\sqrt{\pi}}\left(\frac{Z}{a_0}\right)^{\frac{3}{2}}e^{-\frac{Zr}{a_0}}$, then the integral in (2.17c) is

$$Integral = \frac{1}{\sqrt{\pi}}\left(\frac{Z}{a_0}\right)^{\frac{3}{2}} \frac{8\pi\left(\frac{Z}{a_0}\right)}{\left\{\left[Z^2 + a_0^2\left|\vec{k} - \vec{k}_f\right|^2\right]\left[\frac{1}{a_0}\right]\right\}^2} \ . \tag{2.18}$$

and the differential cross section can be calculated by substituting (2.18) in (2.17c) and then in (2.16),

$$\left[\frac{d\sigma}{d\Omega}\right]_{\hat{k}_f}^{\hat{\varepsilon}} = \frac{32\alpha\hbar k_f^3}{m\omega_{fi}} \frac{Z^5 a_0^3 (cos^2\gamma)}{\left\{\left[Z^2 + a_0^2\left|\vec{k} - \vec{k}_f\right|^2\right]\left[\frac{1}{a_0}\right]\right\}^4} \ . \tag{2.19}$$

In the high energy Born approximation the kinetic energy of the photoelectron is much larger than its ionization energy [25],

$$\hbar\omega = \frac{\hbar^2 k_f^2}{2m} + \ I.E. \sim \frac{\hbar^2 k_f^2}{2m} \ \rightarrow kc \sim \frac{\hbar\, k_f^2}{2m} \ \rightarrow \frac{k}{k_f} \sim \frac{\hbar k_f}{2mc} = \frac{p_f}{2mc} = \frac{v_f}{2c} \ll 1 \ , \tag{2.20}$$

and if the polarization vector is along the x axis, then $\cos\gamma = \sin\theta\cos\phi$:

$$\left[\frac{d\sigma}{d\Omega}\right]_{\hat{k}_f}^{\hat{\varepsilon}} = \frac{32\alpha\hbar}{m\omega_{fi}}\left(\frac{Z}{a_0 k_f}\right)^5 \frac{sin^2\theta cos^2\phi}{\left(1 - \frac{v_f}{c}\, cos\theta\right)^4} \ . \tag{2.21}$$

For unpolarized light the average value of $cos^2\phi$ should be used,

$$\langle cos^2\phi\rangle = \frac{1}{2\pi}\int_0^{2\pi} cos^2\phi \ d\phi = \frac{1}{2} \ , \tag{2.22}$$

which gives

$$\left[\frac{d\sigma}{d\Omega}\right]_{\hat{k}_f}^{unpolarized} = \frac{16\alpha\hbar}{m\omega_{fi}}\left(\frac{Z}{a_0 k_f}\right)^5 (sin^2\theta)\left(1 + 4\frac{v_f}{c}\, cos\theta\right) \ , \tag{2.23}$$

and total cross section is

$$\sigma_{total}^{unpolarized} = \int \left[\frac{d\sigma}{d\Omega}\right]_{\hat{k}_f}^{unpolarized} d\Omega = \frac{128\pi}{3m}\frac{\alpha\hbar}{\omega}\left(\frac{Z}{a_0}\right)^5 \frac{1}{k_f^5} \ . \tag{2.24}$$

By knowing $kc \sim \frac{\hbar\, k_f^2}{2m}$ the total cross section for unpolarized light in first Born approximation is

$$\sigma_{total}^{unpolarized} = \frac{128\pi}{3m}\frac{\alpha\hbar}{\left(\frac{2m}{\hbar}\right)^{5/2}}\left(\frac{Z}{a_0}\right)^5 \frac{1}{\omega^{7/2}} \ . \tag{2.25}$$

As can be seen in (36), the cross section in this approximation goes as $\sigma \to E^{-7/2}, Z^5$. If a non-hydrogenic wave function is used in this calculation the cross section would be proportional to n^{-3}, n is the principle quantum number [26,27].

2.3 Oscillator Strength

2.3.1 Classical Oscillator Strength

Consider a classical interaction between electromagnetic wave and the electrons of an atomic system. The classical model assumes that the electrons oscillate about a certain mean position as they respond to the electromagnetic wave. As a result, there will be an induced dipole moment so the macroscopic terms like atomic polarizability, polarization, or susceptibility can also be defined for this system. An electromagnetic field and its electric intensity vector is described as

$$\vec{E} = \hat{\varepsilon} E_0 e^{-i(\omega t+\theta)} \ . \tag{2.26}$$

With this electric field (2.26), the force on each atomic electron is given by $-k\vec{r}(t)$ so that

$$m\frac{d^2\vec{r}}{dt^2} = -k\vec{r} \ . \tag{2.27}$$

Also a damping term, due to unspecified degrees of freedom, can be considered,

$$m\frac{d^2\vec{r}}{dt^2} = -k\vec{r} - (2\gamma)m\frac{d\vec{r}}{dt} \ , \tag{2.28}$$

and this damped oscillator is driven by the external field (2.26),

$$m\frac{d^2\vec{r}}{dt^2} = -k\vec{r} - (2\gamma)m\frac{d\vec{r}}{dt} + \hat{\varepsilon} E_0 e^{-i(\omega t+\theta)} \ . \tag{2.29}$$

The well-known solution for this damped-driven equation is

$$\vec{r}(t) = \hat{\varepsilon}\frac{e}{m}\frac{E_0}{\omega_{0,s}^2 - \omega^2 - i\Gamma_d\omega} e^{-i(\omega t+\theta)} \quad , \quad 2\gamma = \Gamma_d \ , \tag{2.30}$$

where ω is the frequency of the driving force, and $\omega_{0,s}$ is the natural frequency of the oscillator. Note that the displacement goes to zero as E_0 goes to zero; that means we have an induced dipole moment, or induced oscillating dipole moment.

Now we want to find the connection between oscillator strength, atomic polarizability, and the photoionization cross section. Atomic polarizability is defined as induced dipole moment per unit of electric field.

$$\vec{d} = \alpha \vec{E} \quad , \quad \alpha = \frac{|\vec{d}|}{|\vec{E}|} \, , \tag{2.31}$$

and also we know that dipole moment is proportional to displacement.

$$\vec{d} = e\vec{r}. \tag{2.32}$$

So, by using (2.26), (2.30), (2.31), and (2.32) the atomic polarizability is

$$\alpha = \frac{|e\vec{r}|}{|\vec{E}|} = \frac{e\left|\hat{\varepsilon}\frac{e}{m}\frac{E_0}{\omega_{0.s}^2 - \omega^2 - i\Gamma_d\omega}e^{-i(\omega t+\theta)}\right|}{\hat{\varepsilon}E_0 e^{-i(\omega t+\theta)}} = \frac{e^2}{m}\frac{1}{\omega_{0,s}^2 - \omega^2 - i\Gamma_d\omega} \, . \tag{2.33}$$

Since $\omega_{0,s} \sim \omega$, by factoring out $(\omega_{0,s} + \omega)$ in the denominator we have

$$\alpha = \frac{e^2}{m}\frac{1}{(\omega_{0,s}+\omega)\left((\omega_{0,s}-\omega) - \frac{i\Gamma_d\omega}{(\omega_{0,s}+\omega)}\right)} \sim \frac{e^2}{m}\frac{1}{2\omega_{0,s}\left((\omega_{0,s}-\omega) - \frac{i\Gamma_d\omega}{2\omega_{0,s}}\right)} \, . \tag{2.34}$$

If (2.33) is substituted in (2.30) we get displacement in terms of the polarizability,

$$\vec{r}(t) = \hat{\varepsilon}\frac{E_0\alpha(\omega)}{e}e^{-i(\omega t+\theta)} \, . \tag{2.35}$$

And by substituting (2.35) into (2.32), the dipole moment is

$$\vec{d}(t) = \hat{\varepsilon}E_0\alpha(\omega)e^{-i(\omega t+\theta)} \, . \tag{2.36}$$

To calculate cross section, at first the following question should be answered: What is the average power pumped to the atomic system by electromagnetic field? To answer this question we will start with classical definition of the average power,

$$\langle Q \rangle = \frac{1}{T}\int_0^T p(t)dt = \frac{1}{T}\int_0^T \frac{dW}{dt}dt = \frac{1}{T}\int_0^T \frac{\vec{F}.d\vec{r}}{dt}dt = \frac{1}{T}\int_0^T \left[\left(\frac{\vec{F}}{e}\right).(e\dot{r})\right]dt \, . \tag{2.37}$$

This is a real physical quantity so that

$$\langle Q\rangle_{Re} = \frac{1}{T}\int_0^T \left[\left(\frac{\vec{F}}{e}\right)_{Re} . (e\dot{r})_{Re}\right] dt \ . \quad \textbf{(2.38)}$$

By knowing the definition of electric field, $\vec{E} = \frac{\vec{F}}{e} = \hat{\varepsilon}E_0 e^{-i(\omega t+\theta)}$, the real part is

$$Re\left(\frac{\vec{F}}{e}\right) = \hat{\varepsilon}\frac{E_0}{2}\left(e^{-i(\omega t+\theta)} + e^{+i(\omega t+\theta)}\right) \ . \quad \textbf{(2.39)}$$

And also the real part of the other term is

$$e\dot{r}(t) = \ \hat{\varepsilon}(-i\omega)E_0\alpha(\omega)e^{-i(\omega t+\theta)} \ , \quad \textbf{(2.40)}$$

$$Re[e\dot{r}(t)] = \hat{\varepsilon}\frac{E_0\omega}{2}\left[(-i)\alpha(\omega)e^{-i(\omega t+\theta)} + (+i)\alpha^*(\omega)e^{+i(\omega t+\theta)}\right] \ . \quad \textbf{(2.41)}$$

By substituting (2.41) and (2.39) in (2.38) we get

$$\langle Q\rangle_{Re} = \frac{1}{T}\int_0^T \left[\frac{E_0^2\omega}{4}\begin{Bmatrix}(-i)\alpha(\omega)e^{-2i(\omega t+\theta)} + (+i)\alpha^*(\omega) + \\ (-i)\alpha(\omega) + (+i)\alpha^*(\omega)e^{+2i(\omega t+\theta)}\end{Bmatrix}\right] dt \ . \quad \textbf{(2.42)}$$

Only the first and the last term in curly bracket are time dependent and for calculating those terms for large interval of time $(T \to \infty)$, since before $t = 0$, E_0 was zero we can integrate them from $(-\infty \to +\infty)$, so that

$$\int_{t\to-\infty}^{t\to+\infty} e^{\pm 2i(\omega t+\theta)} dt = \pm\frac{\pi}{2}\delta(\omega) \, . \quad \textbf{(2.43)}$$

Since (2.43) will not zero at $\omega = 0$, and if the frequency is zero there will be no oscillation, these two terms do not contribute in the integral. So (2.42) can be written as,

$$\langle Q\rangle_{Re} = \frac{\omega E_0^2}{4}[(+i)\alpha^*(\omega) + (-i)\alpha(\omega)] = \left(\frac{\omega E_0^2}{2}\right) Im[\alpha(\omega)] \, . \quad \textbf{(2.44)}$$

Finally, the average power pumped into atomic system by electromagnetic field is given by

$$\langle Q\rangle_{Re} = \left(\frac{\omega E_0^2}{2}\right) Im[\alpha(\omega)] \ . \quad \textbf{(2.45)}$$

From equation (2.33), by multiplying both numerator and denominator by the complex conjugate of the denominator, the imaginary part of the polarizability can be calculated as

$$Im[\alpha(\omega)] = \frac{e^2}{m}\frac{\Gamma_d \omega}{\left|\omega_{0,s}^2 - \omega^2 + i\Gamma_d\omega\right|^2} \ . \quad \textbf{(2.46)}$$

Since $\omega_{0,s} \sim \omega$ we have

$$Im[\alpha(\omega)] \sim \frac{e^2}{2m\omega_{0,s}}\frac{\frac{\Gamma_d}{2}}{\left(\left(\omega_{0,s} - \omega\right)^2 - \left(\frac{\Gamma_d}{2}\right)^2\right)} \ . \quad \textbf{(2.47)}$$

If (2.47) is substitute in (2.45) we get

$$\langle Q\rangle_{Re} = \frac{e^2E_0^2}{4m}\frac{\frac{\Gamma_d}{2}}{\left((\omega_{0,s} - \omega)^2 - \left(\frac{\Gamma_d}{2}\right)^2\right)} \ . \quad \textbf{(2.48)}$$

Now, we define differential oscillator strength as

$$\frac{df}{d\omega} = \frac{1}{\pi}\frac{\frac{\Gamma_d}{2}}{\left((\omega_{0,s} - \omega)^2 - \left(\frac{\Gamma_d}{2}\right)^2\right)} \ . \quad \textbf{(2.49)}$$

This is so defined that if one integrates the oscillator strength over the range of frequency from $-\infty$ to $+\infty$ the result would be unity (Appendix D). Then the average power pumped to the atomic system by electromagnetic field in terms of differential oscillator strength is given by

$$\langle Q\rangle_{Re} = \frac{\pi}{4}\frac{e^2E_0^2}{m}\frac{df}{d\omega} \ . \quad \textbf{(2.50)}$$

2.3.2 Quantum Mechanical Oscillator Strength

In this part we will develop a quantum mechanical counterpart of the classical oscillator strength by using perturbation theory. Assuming the perturbed state of ψ_0 with energy E_0 is

$$\psi_0(t) = c_0(t)\psi_0 e^{-\frac{i\omega_0 t}{\hbar}} + \sum_s \psi_s c_s(t) e^{-\frac{i\omega_s t}{\hbar}} , \quad \textbf{(2.51)}$$

and the full Hamiltonian with the perturbation is

$$H = H_0 - er_k A\left(e^{+i\omega t} + e^{-i\omega t}\right) \ . \quad \textbf{(2.52)}$$

By using time dependent perturbation theory, we get

$$c_s(t) = \frac{e}{\hbar}\langle f|r_k|i\rangle A\left\{\frac{exp\ \left[i(\omega+\omega_s-\frac{1}{2}i\Gamma_d)\right]}{\omega+\omega_s-\frac{1}{2}i\Gamma_d}+\frac{exp\left[-i(\omega-\omega_s+\frac{1}{2}i\Gamma_d)\right]}{\omega-\omega_s+\frac{1}{2}i\Gamma_d}\right\}, \quad \textbf{(2.53)}$$

where $E_s - E_0 = \hbar\left(\omega_s - \frac{1}{2}i\Gamma_d\right)$.

The dipole moment due to the mixing ψ_0 and ψ_s is

$$e\langle x\rangle = e\sum_s \langle i|r_k|f\rangle\, c_s \exp\left[-i\left(\omega_s-\frac{1}{2}i\Gamma_d\right)t\right] + c_s^{\dagger}\exp\left[i\left(\omega_s+\frac{1}{2}i\Gamma_d\right)\right]\langle f|r_k|i\rangle, \quad \textbf{(2.54)}$$

and substituting (2.53) in (2.54) gives

$$e\langle x\rangle = \frac{e^2}{\hbar}\sum_s \langle i|r_k|f\rangle\left[\frac{Ae^{i\omega t}}{\omega_s^2-\omega^2+i\Gamma_d\omega}+\frac{Ae^{-i\omega t}}{\omega_s^2-\omega^2-i\Gamma_d\omega}\right]\langle f|r_k|i\rangle. \quad \textbf{(2.55)}$$

And a quantum mechanical definition of polarizability emerges by identifying the quantum dipole moment (66) as $A(\alpha(\omega)e^{-i\omega t}+\alpha^*(\omega)e^{i\omega t})$, and the quantum definition of the polarizability is then

$$\alpha(\omega) = \frac{e^2}{m}\sum_s \frac{f_s}{\omega_s^2-\omega^2-i\Gamma_d\omega}, \quad \textbf{(2.56)}$$

so the oscillator strength is

$$f_{fi} = \frac{2m\omega_{fi}}{\hbar}|\langle f|r_k|i\rangle|^2. \quad \textbf{(2.57)}$$

In the quantum mechanical definition the oscillator strength, for a given transition it can be either positive (in case of absorption $\omega_{fi} > 0$) or negative (in case of emission $\omega_{fi} < 0$), and, like the classical definition, the sum rule is valid here; it is known as the Thomas-Reiche-Kuhn sum rule (see Appendix E),

$$\sum_f f_{fi} = 1. \quad \textbf{(2.58)}$$

The equation (2.58) is the sum rule for a one-electron atom; if we have N-electron atom, the definition for oscillator strength is generalized to

$$f_{fi}^{(N)} = \frac{2m\omega_{fi}}{\hbar}\left|\sum_{j=1}^{N}\left\langle f\left|r_k^{(j)}\right|i\right\rangle\right|^2, \quad \textbf{(2.59)}$$

and the sum rule becomes

$$\sum_f f_{fi}^{(N)} = N. \quad \textbf{(2.60)}$$

By considering all final states in (2.51), we can write

$$\sigma_{total} \propto \int\left|\sum_{j=1}^{N}\left\langle f\left|r_k^{(j)}\right|i\right\rangle\right|^2 d\Omega, \quad \textbf{(2.61)}$$

so that the area under the total cross section is proportional to the sum of all oscillator strength which, owing to the sum rule, is equal to the number of initial state electrons in the target system.

2.4 The Angular Distribution of Photoelectrons:

The presence of angle dependent terms in the differential cross section means that the photoelectrons are not emitted isotropically but exhibit a characteristic angular distribution. To obtain angular distribution we start off with matrix element (2.17a) which can be written as

$$M = \left\langle f\left|e^{i\vec{k}.\vec{r}}\hat{\varepsilon}.\vec{\nabla}\right|i\right\rangle = \frac{1}{-i\hbar}\left\langle f\left|e^{i\vec{k}.\vec{r}}\hat{\varepsilon}.\vec{p}\right|i\right\rangle. \quad \textbf{(2.62)}$$

Also $e^{i\vec{k}.\vec{r}}$ can be expanded in terms of $\frac{r}{\lambda}$, and by taking the leading term

$$e^{i\vec{k}.\vec{r}} \sim 1, \quad \textbf{(2.63)}$$

giving an approximation known as the "Dipole Approximation". This approximation is good for large wavelengths or low energies. In this approximation, the matrix element,

$$M = \left\langle f\left|e^{i\vec{k}.\vec{r}}\hat{\varepsilon}.\vec{\nabla}\right|i\right\rangle \sim \frac{1}{-i\hbar}\langle f|\hat{\varepsilon}.\vec{p}|i\rangle. \quad \textbf{(2.64)}$$

This form of the matrix element is called the momentum or velocity form of the matrix element. Since we have the well-known commutation relation between momentum and position, the matrix element can also be written in position or length form

$$\left[r_k, p_k^2\right] = 2i\hbar p_k \;\rightarrow\; [r_k, H_0] = \frac{i\hbar}{m} p_k, \tag{2.65}$$

$$M = \left\langle f \middle| e^{i\vec{k}.\vec{r}}\, \hat{\varepsilon}.\vec{\nabla} \middle| i \right\rangle \sim \frac{i}{\hbar} \left\langle f \middle| \frac{m}{i\hbar} [r_k, H_0] \middle| i \right\rangle = \frac{m}{\hbar^2} (E_i - E_f) \langle f | r_k | i \rangle, \tag{2.66}$$

so it can be written

$$\langle f | \hat{\varepsilon}.\vec{p} | i \rangle = im\omega_{fi} \langle f | r_k | i \rangle. \tag{2.67}$$

This result is correct for exact wave functions. For approximate wave functions, the discrepancy between length and velocity forms gives some measure of the accuracy of the wave functions. Then, if (2.66) is substituted in (2.14), we have

$$\left[\frac{d\sigma}{d\Omega}\right]_{\hat{k}_f}^{\hat{\varepsilon}} = \frac{4\pi^2 \alpha \hbar^2}{m^2 \omega} \left| \frac{m}{\hbar^2} (E_i - E_f) \langle f | r_k | i \rangle \right|^2 \delta(\omega - \omega_{fi}). \tag{2.68}$$

Notice that the initial and final states are eigenfunctions of the unperturbed Hamiltonian, and from the previous chapter the final state of the photoelectron

$$\psi_{total}(\vec{r}) \xrightarrow[r\to\infty]{} \sum_l c_l i^l (2l+1) P_l(cos\theta) \frac{\sin\left(kr - \frac{l\pi}{4} + \delta_l\right)}{kr}. \tag{2.69}$$

And with the ingoing boundary condition, $c_l = e^{-i\delta_l}$, so

$$\psi_{total}(\vec{r}) \xrightarrow[r\to\infty]{} \sum_l e^{-i\delta_l} i^l (2l+1) \left\{ \frac{4\pi}{2l+1} \sum_{m=-l}^{l} Y_l^{m*}(\hat{k}_f) Y_l^m(\hat{r}) \right\} \frac{\sin\left(kr - \frac{l\pi}{4} + \delta_l\right)}{kr}\ , \tag{2.70}$$

then we can write

$$\psi_{total}(\vec{r}) = \sum_{l,m} a(l,m) Y_l^m(\hat{r}) R_{nl}(r)\ , \tag{2.71a}$$

where

$$a(l,m) = 4\pi\, e^{-i\delta_l} i^l Y_l^{m*}(\hat{k}_f), \tag{2.71b}$$

and the hydrogenic initial state is

$$\psi_{initial} = R_{n',l'}(r) Y_{l'}^{m'}(\hat{r}). \tag{2.72}$$

Considering the light polarization is along x axis, $\hat{\varepsilon} = \hat{e}_x$, and the angle between $\hat{k}_f$ and x axis is γ (figure 2.3). Therefore the transition matrix element is

$$\langle f|r_k|i\rangle = \langle f|\vec{r}.\hat{e}_x|i\rangle = \langle f|r\cos\gamma\,|i\rangle = \left\langle f\left|r\sqrt{\frac{4\pi}{3}}Y_1^{m=0}(\Theta,\Phi)\right|i\right\rangle . \quad \textbf{(2.73)}$$

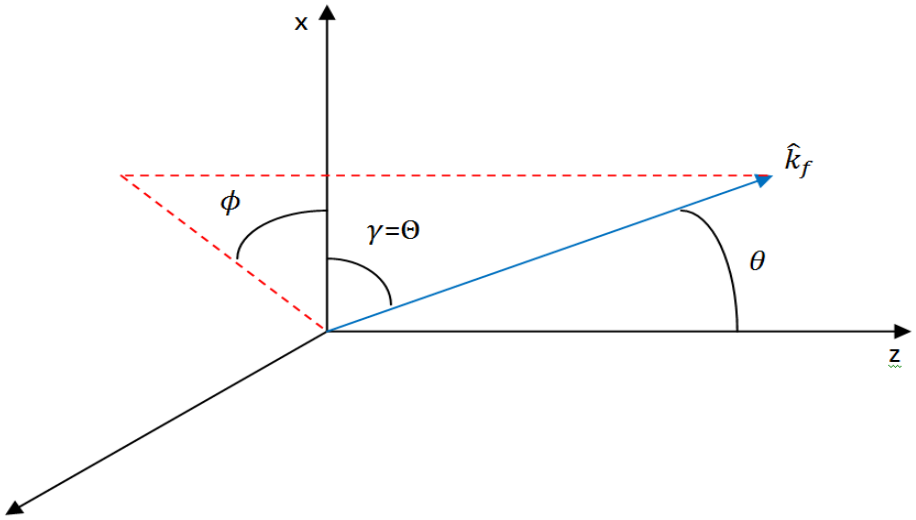

Figure2.2 Representation of the photoionization process with the photon incident along the z-axis. γ is the angle between the polarization axis, $\hat{\varepsilon} = \hat{e}_x$and the direction of the photoelectron $\hat{k}_f$, and ϕ is the angle between the projection of $\hat{k}_f$, in the xy--plane and the polarization.

It is useful to introduce a term that is called re-normalized spherical harmonics as follows

$$C_l^m(\Theta,\Phi) = \sqrt{\frac{4\pi}{2l+1}}Y_l^m(\Theta,\Phi), \quad \textbf{(2.74)}$$

so we can write the matrix element as

$$\langle f|r_k|i\rangle = \langle f|rC_1^{m=0}(\Theta,\Phi)|i\rangle. \quad \textbf{(2.75)}$$

Now, by having final state (2.71a) and initial state (2.72) the matrix element can be calculated,

$$\langle f|r_k|i\rangle = \langle f|rC_1^{m=0}(\Theta,\Phi)|i\rangle = \left\langle \sum_{l,m} a(l,m)Y_l^m(\hat{r})R_{nl}(r)\left|rC_1^{m=0}(\Theta,\Phi)\right|R_{n'l'}(r)Y_{l'}^{m'}(\hat{r})\right\rangle. \quad \textbf{(2.76)}$$

Then,

$$\langle f|r_k|i\rangle = \sum_{l,m} a(l,m)\left[\int_0^\infty r^2 dr\, R_{nl}(r)rR_{n',l'}(r)\right]\langle Y_l^m(\hat{r})|C_1^{m=0}(\Theta,\Phi)|Y_{l'}^{m'}(\hat{r})\rangle, \quad \textbf{(2.77a)}$$

$$\langle f|r_k|i\rangle = \sum_{l,m} a(l,m)[d_{ll'}]\,\langle lm|C_1^{m=0}(\Theta,\Phi)|l'm'\rangle. \quad \textbf{(2.77b)}$$

To get the matrix element of re-normalized spherical harmonics, we use the Wigner-Eckart theorem,

$$\langle lm|C_1^{m=0}(\Theta,\Phi)|l'm'\rangle = (-1)^{l-m}\langle l|C_1|l'\rangle \begin{pmatrix} l & 1 & l' \\ -m & 0 & m' \end{pmatrix}, \quad \textbf{(2.78)}$$

and,

$$\langle l|C_1|l'\rangle = (-1)^{\frac{l'-l+1}{2}}\sqrt{l_>} = (-1)^g\sqrt{l_>} \quad \textbf{(2.79)}$$

where $l_>$ is the greater of the l and l', and $g = \frac{l'-l+1}{2}$.

Then, if (2.78) and (2.79) are substituted in (2.77b) we have

$$\langle f|r_k|i\rangle = \sum_{l,m} a(l,m)[d_{ll'}]\left\{(-1)^g\sqrt{l_>}\,(-1)^{l-m}\begin{pmatrix} l & 1 & l' \\ -m & 0 & m' \end{pmatrix}\right\}. \quad \textbf{(2.80)}$$

Now we can substitute (2.80) in (2.68),

$$\left[\frac{d\sigma}{d\Omega}\right]_{\hat{k}_f}^{\hat{\varepsilon}} \propto \frac{1}{2l+1}\sum_m \left\{\left\{\sum_{l_1} a(l_1,m)\left[d_{l_1 l}\right]\left\{(-1)^g\sqrt{l_>}\,(-1)^{l_1-m}\begin{pmatrix} l_1 & 1 & l \\ -m & 0 & m \end{pmatrix}\right\}\right\}\right.$$
$$\left.\left\{\sum_{l_2} a^*(l_2,m)\left[d_{l_2 l}\right]\left\{(-1)^g\sqrt{l_>}\,(-1)^{l_2-m}\begin{pmatrix} l_2 & 1 & l \\ -m & 0 & m \end{pmatrix}\right\}\right\}\right\}. \quad \textbf{(2.81)}$$

Note that in dipole approximation $\Delta l = \pm 1$, so we do not need to sum l from zero to infinity. Therefore we have only four terms. And by introducing energy dependent angular distribution asymmetry parameter, β, the relation (2.81) simplifies to

$$\left[\frac{d\sigma}{d\Omega}\right]_{\hat{k}_f}^{\hat{\varepsilon}} = \frac{\sigma_{total}}{4\pi}(1+\beta P_2(cos\Theta)), \quad \textbf{(2.82)}$$

called the Cooper-Zare formula [28], where the angular distribution asymmetry parameter is given by

$$\beta = \frac{l(l-1)d_{l-1,l}^2 + (l+1)(l+2)d_{l+1,l}^2 - 6l(l+1)d_{l+,l}d_{l-1,l}\cos(\delta_{l+1}-\delta_{l-1})}{(2l+1)\left[ld_{l-1,l}^2 + (l+1)d_{l+1,l}^2\right]}. \quad \textbf{(2.83)}$$

Because the total cross section and differential cross section are positive quantities, and by knowing that $P_2(cos\Theta) = \frac{1}{2}(3cos^2\Theta - 1)$ and the limits for Θ, the limits for β are

$$\left.\begin{array}{l} \frac{\beta}{2}(3cos^2\Theta - 1) \geq -1 \\ 0 \leq \Theta \leq \pi \ \rightarrow 0 \leq cos^2\Theta \leq 1 \end{array}\right\} \rightarrow \ -1 \leq \beta \leq 2 \ . \qquad \textbf{(2.84)}$$

3.DENSITY FUNCTIONAL THEORY (DFT), LOCAL DENSITY APPROXIMATION (LDA), AND TIME DEPENDENT LDA (TDLDA)

3.1 Introduction

Density functional theory is a very powerful tool used in many-body quantum computational physics. Unlike the other methods, instead of solving Schrödinger equation with many variables (position of the nucleus and each of the electrons), in this method we try to solve a differential equation for electron density, that has only three variables for each point in space, and we use that to calculate wave functions and their energies. For this method some approximations must be used. In this work, the Local Density Approximation (LDA), and Time-Dependent LDA (TDLDA) are used these methods are discussed in detail in this chapter.

3.2 Density Functional Theory (DFT)

Density functional theory is based upon two mathematical theorems that were proposed and proved in 1964 by Hohenberge and Kohn [29] .These two theorems are:

1. The electron density $n(\vec{r})$ in the ground state is a functional of the potential $U(\vec{r})$.
2. The potential $U(\vec{r})$ is unique functional of the density $n(\vec{r})$.

In other words, together, these theorems are equivalent to the assertion that the ground state energy E_G is minimum with respect to variations in the electron density $n(\vec{r})$.

By introducing the concept of functional variation, these two theorems can be stated more precisely. The energy of the ground state, E_G, characterizes the entire system. The electron density, $n(\vec{r})$, depends upon the position, $\vec{r}$. The functional derivative of the ground state energy with respect to the electron density, $\frac{\delta E_G}{\delta\, n(\vec{r})}$, is a function of $\vec{r}$; this gives the change in the ground state energy at each

point as a function of the variation in density at that point. So, if F is a functional with linear and quadratic dependences on the electron density, the functional derivative is

$$F = \int d^3r\, n(\vec{r})\, u(\vec{r}) + \int d^3r_1 d^3r_2\ \ n(\vec{r}_1)\, V(\vec{r}_1 - \vec{r}_2)\, n(\vec{r}_2), \tag{3.1}$$

$$\frac{\delta E_G}{\delta\, n(\vec{r})} = \ u(\vec{r}) + \ 2\int d^3r' V(\vec{r} - \vec{r}')n(\vec{r}'). \tag{3.2}$$

The total number of electrons in a system is usually fixed, N, and that is a constraint on the variation with respect to the density. The variation with constraints is handled by introducing Lagrange multipliers. So, the functional derivative of the ground state with respect to the electron density is equal to a Lagrange multiplier, which is constant,

$$\frac{\delta E_G}{\delta\, n(\vec{r})} = \ \mu, \tag{3.3}$$

$$\int d^3r\ \delta n(\vec{r}) = 0. \tag{3.4}$$

The single particle Hamiltonian for a single electron includes the kinetic energy, T, the nuclear potential energy, $U(\vec{r})$, the self-consistent potential owing to the electrostatic fields of the other electrons (the Hartree potential), $V_H(\vec{r})$, and $V_{xc}(\vec{r})$ which is a central-field approximation to the effects of exchange and correlation. The sum of $V_H(\vec{r})$, and $V_{xc}(\vec{r})$ are an approximation to the excat potemtila in (3.1). Furthermore, the kinetic energy term can be similarly constructed; for non-interacting particles we have

$$T = \frac{\hbar^2}{2m}\int d^3r \sum_j \vec{\nabla}\psi_j^{\dagger}\ .\vec{\nabla}\psi_j. \tag{3.5}$$

According to the Hohenberg and Kohn theorem, the ground state energy including kinetic energy can be represented in terms of density. But how is (3.5) represented by the density? The simplest way is using Thomas-Fermi approximation. Thomas and Fermi (TF) in the 1920s [30,31] suggested looking at atoms as uniformly distributed electrons (negative charged cloud) around nuclei in six dimensional spaces

(momentum and coordinate). Using the Thomas-Fermi approach, the kinetic energy of the system can be written as a functional of the local electron density (see Appendix F) as

$$T_{TF}[\rho] = C_F \int n^{5/3}(\vec{r})\, d^3r \quad , \quad C_F = \frac{3}{10}(3\pi^2)^{2/3}. \tag{3.6}$$

So, the first step for constructing a functional for the ground state energy is to add the TF kinetic energy to potential, (3.1)

$$E_{TF} = \frac{3}{10}(3\pi^2)^{2/3} \int n^{5/3}(\vec{r})\, d^3r + \int d^3r\, n(\vec{r})\, u(\vec{r}) + \int d^3r_1 d^3r_2 \ \frac{n(\vec{r}_1)\, n(\vec{r}_2)}{|\vec{r}_1 - \vec{r}_2|} \ . \tag{3.7}$$

Then by using (3.3) the chemical potential is

$$\mu = \frac{1}{2}\left(3\pi^2\, n(\vec{r})\right)^{2/3} + u(\vec{r}) + 2\int d^3r' \frac{n(\vec{r'})}{|\vec{r} - \vec{r}'|} \ . \tag{3.8}$$

The, (3.8) can be solved to give the density as a functional of the screened potential

$$n(\vec{r}) = \frac{1}{3\pi^2}(2)^{3/2}\left(\mu - \ u(\vec{r}) - V_H(\vec{r})\right)^{3/2} \quad , \ V_H(\vec{r}) = 2\int d^3r' \frac{n(\vec{r'})}{|\vec{r} - \vec{r}'|} \ . \tag{3.9}$$

This result is not numerically very accurate. In order to increase the accuracy, the kinetic energy term must be changed to a better form. This can be done by introducing terms which involve the gradient of the density. This has been investigated extensively by Von Weizsacker in 1935 [32,33],

$$T[n] = \int t[n(\vec{r})] d^3r, \tag{3.10}$$

$$t[n(\vec{r})] = t_0[n(\vec{r})] + t_2[n(\vec{r})] + t_4[n(\vec{r})] + \cdots, \tag{3.11}$$

$$t_2[n(\vec{r})] = \frac{1}{72}\frac{(\nabla n)^2}{n}, \tag{3.12}$$

$$t_4[n(\vec{r})] = \frac{(3\pi^2)^{-2/3}}{540} n^{1/3}\left[\left[\frac{\nabla^2 n}{n}\right]^2 - \frac{9}{8}\left[\frac{\nabla^2 n}{n}\right]\left[\frac{\nabla n}{n}\right]^2 + \frac{1}{3}\left[\frac{\nabla n}{n}\right]^4\right]. \tag{3.13}$$

The modern theory uses the wave function form of kinetic energy as given (3.5). Additional improvements in the ground state energy are achieved by adding terms which include the effect of exchange and correlation.

3.3 Local Density Approximation (LDA)

In this section we discuss the second remarkable paper on the Density Functional Theory by Kohn and Sham in 1965 [34]. They added some features to the theory which brought it to the form which is used today. Their theory is called *Local Density Approximation* (LDA). Their paper made a big contributions to the kinetic energy,$T[n(\vec{r})]$, and exchange-correlation,$E_{xc}[n(\vec{r})]$, terms, that would be added to electron nucleus potential and self consistent terms

$$E_G = T + E_{xc} + \int d^3r\, n(\vec{r})\, u(\vec{r}) + \int d^3r_1 d^3r_2 \;\frac{n(\vec{r}_1)\, n(\vec{r}_2)}{|\vec{r}_1 - \vec{r}_2|}\,. \tag{3.14}$$

Kohn and Sham suggested a way to calculate kinetic and exchange-correlation terms that is the basis for LDA.

3.3.1. Exchange-Correlation term

Suppose $\varepsilon_{xc}(n_0)$ is the ground state energy per electron from the exchange and correlation in electron gas of uniform density n_0. The total ground state energy from exchange-correlation is then

$$E_{ex} = N\varepsilon_{xc}(n_0)\,, \tag{3.15}$$

where N is the number of electrons. If we express the number N as an integral over all space of the density, the exchange-correlation energy of the ground state is

$$E_{ex} = \int d^3r\, n_0 \varepsilon_{xc}(n_0)\,. \tag{3.16}$$

Kohn and Sham suggested that the inhomogeneous electron gas can be treated by replacing the constant density, n_0, by the actual electron density, $n(\vec{r})$

$$E_{ex} = \int d^3r n(\vec{r}) \varepsilon_{xc}(n(\vec{r}))\,. \tag{3.17}$$

This assumption is the basis of the Local Density Approximation, LDA, version of Density Functional, DFT. This is a very good approximation when the density is slowly varying with the position, $\vec{r}$. The Kohn-

Sham method was a great improvement, since it cast the potentials as due to functional derivatives of the ground state energy terms,

$$V_{xc} = \frac{\delta E_{ex}}{\delta n(\vec{r})} \,. \tag{3.18}$$

The total LDA potential is given by

$$V(\vec{r}) = V_{xc}(\vec{r}) + V_H(\vec{r}) + u(\vec{r}) \,, \tag{3.19}$$

where $V_{xc}(\vec{r})$, $V_H(\vec{r})$, and $u(\vec{r})$ are respectively the exchange-correlation, self consistent, and the electron nucleus potentials.

3.3.2. Kinetic energy term

To calculate the kinetic energy the Kohn-Sham treatment, one simply uses the eigenfunction description of (3.5), so that in atomic units,

$$T = \int d^3r \sum_j \vec{\nabla}\psi_j^\dagger \cdot \vec{\nabla}\psi_j \,. \tag{3.20}$$

3.3.3. Ground state energy and electron density

The ground state energy is the sum of the kinetic energy, (3.20), and potential energy, (3.19). By taking the functional derivative of each of the terms of the ground state energy with respect to the Hermitian conjugate of the eigenfunction $\psi_j^\dagger$, we have

$$\frac{\delta E_G}{\delta \psi_j^\dagger} = \frac{\delta T}{\delta \psi_j^\dagger} + \frac{\delta V}{\delta \psi_j^\dagger} \,. \tag{3.21}$$

Since the potential energy is a functional of density and the wave function $\psi_j^\dagger$ enters only though the electron density, the second term of the (3.21) can be written

$$\frac{\delta V}{\delta \psi_j^\dagger} = \frac{\delta V}{\delta n(\vec{r})} \frac{\delta n(\vec{r})}{\delta \psi_j^\dagger} = \frac{\delta V}{\delta n(\vec{r})} \psi_j \,, \tag{3.22}$$

And, for the kinetic term, it is

$$\frac{\delta T}{\delta \psi_j^\dagger} = -\nabla^2 \psi_j \,. \tag{3.23}$$

Now, the variation of the eigenfunctions must be done with constraint of conserving the number of electrons, which introduces the Lagrange multiplier λ,

$$\frac{\delta}{\delta \psi_j^\dagger}\left[E_G - \lambda \int d^3r\, n(\vec{r})\right] = 0 \,, \tag{3.24}$$

$$\{-\nabla^2 + V_{xc}(\vec{r}) + V_H(\vec{r}) + u(\vec{r})\}\psi_j = \lambda_j \psi_j \,, \tag{3.25}$$

$$n(\vec{r}) = \sum_j \left|\psi_j\right|^2 . \tag{3.26}$$

The density is determined by summing over all the densities of the N electrons. Then (3.25) and (3.26) are used to calculate the ground state energy self-consistently. The Schrödinger-like equation (3.25) is solved for the eigenfunction ψ_j for each occupied state j. These eigenfunctions are used to calculate the electron density, and the electron density is used to calculate the potential terms. This process is iterated until self-consistency is achieved.

The final results of this calculation are two important quantities: (i) The electron density $n(\vec{r})$, and (ii) The ground state energy E_G. The ground state energy is determined self-consistently in the eigenfunctions, and since we have the eigenfunctions, the density is the sum of the squares of the absolute eigenfunctions. Thus, the ground state energy can be written

$$E_G = \sum_j \int d^3r\, \psi_j^\dagger \left\{-\nabla^2 + V_{xc}(\vec{r}) + \frac{1}{2}V_H(\vec{r}) + u(\vec{r})\right\}\psi_j \,, \tag{3.27}$$

and the kinetic energy term can be evaluated using Kohn-Sham equation (3.25),

$$E_G = \sum_j \lambda_j - \int d^3r_1 d^3r_2 \;\frac{n(\vec{r}_1)\, n(\vec{r}_2)}{|\vec{r}_1 - \vec{r}_2|} \;+ \int d^3r\, n(\vec{r}) \left(\varepsilon_{xc}\big(n(\vec{r})\big) - V_{xc}\big(n(\vec{r})\big)\right). \tag{3.28}$$

By using the definition of the exchange-correlation potential V_{xc} as a functional derivative of the terms in the ground state energy the last term in (3.28) can be simplified to

$$V_{xc} = \frac{\delta}{\delta n}\int d^3 r n(\vec{r})\varepsilon_{xc}\big(n(\vec{r})\big) = \varepsilon_{xc} + n(\vec{r})\left(\frac{\partial \varepsilon_{xc}}{\partial n}\right)_{n=n(\vec{r})}, \quad \textbf{(3.29)}$$

$$\int d^3 r\, n(\vec{r})\, \Big(\varepsilon_{xc}\big(n(\vec{r})\big) - V_{xc}\big(n(\vec{r})\big)\Big) = -\int d^3 r\big(n(\vec{r})\big)^2 \left(\frac{\partial \varepsilon_{xc}}{\partial n}\right)_{n=n(\vec{r})}. \quad \textbf{(3.30)}$$

This term is positive since the exchange-correlation energy is decreasing with increasing density.

We used the eigenfunctions for the ψ_j and the eigenvalues for the λ_j, but it is a mistake to think of these functions as representing wave function and energy of the one-electron state. There is no Hamiltonian defined for single electron. Therefore, there would be no wavefunction and energy eigenvalue for single electron. The way to think about these quantities is that ψ_j and λ_j are just quantities which are computed while solving the LDA equations. So, the terms "Kohn-Sham eigenfunctions" and "Kohn-Sham eigenvalues" are used for them. The only quantities that have physical interpretations are the ground state energy and electron density, which, at least in principle, can be measured experimentally.

So far, since for filled shell atoms the spin plays a minor role in the theory, as it can be seen in the LDA equations (3.25), we haven't considered spin of electrons in our calculation. For atoms that the shells are partially filled with electrons, the number of up spin-electrons may be different than the down-spin ones; in this case the exchange-correlation potential depends upon the spin of the electrons. In order to calculate partially filled shell atoms, the separate equations for each spin component plus the spin dependent exchange-correlation potential must be considered. These coupled equations make calculation for unfilled shells much more complicated. These equations are discussed in Lundqvist and March [35]. All of our calculations will be for filled shell atoms, where the spin component, except for rules about the number of electrons in an orbital, is unimportant.

By using LDA we have simple calculations and accurate results, but one should not forget that LDA is only an approximation for solving complicated DFT equations. The first approximation is used in the kinetic energy term. The kinetic energy is not a functional of density and is derived from independent particle states. The theorem of Hohenberg and Kohn says that the entire ground state energy is a func-

tional of the electron density, and since the kinetic energy term is treated differently we make an approximation. The second approximation is using a local spherically-symmetric function for exchange-correlation potential. The theorem is that the exchange-correlation potential is a function of the electron density, so making it a local function of electron density is an approximation.

3.4. Linear and Non-linear Response

Most experiments in atomic and condensed matter physics measure the response of a system to a relatively weak perturbation. For instance, measurement of the absorption and photoionization of incident electromagnetic waves, electrical current in response to an applied electric field, magnetization induced by applied magnetic field, etc. Linear response means that the measured signal is directly proportional to the intensity of the perturbation, and the higher order response functions are proportional to higher powers of the strength of the perturbation. It is obvious that if the external incident or induced field is strong the concept of perturbation is not valid, and the power series description breaks down.

3.4.1. Response Function

The propagation of the electromagnetic waves in a medium is governed by Maxwell's equations in the semiclassical theory of radiation. In particular, the displacement $\vec{D}$ and the electric field $\vec{E}$ are related by

$$\vec{D} = \vec{E} + 4\pi\vec{P} \tag{3.31}$$

where $\vec{P}$ is the polarization or the induced dipole moment density of the medium. In linear response theory, the induced polarization is proportional to the electric field, so

$$\vec{D} = \epsilon\,\vec{E}\ , \tag{3.32}$$

where ϵ is the dielectric tensor. The polarization may contain non-linear terms as well,

$$\vec{P}(\vec{r},t) = \vec{P}^{(1)}(\vec{r},t) + \vec{P}^{(2)}(\vec{r},t) + \vec{P}^{(3)}(\vec{r},t) + \cdots, \tag{3.33}$$

where the superscript denotes the power of the electric field in each term [36]. The response functions can be shown as follow [37]

$$\vec{P}^{(n)}(\vec{r},t) = \int_{-\infty}^{t} dt_1 \dots \int_{-\infty}^{t} dt_n$$

$$\int d^3r_1 \dots \int d^3r_n \;\; \Phi^{(n)}_{ijl\dots\alpha}(\vec{r},t;\, \vec{r}_1,t_1;\dots;\vec{r}_n,t_n)\;\, \varepsilon_j(\vec{r}_1,t_1)\dots\varepsilon_\alpha(\vec{r}_n,t_n)\,, \tag{3.34}$$

where the summation convention on repeated subscripts is implied and the $\Phi^{(n)}_{ijl\dots\alpha}$ are the response functions that are the subject to conditions which result from causality, and from the fact that the polarization must be real if the electric field is real. The susceptibilities are appropriately summed Fourier transforms of the response functions,

$$\chi^{(n)}_{ijk\dots}(\vec{k}\omega;\vec{k}_1\omega_1,\dots,\vec{k}_n\omega_n) = \frac{1}{n!}\sum_{\wp}\kappa^{(n)}_{ijk\dots}(\vec{k}\omega;\vec{k}_1\omega_1,\dots,\vec{k}_n\omega_n)\,, \tag{3.35}$$

where $\wp$ refers to the sum over all terms obtained by permutation of $j\vec{k}_1\omega_1, l\vec{k}_2\omega_2, \dots$, and

$$\kappa^{(n)}_{ijk\dots}(\vec{k}\omega;\vec{k}_1\omega_1,\dots,\vec{k}_n\omega_n)$$

$$= \int d\tau \int d^3r \int d\tau_1 d^3r_1 \dots \int d\tau_n d^3r_n\, \Phi^{(n)}_{ijl\dots\alpha}(\vec{r},\tau;\, \vec{r}_1,\tau_1;\dots;\vec{r}_n,\tau_n) ex\,p\big(i\vec{k}.\vec{r}\big)\, ex\,p\big[i\big(\vec{k}.\vec{r} \tag{3.36}$$

$$+ \vec{k}_1.\vec{r}_1 + \cdots\big) - i(\omega\tau + \omega_1\tau_1 + \cdots)\big].$$

As an example, the induced polarization for a monochromic, long wavelength field up to third order in electric field can be written as

$$\vec{P}(t) = P^{(0)} + \chi^{(1)}(\omega).\varepsilon\cos(\omega t) + \chi^{(2)}(0){:}\,\varepsilon\varepsilon + \chi^{(2)}(2\omega){:}\,\varepsilon\varepsilon\cos(2\omega t) + \chi^{(3)}(\omega)$$

$$\vdots\, \varepsilon\varepsilon\varepsilon\cos(\omega t) + \chi^{(3)}(3\omega)\,\vdots\,\varepsilon\varepsilon\varepsilon\cos(3\omega t) + \cdots. \tag{3.37}$$

The first term is due to the permanent dipole moment, the second term is the linear response, and leads to the standard linear dielectric function. The third term represents a static moment proportional to the square of the electric field and describes optical rectification [38], the forth term describes second harmonic generation, and the fifth term leads to the nonlinearly of the refractive index, while it is responsible for the third harmonic generation.

3.4.2. Perturbation Theory

Usually, time dependent perturbation theory is starting point for the description of the response of the system (e.g. atom or molecule) to an external field. So, in this section the derivation of the linear and non-linear susceptibilities using standard perturbation theory is presented.

Consider for a system, that governed by an unperturbed time-independent Hamiltonian $H^{(0)}(\vec{r})$, a time-dependent perturbation,

$$H^{(1)}(r,t) = f(t)V^{(1)}(r,t), \tag{3.38}$$

where $f(t)$ is such that

$$H^{(1)}(\vec{r}, t \to -\infty) \to 0. \tag{3.39}$$

Assume that at $t = -\infty$ the system is in a particular, normalized, non-degenerate state with the eigenstate $\phi_j^{(0)}(\vec{r})$ of the unperturbed Hamiltonian $H^{(0)}(\vec{r})$, with energy $E_j^{(0)}$,

$$\Psi(\vec{r}, t \to -\infty) = \phi_j^{(0)}(\vec{r}) exp\left[-\frac{iE_j^{(0)}t}{\hbar}\right] \equiv \Psi^{(0)}(\vec{r}, t). \tag{3.40}$$

Also, it is assumed that the total Hamiltonian is Hermitian, the perturbation is significantly smooth and continuous in all time such that the normalization of $\Psi^{(0)}$ implies that the wave function is normalized for all the times. So, the system is governed by time-dependent Schrödinger equation,

$$\left[H^{(0)}(\vec{r}) + H^{(1)}(\vec{r}, t) - i\hbar\left(\frac{\partial}{\partial t}\right)\right]\Psi(\vec{r}, t) = 0\,. \tag{3.41}$$

Consider a case that static perturbation turned on adiabatically. One could introduce the ansatz,

$$\Psi(\vec{r}, t) = \xi_s(\vec{r}) exp\,(-iE_s t/\hbar) \tag{3.42}$$

where $\xi_s(\vec{r})$ is the normalized eigenfunction of the total Hamiltonian, and E_s is the corresponding perturbed eigenvalue, that can be expanded in perturbation series,

$$\xi_s(\vec{r}) = \sum_{n=0}^{\infty} \xi^{(n)}(\vec{r}), \tag{3.43}$$

$$E_s = \sum_{n=0}^{\infty} E^{(n)}. \tag{3.44}$$

By substituting these two expansions in (3.41) we have:

$$\left[H^{(0)}(\vec{r}) - E^{(0)}\right]\xi^{(0)}(\vec{r}) = 0, \tag{3.45}$$

$$\left[H^{(0)}(\vec{r}) - E^{(0)}\right]\xi^{(1)}(\vec{r}) = \left[H^{(1)}(\vec{r}) - E^{(1)}\right]\xi^{(0)}(\vec{r}), \tag{3.46}$$

$$\left[H^{(0)}(\vec{r}) - E^{(0)}\right]\xi^{(n)}(\vec{r}) = \left[H^{(1)}(\vec{r}) - E^{(1)}\right]\xi^{(n-1)}(\vec{r}) + \sum_{k=1}^{n} E^{(k)}\xi^{(n-k)}(r), \qquad n > 1 \tag{3.47}$$

with

$$E^{(1)} = \left\langle \xi^{(0)} \middle| H^{(1)} \middle| \xi^{(0)} \right\rangle, \tag{3.48}$$

$$E^{(n)} = \left\langle \xi^{(0)} \middle| H^{(1)} \middle| \xi^{(n-1)} \right\rangle - \sum_{k=1}^{n-1} \left\langle \xi^{(0)} \middle| \xi^{(n-1)} \right\rangle, \qquad n > 1 \tag{3.49}$$

and

$$\sum_{k=0}^{n} \left\langle \xi^{(k)} \middle| \xi^{(n-k)} \right\rangle = 0, \quad n > 0. \tag{3.50}$$

It is useful to introduce a wave function $\phi_s(\vec{r})$ with the so-called intermediate normalization,

$$\Psi(\vec{r}, t) = \phi_s(\vec{r})\langle\phi_s|\phi_s\rangle^{-1/2} \exp\left(-\frac{iE_s t}{\hbar}\right), \tag{3.51}$$

$$\phi_s(\vec{r}) = \sum_{n=0}^{\infty} \phi^{(n)}(\vec{r}), \tag{3.52}$$

$$\left\langle \phi^{(0)} \middle| \phi^{(0)} \right\rangle = 1, \tag{3.53}$$

$$\left\langle \phi^{(0)} \middle| \phi^{(n)} \right\rangle = 0, \quad n > 0. \tag{3.54}$$

Then, it can be calculated that

$$\xi^{(0)} = \phi^{(0)}, \tag{3.55}$$

$$\xi^{(1)} = \phi^{(1)}, \tag{3.56}$$

$$\xi^{(2)} = \phi^{(2)} - \frac{1}{2}\left\langle \phi^{(1)} \middle| \phi^{(1)} \right\rangle \phi^{(0)}, \tag{3.57}$$

$$\xi^{(3)} = \phi^{(3)} - \frac{1}{2}\left\langle \phi^{(1)} \middle| \phi^{(1)} \right\rangle \phi^{(1)} - \frac{1}{2}\left[\left\langle \phi^{(1)} \middle| \phi^{(2)} \right\rangle + \left\langle \phi^{(2)} \middle| \phi^{(1)} \right\rangle\right] \phi^{(0)}, \ldots . \tag{3.58}$$

The wave function normalization to the appropriate order must be considered while calculating the expectation values. Now we are interested in the solution of (3.41) using time-dependent perturbation theory,

$$\left[H^{(0)}(\vec{r}) - i\hbar\left(\frac{\partial}{\partial t}\right)\right] \Psi^{(0)}(\vec{r}, t) = 0, \tag{3.59}$$

$$\left[H^{(0)}(\vec{r}) - i\hbar\left(\frac{\partial}{\partial t}\right)\right] \Psi^{(n)}(\vec{r}, t) + H^{(1)}(\vec{r}, t)\Psi^{(n-1)}(\vec{r}, t) = 0, \quad n > 1, \tag{3.60}$$

and we know that

$$\sum_{k=0}^{n} \left\langle \Psi^{(k)} \middle| \Psi^{(n-k)} \right\rangle = 0, \;\; n > 0. \tag{3.61}$$

A careful and consistent treatment of the secular and normalization terms that arise in the case of time-dependent perturbation has been given by Langhoff [39]. Time-dependent generalizations of (3.45) to (3.47) obtain. Considering a perturbation with sinusoidal time dependence of frequency ω,

$$H^{(1)}(\vec{r}, t) = H^{(1)}(\vec{r})[\exp(i\omega t) + \exp(-i\omega t)], \tag{3.62}$$

one has,

$$\phi^{(1)}(\vec{r}, t) = \phi_{+1}^{(1)}(\vec{r})e^{i\omega t} + \phi_{-1}^{(1)}(\vec{r})e^{-i\omega t}, \tag{3.63}$$

$$\phi^{(2)}(\vec{r}, t) = \phi_{+1}^{(2)}(\vec{r})e^{2i\omega t} + \phi_{-1}^{(2)}(\vec{r})e^{-2i\omega t} + \phi_{0}^{(1)}(\vec{r}), \ldots, \tag{3.64}$$

with

$$\left(H^{(0)}(\vec{r}) - E_0 \pm \hbar\omega\right)\phi_{\pm 1}^{(1)} = \left(E^{(1)} - H^{(1)}(\vec{r})\right)\phi^{(0)}, \tag{3.65}$$

$$\left(H^{(0)}(\vec{r}) - E_0 \pm 2\hbar\omega\right)\phi_{\pm 2}^{(2)} = \left(E^{(1)} - H^{(1)}(\vec{r})\right)\phi_{\pm 1}^{(1)} + E_{\pm 2}^{(2)}\phi^{(0)}, \ldots . \tag{3.66}$$

As can be seen, the first corrections involve changers to the energy of $\pm\hbar\omega$, the second order shifts are $\pm 2\hbar\omega$, etc. e.g.,

$$E_{\pm 2}^{(2)} = \left\langle \phi^{(0)} \middle| H^{(1)}(\vec{r}) \middle| \phi_{\pm 1}^{(1)} \right\rangle , \dots . \tag{3.67}$$

The standard method of solution is to expand the perturbed functions in the complete set of eigenfunctions of the unperturbed Hamiltonian, $H^{(0)}(\vec{r})$. Using static perturbation theory, if we choose the orbital $\xi^{(0)}(\vec{r}) \equiv \phi_j(\vec{r})$ in (3.55) we will have

$$\xi_j^{(1)}(\vec{r}) = \sum_{\beta \neq j} \frac{\langle \phi_\beta | H^{(1)} | \phi_j \rangle}{E_j^{(0)} - E_\beta^{(0)}} \, \phi_\beta(\vec{r}). \tag{3.68}$$

For the case of long wavelength monochromatic electromagnetic waves incident on a dilute gas of atoms using this approach, the lowest order susceptibilities are

$$\chi^{(1)}(j;\omega) = -ne^2 \sum_{\beta \neq j} \frac{\vec{r}_{j\beta} v_{j\beta}}{(\omega_{\beta j} \pm \omega)}, \tag{3.69}$$

$$\chi^{(2)}(j;\omega) = -\frac{ne^3}{4} \sum_{\beta \neq j} \left[\frac{2\vec{r}_{j\beta} v_{j\beta} v_{jj}}{\omega_{\beta j}(\omega_{\beta j} \pm \omega)} + \frac{\vec{r}_{jj} v_{j\beta} v_{\beta j}}{(\omega_{\beta j} \pm \omega)^2} \right] + \frac{ne^3}{4} \sum_{\beta \neq j} \sum_{l \neq j} \{ \frac{2\vec{r}_{j\beta} v_{\beta l} v_{lj}}{\omega_{\beta j}(\omega_{lj} \pm \omega)} + \frac{\vec{r}_{\beta j} v_{\beta l} v_{lj}}{(\omega_{\beta j} \pm \omega)(\omega_{lj} \pm \omega)} \}, \tag{3.70}$$

where n is the number density of atoms, and

$$\vec{r}_{kl} = \langle k^{(0)} | \vec{r} | l^{(0)} \rangle, \tag{3.71}$$

And

$$v_{kl} = \vec{r}_{kl} \,.\, \hat{\eta}, \tag{3.72}$$

is a unit vector in the direction of the electric field, and $\pm$ used for the summation of the terms that have both signs.

3.5. Time-Dependent LDA (TDLDA)

It was assumed in the previous section that the eigenvalues and eigenfunctions for the unperturbed states are exactly known. Obviously, this is rarely the case, and the unperturbed eigenvalues and eigenfunctions are calculated in some approximate way, usually using a variational scheme such as Hatree-Fock, or LDA. In these cases, using a perturbation scheme that is consistent with the variational

principle to obtain the unperturbed states is important. For example, for Hartree-Fock the starting point would be the Dirac-Fernkel time-dependent variational method [40].

A local density approximation for the frequency dependent exchange-correlation potential using linear response theory was provided by Gross and Kohn [41]. Assuming an unperturbed inhomogeneous electronic system, $n^{(0)}(\vec{r})$ is the density of this system in a nondegenerate ground state of the external static potential $U(\vec{r})$. If we have a small perturbing potential $V_{ext}(\vec{r},t)$, and corresponding density response $n^{(1)}(\vec{r},t)$, we get the relation between the Fourier components of these two quantities as

$$n^{(1)}(\vec{r},\omega) = \int d^3r'\, \chi(\vec{r},\vec{r}';\omega)\, n^{(1)}(\vec{r},t) V_{ext}(\vec{r}',\omega), \tag{3.73}$$

where the $\chi(\vec{r},\vec{r}';\omega)$ is the density-density response function (defined below). In the local density approximation, the density $n^{(0)}(\vec{r}) + n^{(1)}(\vec{r},t)$ results from a system which contains non-interacting particles in a single-particle potential $V_{eff}^{(0)}(\vec{r}) + V_{eff}^{(1)}(\vec{r},t)$. Thus,

$$n^{(1)}(\vec{r},\omega) = \int d^3r'\, \chi_{KS}(\vec{r},\vec{r}';\omega)\, V_{eff}^{(1)}(\vec{r}',\omega), \tag{3.74}$$

where $\chi_{KS}(\vec{r},\vec{r}';\omega)$ is the density-density response function of the non-interacting Kohn-Sham ground state corresponding to $V_{eff}^{(1)}(\vec{r},t)$ that is given in terms of the Kohn-Sham eigenfunctions and eigenvaues,

$$\chi_{KS}(\vec{r},\vec{r}';\omega) = \sum_{i,j} (f_i - f_j) \frac{\psi_i(\vec{r})^* \psi_j(\vec{r}) \psi_j(\vec{r}')^* \psi_i(\vec{r}')}{\hbar\omega - (\epsilon_j - \epsilon_i) + i\delta}, \tag{3.75}$$

where the $f_i (= 0,1)$ are the occupation numbers.

The exchange-correlation part of $V_{eff}^{(1)}$ is defined as

$$V_{eff}^{(1)}(\vec{r},\omega) = V_{ext}(\vec{r},\omega) + 2\int \frac{n^{(1)}(\vec{r}',\omega)}{|\vec{r}-\vec{r}'|} d^3r' + \delta V_{xc}^{(1)}(\vec{r},\omega), \tag{3.76}$$

$$\delta V_{xc}^{(1)}(\vec{r},\omega) = \int d^e r' f_{xc}(\vec{r},\vec{r}';\omega)\, n^{(1)}(\vec{r}',\omega), \tag{3.77}$$

where f_{xc} depends upon the unperturbed ground state density,

$$f_{xc}(\vec{r},\vec{r}';\omega) = \chi_{KS}^{-1}(\vec{r},\vec{r}';\omega) - \chi^{-1}(\vec{r},\vec{r}';\omega) - \frac{1}{|\vec{r}-\vec{r}'|}\ , \qquad \textbf{(3.78)}$$

assuming that the inverse response functions exist. In case of an homogeneous electron gas f_{xc} is known, and the Lindhard expression takes the place of χ_{KS}. So,

$$f_{xc}^{h}(\vec{q},\omega) = -\left(\frac{4\pi}{q^2}\right) G(\vec{q},\omega), \qquad \textbf{(3.79)}$$

where $G(\vec{q},\omega)$ is the local field factor [42].

Assuming (i) $n^{(0)}(\vec{r})$ is sufficiently slowly varying so that $f_{xc}{\sim}f_{xc}^{h}$, and (ii) $n^{(1)}(\vec{r}',\omega)$ is sufficiently slowly varying that can be replaced by $n^{(1)}(\vec{r},\omega)$ in (3.77), the time-dependent local density approximation for the electron gas is obtained,

$$\delta V_{xc}^{(1)}(\vec{r},\omega) = f_{xc}^{h}\left(q=0,\omega;n^{(0)}(\vec{r})\right)n^{(1)}(\vec{r},\omega). \qquad \textbf{(3.80)}$$

It is obvious that these assumptions will break down when the frequency of the applied field is near an electronic resonance of the system. Nevertheless, this scheme provides very accurate results for linear and nonlinear response in many situations.

The time-dependent local density approximation (TDLDA) is actually linearized time-dependent. In other words, the prefix *time-dependent* is used to denote the process of calculating the potential is self-consistently. This method of calculating polarizability and cross section is called the time-dependent local density approximation (TDLDA).

3.6. Photoionization

As we discussed, the time-dependent local density approximation (TDLDA) can be used to calculate the response of a system (e.g., atoms or molecules) to a time-dependent electric field. Consider a response of a single atom to electromagnetic waves. Dipole polarizability, which is a function of frequency, is used to calculate photoionization cross section. For small frequency the polarizability is real, but for large frequency the atom can absorb the radiation and photoionize an atom. In this case the polarizability is a complex quantity and its imaginary part is related to the photoionization cross section,

$$\sigma_{PI} = \frac{4\pi\omega}{c} Im(\alpha_d). \quad \textbf{(3.81)}$$

The LDA expression for dipole polarizability as a function of ω, using (2.67) and(2.68), is

$$\alpha_d(\omega) = e^2 \sum_{im} |\langle i|z|m\rangle|^2 f_i(1-f_m)\left\{\frac{1}{\lambda_{mi}+\hbar\omega+i\delta}+\frac{1}{\lambda_{mi}-\hbar\omega-i\delta}\right\} \quad \textbf{(3.82)}$$

where δ is infinitesimal, and $\lambda_{mi} = E_m - E_i$. By calculating the imaginary part of (3.82) and using (3.81) with the Fermi golden rule expression for the absorption cross section, we have

$$\sigma_{absorption} = \frac{4\pi^2 e^2}{c} \sum_{im} |\langle i|z|m\rangle|^2 f_i(1-f_m)\,\delta(\hbar\omega-\lambda_{mi}). \quad \textbf{(3.83)}$$

Now we define the threshold frequency ω_{th} in relation to the ionization energy of the atom as $\hbar\omega_{th} = E_{ionization}$. Using LDA the ionization energy can be calculated very accurately. It can be done by finding the difference between the LDA self-consistent calculated ground state energy of the atom with N electrons, and another calculation for atom with N-1 electrons,

$$E_G(N-1) - E_G(N) = E_{ionization.} \quad \textbf{(3.84)}$$

It can be shown that the eigenvalue of the highest occupied density functional orbital is the exact ionization potential [43].

In this research, the dipole polarizability is calculated using TDLDA, which is a complex quantity for frequencies larger than the ionization threshold. Since the LDA formalism is good for ground state properties but not for the excited state properties, TDLDA is used for photoionization cross section calculations.

Consider the LDA expression for the polarizability as a function in (3.82). In the case of the LDA calculation, the perturbation is z instead of the self-consistent potential. The factor f_i denotes that the initial state $|i\rangle$ is occupied, and factor $(1-f_m)$ denotes that the final state $|m\rangle$ is empty so it is equal to unity. Thus, the summation of matrix elements for finding polarizability is

$$\alpha_d(\omega) = e^2 \sum_i f_i \int d^3r\, \psi_i^*(\vec{r}) z \left[\psi_i^{(1,+)}(\vec{r}) + \psi_i^{(1,-)}(\vec{r})\right], \tag{3.85}$$

$$\psi_i^{(1,\pm)}(\vec{r}) = \sum_m (1 - f_m) \frac{\psi_m(\vec{r})\langle m|z|i\rangle}{\lambda_{mi} \pm (\hbar\omega + i\delta)}. \tag{3.86}$$

The first order change in $\psi_i^{(1,\pm)}(\vec{r})$ is calculated by operating on both sides of (3.86) by $[H_0 - E_i \pm \hbar\omega]$, so that

$$[H_0 - E_i \pm \hbar\omega]\, \psi_i^{(1,\pm)}(\vec{r}) = \sum_m (1 - f_m)\psi_m(\vec{r})\langle m|z|i\rangle = z\psi_i(r) - \sum_m f_m \psi_m(\vec{r})\langle m|z|i\rangle. \tag{3.87}$$

The right hand side shows that the occupied states must be subtracted out, but, it turns out that this term is quite small, so there is no need to restrict the summation in (3.87) over *m* to unoccupied states. Then, averaging (3.82) with the expression obtained by interchanging the summation variables *i* and *m*,

$$\alpha_d(\omega) = \frac{e^2}{2} \sum_{im} |\langle i|z|m\rangle|^2 \begin{bmatrix} f_i(1 - f_m)\left\{\dfrac{1}{\lambda_{mi} + \hbar\omega + i\delta} + \dfrac{1}{\lambda_{mi} - \hbar\omega - i\delta}\right\} + \\ f_m(1 - f_i)\left\{\dfrac{1}{\lambda_{mi} + \hbar\omega + i\delta} + \dfrac{1}{\lambda_{mi} - \hbar\omega - i\delta}\right\} \end{bmatrix}, \tag{3.88}$$

or

$$\alpha_d(\omega) = \frac{e^2}{2} \sum_{im} |\langle i|z|m\rangle|^2 [f_i + f_m]\left\{\frac{1}{\lambda_{mi} + \hbar\omega + i\delta} + \frac{1}{\lambda_{mi} - \hbar\omega - i\delta}\right\}. \tag{3.89}$$

By interchanging the dummy variables *i* and *m*, it can be shown that $f_i = f_m$ so that the final expression becomes

$$\alpha_d(\omega) = e^2 \sum_{im} f_i |\langle i|z|m\rangle|^2 \left\{\frac{1}{\lambda_{mi} + \hbar\omega + i\delta} + \frac{1}{\lambda_{mi} - \hbar\omega - i\delta}\right\}. \tag{3.90}$$

By comparing (3.90) and (3.82) we see that there is no longer a restriction that the final state *m* must be unoccupied. For example, in the argon atom, the 3s and 3p subshells are fully occupied. In calculating polarizability, virtual transitions $3s \rightarrow 3p$ and $3p \rightarrow 3s$ are included with the former positive and the later negative. Thus, they cancel each other exactly, and do not affect the result. But this cancellation only occurs for the real part of the polarizability. But for calculating the photoionization cross section the

imaginary part of the polarizability is used, and unwanted transitions in photoionization spectra are excluded by avoiding the discrete values of frequency in the summation where they occur.

In TDLDA, the inhomogeneous differential equation in (3.87) is replaced by

$$[H_0 - \lambda_i \pm \hbar\omega]\,\psi_i^{(1,\pm)}(\vec{r}) = V_{sc}(\vec{r},\pm\omega)\psi_i(\vec{r}), \tag{3.91}$$

$$n^{(1)}(\vec{r},\pm\omega) = \sum_i f_i\left[\psi_i^*(\vec{r})\psi_i^{(1,\pm)}(\vec{r}) + \psi_i(\vec{r})\psi_i^{(1,\mp)*}(\vec{r})\right], \tag{3.92}$$

$$\alpha_d(\omega) = e^2\int d^3r\, z n^{(1)}(\vec{r},\omega), \tag{3.93}$$

where $V_{sc}(\vec{r},\pm\omega)$ is the self-consistent potential.

There are two possibilities in the solution of (3.93). First if $\lambda_i \pm \hbar\omega < 0$, then $\psi_i^{(1,\pm)}(\vec{r}\to\infty)\to 0$, and there will be no photoionization. The other possibility is that $\lambda_i \pm \hbar\omega > 0$; in this case the photoionization can occur for the electrons in i shell. In this process the electron absorbs the ingoing electromagnetic wave and leaves the atom. Therefore, we need to solve (3.91) with the ingoing boundary condition. The Greens functions for the atomic orbitals can be written as

$$G(\vec{r},\vec{r}',E) = \sum_j \frac{\psi_j(\vec{r})\psi_j^*(\vec{r}')}{E_j - E - i\delta}\ , \tag{3.94}$$

$$\psi_i^{(1,-)}(\vec{r}) = \epsilon\phi_{\vec{k}}(\vec{r}) + \int d^3r' G(\vec{r},\vec{r}',E_i+\hbar\omega)\, V_{sc}(\vec{r}',-\omega)\psi_i(\vec{r}'), \tag{3.95}$$

$$k^2 = \omega + E_i/\hbar. \tag{3.96}$$

Note also that this same procedure can be used to find $\psi_i^{(1,+)}(\vec{r})$.

The factor $i\delta$ in the Greens function leads to the ingoing boundary condition. The first term on the right hand side of (3.95) is only present when $k^2 > 0$, because only then is there a homogeneous solution to the homogeneous differential equation. The eigenfunction $\phi_{\vec{k}}(\vec{r})$ is the electron final state eigenfunction, when is exits the atom. Note that ϵ, the coefficient of the homogeneous solution in (3.95), can take any value and (3.95) is still a solution. Thus, the value of ϵ should be chosen by physical arguments to insure the correct boundary conditions.

Since the homogeneous term corresponds to the incoming plane wave in the scattering case, and we do have any incoming plane wave in photoionization case, the value for ϵ is zero. The electron eigenfunctions for the outgoing continuum states, which are discussed explicitly in chapter 2, are

$$\phi_{\vec{k}}(\vec{r}) = \sum_{l} (2l+1)(-i)^l \, u_l(kr) P_l\left(\hat{k}.\hat{r}\right), \tag{3.97}$$

$$\psi_i^{(1,-)}(r) = \sum_{l'=|l-1|}^{l+1} c_{l'm} R_{l'}^{(1,-)}(kr) Y_{l'm}(\theta,\phi). \tag{3.98}$$

The radial part $u_l(kr)$ is the solution of the homogeneous differential equation.

$$\left\{-\frac{\partial^2}{\partial r^2} + \frac{l(l+1)}{r^2} + V(r) - k^2\right\}\left(r u_l(kr)\right) = 0, \tag{3.99}$$

and the asymptotic form for the solution is

$$u_l(kr \to \infty) \to \frac{1}{kr} sin\left(kr + \delta_l(k) - \frac{l\pi}{2}\right). \tag{3.99}$$

The equation (3.99) is second order, so it has two solutions; the second one, $v_l(kr)$, has the asymptotic limit $-\frac{1}{kr} cos\ (kr + \delta_l(k) - \frac{l\pi}{2})$ and is irregular at origin. In any case, to obtain the correct asymptotic form , the outgoing wave solution is

$$w_l(kr) = u_l(kr) + i v_l(kr). \tag{3.100}$$

The radial part of the Green's function, after averaging over angle, is

$$G_l(r, r'; \omega) = \frac{k}{4\pi} \, u_l(kr_<) w_l(kr_>) \, , \tag{3.101}$$

where $r_<$ and $r_>$ are the lesser and greater of (r, r'), respectively. In the photoionization (ingoing boundary condition) case the solution for inhomogeneous differential equation using Green's function's method is

$$R_{l'}^{(1,-)}(kr) = \left\{ \begin{matrix} k w_{l'}(kr) \int_0^r r'^2 dr' u_{l'}(kr') v_{sc}(r', -\omega) R_{nl}(r') + \\ k u_{l'}(kr) \int_r^\infty r'^2 dr' w_{l'}(kr') v_{sc}(r', -\omega) R_{nl}(r') \end{matrix} \right\}, \tag{3.102}$$

and the asymptotic form is

$$R_{l'}^{(1,-)}(kr; r \to \infty) = Dw_{l'}(kr), \tag{3.103}$$

$$D = k\int_0^\infty r'^2 dr' u_{l'}(kr') v_{sc}(r', -\omega) R_{nl}(r'). \tag{3.104}$$

These equations were derived and solved by Zangwill and Soven [44].

3.6.1. Numerical Methods

In order to solve homogeneous equation, we define

$$g(kr) = kru_l(kr), \tag{3.105}$$

so that the numerical solution in the asymptotic $(r \to \infty)$ region is

$$g(kr; r \to \infty) = C_g kr\, cos(\delta)\,[j_l(kr) - tan(\delta)\,\eta_l(kr)] \tag{3.106}$$

$$= C_g \sin\left(kr + \delta - \frac{l\pi}{2}\right), \tag{3.107}$$

where j_l and η_l are spherical Bessel and Neumann functions, respectively. Also, this asymptotic solution has two constants; amplitude C_g and phase shift δ. These two constants are obtained by fitting the numerical solution at two different points to the analytical formula (3.107). This procedure is to calculate the eigenfunction which is a solution to the inhomogeneous equation. Now, for solving inhomogeneous equation we define a new variable as follows to be the solution for inhomogeneous equation with ingoing boundary conditions,

$$X(r) = kr\, R^{(1,-)}(kr). \tag{3.108}$$

We start of by calculating the LDA solution. In this case all the radial functions ($R^{(1,\pm)}$) are real, except those states where the electron is in an outgoing wave. Only the outgoing wave has complex part that contributes in calculating cross section. The method is a simple variation which was suggested by Senatore and Subbaswamy [45] as follows:

1. Define $X = ag + f$, where $g(r)$and $f(r)$ are determined as follows:

2. $g(r)$ is the solution for homogeneous equation as $g'' = Ag$ by iterating outwards form the origin with the initial conditions that $g_0 = 0$ and $g_1 = 1$. The asymptotic form for that,

$$g(r \gg 1) \rightarrow C_g \sin\left(kr + \delta - \frac{l\pi}{2}\right). \quad \textbf{(3.109)}$$

3. The constants are obtained by fitting the numerical solution at two points of the analytical form.
4. $f(r)$ is calculated by iterating the inhomogeneous equation $f'' = Af + B$ outwards from the origin with the initial values of $f_0 = 0, f_1 = 0$, where $B = krv_{sc}R_{nl}$ for the outgoing wave. The asymptotic form for $f(r)$ is

$$f(r \gg 1) \rightarrow C_f \sin\left(kr + \delta' - \frac{l\pi}{2}\right). \quad \textbf{(3.110)}$$

5. The constant a, and the function $X(r)$ are

$$a = -\frac{C_f}{C_g} e^{i(\delta - \delta')}, \quad \textbf{(3.111)}$$

$$X(r) = f(r) - \frac{C_f}{C_g} e^{i(\delta - \delta')} g(r). \quad \textbf{(3.112)}$$

6. By substituting the asymptotic relation for $f(r)$ and $g(r)$in (3.112) we get

$$X(r \gg 1) = C_f \left[sin\left(kr + \delta' - \tfrac{l\pi}{2}\right) - e^{i(\delta - \delta')} sin\left(kr + \delta - \tfrac{l\pi}{2}\right) \right]. \quad \textbf{(3.113)}$$

Since the $e^{(-ikr)}$ term is canceled, (3.114) is pure outgoing wave,

$$X(r \gg 1) = De^{i(kr + \delta - \frac{l\pi}{2})}, \quad \textbf{(3.114)}$$

where,

$$D = C_f si\, n(\delta' - \delta). \quad \textbf{(3.115)}$$

The function $X(r)$ is regular at origin and, as r become larger, it becomes an outgoing wave; also it is a solution to the inhomogeneous differential equation. Since $X(r)$ has an imaginary part, it contributes to the photoionization cross section. Then, equation (3.81) can be rewritten as,

$$\sigma(\omega) = 4\pi\alpha_f \hbar\omega \int d^3r\, z\, Im\{n^{(1)}(\vec{r},\omega)\}, \quad \textbf{(3.116)}$$

where $\alpha_f$is fine structure constant, and the imaginary part of $X(r)$ contributes to the imaginary part of the perturbed density $n^{(1)}$.

Coefficient D is given in to different relations, (3.104) and (3.115). Since these two equations give the same numerical result, the theory is consistent. Also this identity provides a check on numerical accuracy of the calculation.

The above procedure is the LDA calculation of the cross section, where the external potential is z instead of v_{sc}. We use a somewhat different procedure if the full self-consistent field is used for external potential in (3.91), since both $n^{(1)}$ and v_{sc} are complex. In this case, every function in $R^{(1,\pm)}(r)$ is complex and contributes in the cross section calculation. As a result, the numerical procedure needs to be different when $B(r) \equiv krv_{sc}R_{nl}(r)$ is complex. Specifically, the procedure is:

1. $\lambda_i \pm \omega < 0$ the eigenfunctions $R^{(1,\pm)}(r)$ go to zero outside of the atom.

a. Define $= ag + f$, with the same condition that discussed before.

b. By integrating outward form origin $g_<$, $g'_<$ and $f_<$, $f'_<$ are determined.

c. Define $X = ag + f$ such that:

$g'' = Ag$ with the boundary conditions: $g_N = 0, g_{N-1} = 1$,

$f'' = Af + B$ with the boundary conditions: $f_N = 0, f_{N-1} = 0$,

and determine $g_>$, $g'_>$ and $f_>$, $f'_>$.

d. Now we have values for $X_>$ and $X_<$. The functions and their derivative must be equal

$$ag_< - bg_> = -f_< + f_>, \quad \textbf{(3.117)}$$

$$ag'_< - bg'_> = -f'_< + f'_>, \quad \textbf{(3.118)}$$

where *a* and *b* are unknown. The quadratic equation are solved to find these two unknown constant; thus, the solution for $X(r)$is obtained for all values of r.

2. For $\lambda_i \pm \omega > 0$, the eigenfunctions are outgoing waves and the procedure is the same as in LDA with some modifications. Like the previous case $g(r)$ is real since this function does not involve $B(r)$. $f(r)$ is complex and has different asymptotic form,

$$f(r \gg 1) \rightarrow C_{f_1} sin\left(kr + \delta_1 - \frac{l\pi}{2}\right) + i\, C_{f_2} sin\left(kr + \delta_2 - \frac{l\pi}{2}\right). \quad \textbf{(3.119)}$$

The real and imaginary parts of $f(r)$ has different phase shifts (δ_1, δ_2), so the coefficient a in (3.112) becomes

$$a = -\frac{e^{i\delta}}{C_g}\left[C_{f_1} e^{-i\delta_1} + iC_{f_2} e^{-i\delta_2}\right], \quad \textbf{(3.120)}$$

$$X(r) = ag(r) + f(r), \quad \textbf{(3.121)}$$

$$D = C_{f_1} \sin(\delta_1 - \delta) + iC_{f_2} \sin(\delta_2 - \delta). \quad \textbf{(3.122)}$$

By using the self-consistent potential in computing the photoionization cross section, all the eigenfunctions will be complex. However, the numerical methods are the same, except that complex numbers are used in computing.

4. RESULTS AND DISCUSSION

4.1. Introduction

In this research, since the interest is in low-energy photoionization, starting at the threshold of the valence shells, it is crucial to employ a theoretical model which includes coupling of the atomic photoionization channels with the huge low-energy plasmon resonances of the surrounding fullerene [2,3,4]. Furthermore, since the valence electron wave functions of an atom are typically of large spatial extent, it is necessary to allow for the possibility of mixing of the initial state wave functions of the atom with those of the C_{60} shell, i.e., hybridization of the atomic wave functions. Thirdly, the inclusion of correlation is of importance to ensure the accuracy of the calculations. A methodology which includes all of these effects is our jellium-based time-dependent local density technique which includes interchannel coupling, hybridization and sig-

nificant aspects of correlation [46]. This methodology has been used in the past and has predicted a huge increase of atomic photoionization channels owing the interaction with the plasmons of C_{60} (interchannel coupling) [47,48,49] along with significant effects of hybridization [46,50].

In the following section, a brief discussion of the theory and calculational methodology are presented. Next a detailed account of the results are presented and discussed.

4.2. Calculation

Nonrelativistic density functional theory is used to obtain the structure of the C_{60} fullerene cage. In the formulation for the C_{60} ground state, the four valence electrons ($2s^2 2p^2$) of each carbon atom are delocalized, a total of 240 delocalized electrons, while the core C^{4+} ions (each consisting of a carbon nucleus plus two very tightly bound 1s electrons) are represented by a classical spherical jellium shell (with radius $R = 3.5$ Å , thickness Δ), and a constant potential depth V_0 [51]; the details of the calculation were presented in [17]. The energy levels and designations of the electronic states of the free C_{60} molecule are shown in Table4.1. The entrapped noble gas atom is placed at the center of the C_{60} shell and the Kohn-Sham equations for the 240 + N-electron system (240 cage electrons and N=2 for He, N=10 for Ne, N=18 for Ar, N=36 for Kr, N=54 for Xe,…) are then solved to obtain the ground state wave function of the system in the local density approximation (LDA). As the exact form of V_{xc} is unknown in a local formalism like LDA (since the exact exchange interaction is non-local), A widely-used parametric exchange-correlation potential is used in the calculation [52]. The parameters V_0 and Δ are determined by requiring both charge neutrality and obtaining the experimental value, 7.54 eV, for the first ionization potential. This procedure yields Δ=1.5, in excellent agreement with experiment [53].

Table 4. 1. Calculated binding energies of the occupied states of free C_{60} in atomic units (au).

1s	-1.392378
1p	-1.369104
1d	-1.322853
1f	-1.254177
1g	-1.163832
1h	-1.052725

1i	-0.921855
1j	-0.772279
2s	-0.645068
2p	-0.618723
1k	-0.605075
2d	-0.567211
2f	-0.491933
1l	-0.421323
2g	-0.394359
2h	-0.276164

To remove the unphysical self-interactions in the LDA potential, a self-interaction correction was introduced into the potential [54,55]. The importance of doing this is that the potential with this correction has the correct asymptotic form. However, since the self-interaction correction is orbital-dependent, this renders the LDA potential orbital specific, i.e., electrons in the different states are subject to somewhat different potentials.

A time-dependent LDA (TDLDA) method [12] is employed to calculate the dynamical response of the system to the external dipole field, i.e., the photoionization cross section. The perturbation z, the dipole interaction for linearly polarized light, induces a frequency-dependent complex change in the electron density arising from dynamical electron correlations. This can be written, using the LDA susceptibilityχ_0, as

$$\delta n(\vec{r};\omega) = \int \chi_0(\vec{r},\vec{r}';\omega)\delta V(\vec{r}';\omega)d^3r' \quad \textbf{(4.1)}$$

With

$$\delta V(\vec{r}';\omega) = z + \delta V'(\vec{r}';\omega) = z + \int \frac{\delta n(\vec{r}';\omega)}{|\vec{r}-\vec{r}'|}d^3r' + \left[\frac{\partial V_{xc}}{\partial n}\right]_{n=n_0}\delta n(\vec{r};\omega) \quad \textbf{(4.2)}$$

where the second and third terms on the right-hand side are, respectively, the induced change of the Coulomb and the exchange-correlation potentials. In addition to the external perturbation z, δV also includes the dynamical field produced by important electron correlations. The photoionization cross section is then calculated as the sum of independent partial cross sections $\sigma_{nl\to kl'}$ corresponding to a dipole transition $nl \to kl'$ as

$$\sigma_{PI} = \sum_{nl} \sigma_{nl \to kl'} \approx \sum_{nl} (2l+1) |\langle \phi_{kl'} | \delta V | \phi_{nl} \rangle|^2 \qquad \textbf{(4.3)}$$

where details of the calculation of the continuum wave functions $\phi_{kl'}$ is given in [17]. Clearly, replacing δV in (4.4) by z yields the LDA cross section that entirely omits any correlation.

4.3. Valence Photoionization of Noble Gas Atoms Confined in the Fullerene C_{60}

4.3.1. He@C_{60}

Using the density functional methodology, described above, calculations have been performed for the energies and wave functions of the ground states of the free He atom and the free C_{60} molecule, along with the energy levels and wave functions for He@C_{60}. In the combined system, He@C_{60}, an interesting phenomenon occurs – hybridization. This effect is depicted in Figure4.1 where the wave functions of the free He 1*s* (localized in the atomic potential), the free C_{60} 2*s* (localized in the C_{60} shell potential), and the wave functions of these *s*-states in the combined He@C_{60} system, which are termed $1s^+$ and $1s^-$, are shown. It is clear from Figure4.1 that these *s*-state wave functions in the He@C_{60} system have significant amplitude in both the atomic and shell regions of the combined potential, i.e., a hybridized mixture of atomic and shell states. This phenomenon was seen earlier [50] and can be explained qualitatively *via* perturbation theory. The mixing coefficient from that point of view is the matrix element of the perturbing potential between the unperturbed atomic and shell states divided by the (unperturbed) energy difference. This suggests that the He 1s state, 1.028 au, lies roughly half way between the 1*s* (1.392 au) and 2*s* (0.645 au) of free C_{60} (see Table4.1), so there is no near-degeneracy. But, as seen in Figure4.1, there is a large overlap between He 1*s* and C_{60} 2s, which results a large interaction matrix element and significant hybridization. On the other hand, there is essentially no hybridization between the 1*s* of He and the 1*s* of C_{60}, even though the energy difference between these states is about the same as the 1*s* of He with the 2*s* of C_{60}, because there is almost no overlap between the two 1s wave functions. The fact that there is no hybridization between states of differing angular momentum results because the Hamiltonian of the system is spherically symmetric and,

thereby, commutes with the orbital angular momentum operator; thus, the matrix element of the Hamiltonian between states of different orbital angular momentum vanishes.

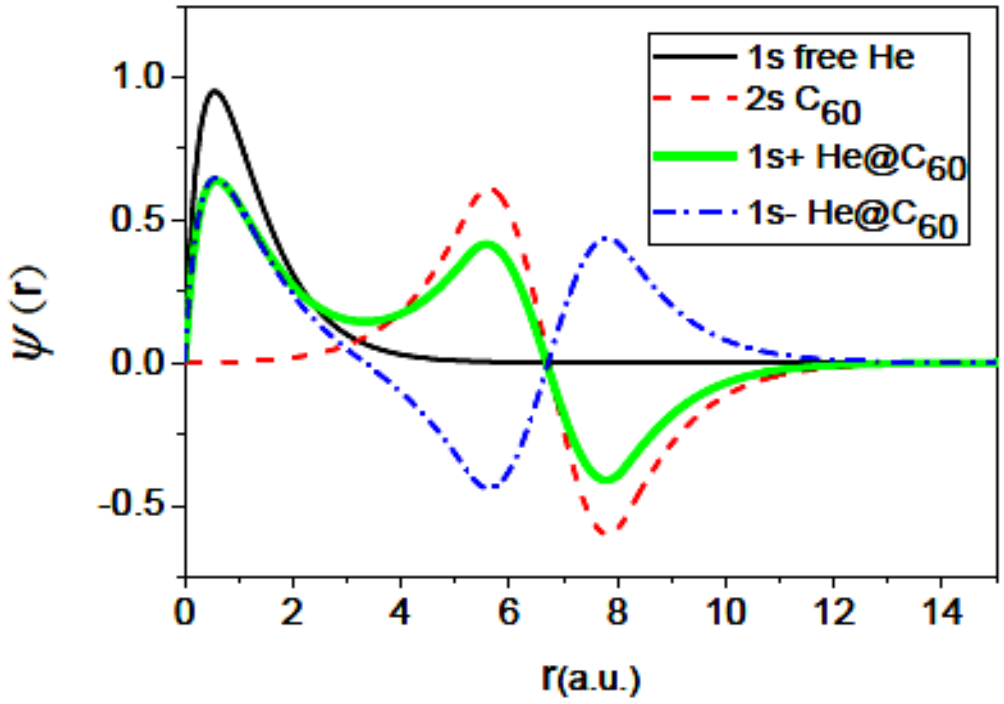

Figure4.1 Wave functions of 1s of free He, 2s of C_{60} and hybridized states of He@C_{60}

It is of interest to note that the binding energies of the two hybridized states, $1s^{+}$ and $1s^{-}$, are about 0.663 au and 0.687 au, quite close to the energy of the unperturbed C_{60} 2*s* state (0.645 au) but quite far from the 1*s* energy (1.028 au) of free He. This is not accidental. In the combined system, the potential of the He atom perturbs the shell states, while the shell potential perturbs the 1*s* of He. Since the shell potential is so much larger than the atomic potential, in a general sense, it is evident that, in the combined system, the atomic energy levels should be altered much more than the energies of the shell states. This is exactly what is found numerically for He@C_{60}. Furthermore, as a corollary, this implies that in cases where there is no hybridization, the atomic energies of the combined system will experience much greater changes from the unperturbed energies than what will be the case for the shell state energies.

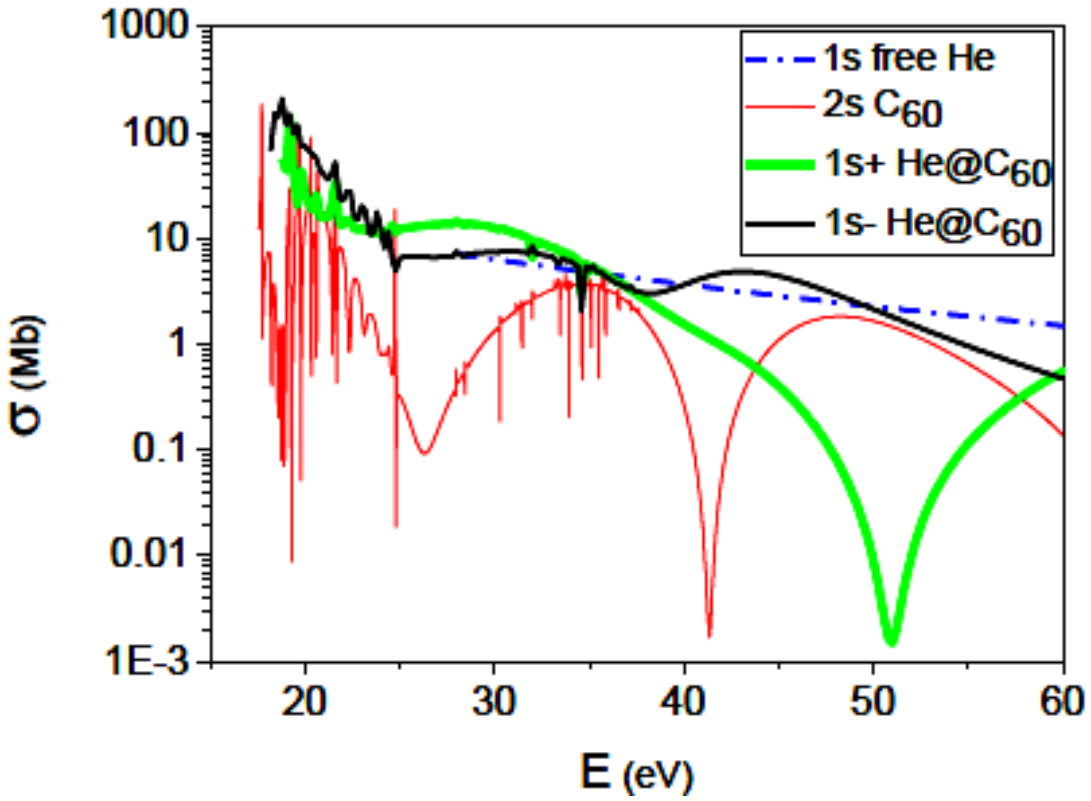

Figure 4.2 Cross sections of 1s of free He, 2s of C_{60} and hybridized states of He@C_{60}

Using these initial-state wave functions, the photoionization cross sections are obtained using the TDLDA methodology as described in the previous section. Since He has just a single 1*s* shell, and this 1*s* is hybridized, as discussed above, it is no longer possible to ask how the confining shell modifies the He photoionization cross section; all one can do is look at the cross sections of the various subshells of the combined He@C_{60} system. In Figure4.2, the cross sections for the hybridized states, $1s^{+}$ and $1s^{-}$, are shown, along with the cross sections of the states that mix to form these hybridizations, free He 1*s* and free C_{60} 2*s*. The free He 1s cross section is seen to be featureless and monotone decreasing from the threshold value of about 8 Mb. The free C_{60} 2*s* cross section is significantly larger, more than 30 Mb, in the threshold region (note the log scale), which is somewhat below the He 1s threshold, where it contributes to the well-known plasmon resonance in free C_{60} [2,3,4]. At higher energy, it falls off very rapidly, falling below the He 1*s* cross section around the He 1*s* threshold despite a second maximum in the 40 eV region contributing to the second (much smaller) C_{60} plasmon, and dropping much faster than He 1*s* at still higher energies. In addition,

the free C_{60} 2*s* cross section exhibits numerous minima which are analogous to the Cooper minima of atoms. Thus, since the mixing of these state in the $1s^+$ and $1s^-$ wave functions is roughly 50-50, it must be that the $1s^+$ and $1s^-$ cross sections emulate C_{60} 2*s* in the near-threshold region, where the C_{60} 2s cross section is by far the larger, and will be much closer to the He 1s cross section at higher energies for a similar reason; this is exactly what is seen in Figure 4.2. Near threshold both $1s^+$ and $1s^-$ cross sections are quite large, compared to He 1s, reflecting the influence of C_{60} 2*s*, and at the larger energies, they are close to He 1s. In the intermediate energy region, where the two unperturbed cross sections are comparable, the $1s^+$ and $1s^-$ cross sections are complicated owing the existence of interferences in the coherent addition of the matrix elements; the deep Cooper minimum in the $1s^+$ cross section at about 50 eV, which is not where the unperturbed C_{60} 2*s* cross section shows a Cooper minimum, exemplifies this behavior.

However, this cannot be the entire story. Looking carefully at Figure 4.2, it is noted that both the $1s^+$ and $1s^-$ cross sections maximize at about 100 Mb in the threshold region; far larger than the free C_{60} 2*s* cross section. It is, thus, evident that the $1s^+$ and $1s^-$ cross sections are not simply fractions of the free C_{60} 2*s* cross section determined by the squares of the relative amplitudes of the discrete C_{60} 2*s* and hybridized wave functions in the shell region, depicted in Figure 4.1. This implies that the change in the total potential engendered by the He atom inside the C_{60} cage changes not only the initial discrete wave function , e.g., hybridization, but also the final state wave functions and the interchannel coupling among them. It is known that interchannel coupling has a large effect upon the atomic photoionization cross sections of non-hybridized states trapped atoms in the plasmon region [3,56,4], so it is no surprise that significant interchannel coupling exists for hybridized states as well. And this is why the $1s^+$ and $1s^-$ cross sections are both significantly larger than the free C_{60} 2*s* cross section in threshold region which is also the energy region of the lower-energy C_{60} plasmon; the interchannel coupling caused mixing of the $1s^+$ and $1s^-$ channels with the matrix elements of the (very large) C_{60} photoionization channels contributing to the plasmon.

At the higher energies, shown in Figure 4.3, it is evident that both the $1s^+$ and $1s^-$ cross sections are dominated by the contribution of He 1*s*. The $1s^+$ and $1s^-$ cross sections are seen to be about equal in magnitude, except for the oscillations exhibited by both; oscillations not seen in the unperturbed He 1*s* cross section. These oscillations are known as confinement resonances, or confinement oscillations [57,58,55,59], and are the result of interferences of the continuum photoelectron wave emerging directly, and after reflection from the inner or outer edges of the confining potential. These oscillations are ubiquitous, and always occur for atoms confined in a potential [60,58]. The details of these confinement oscillations differ from atom to atom and even from subshell to subshell within a given atom. Looking at Figure 4.3, it is seen that the $1s^+$ and $1s^-$ cross sections exhibit these oscillations of the same amplitude and period, which simply reflects the geometry of the confining potential [57]. However, the details of the phases of these oscillations, exactly where the maxima and minima are, also involve the details of the atomic wave functions. This notion shall be reinforced as the photoionization cross sections of the other noble gases are presented below. Note also that interchannel coupling is not important for the atomic cross sections in the higher energy region where the C_{60} photoionization channels are not much larger than the atomic cross sections; here they are smaller so that any mixing does not cause any appreciable change in the atomic cross sections.

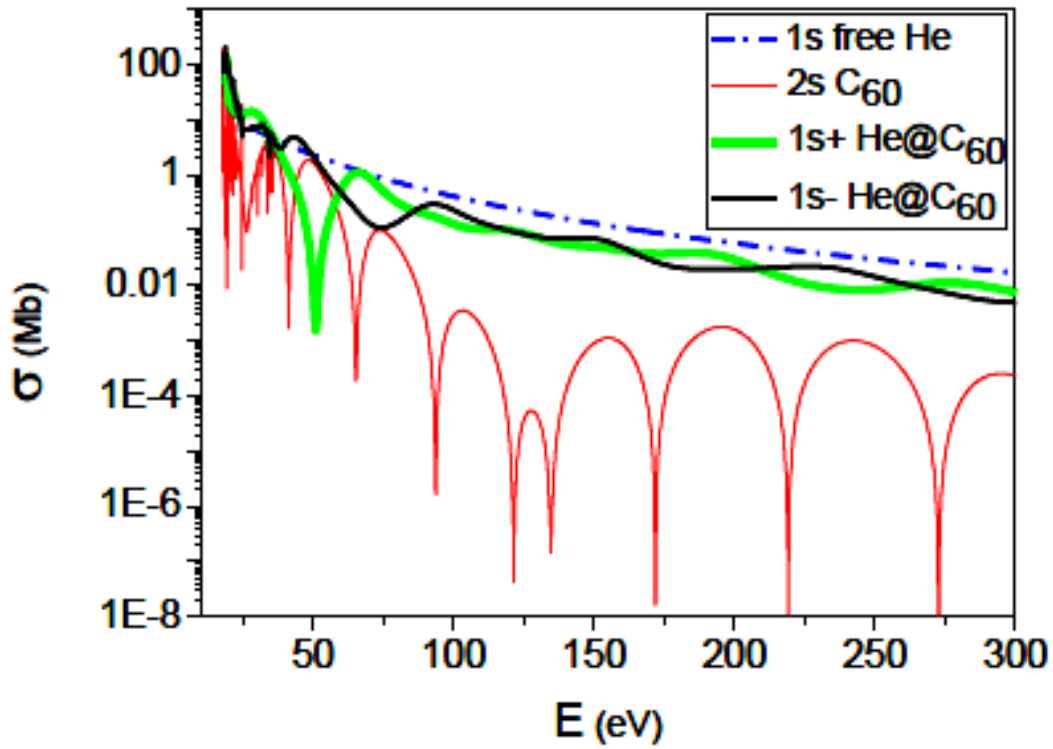

Figure4.3 Cross sections of 1s of free He, 2s of C_{60} and hybridized states of He@C_{60} at higher energies

4.3.2. Ne@C_{60}

Looking at Ne@C_{60}, the situation differs somewhat in that the entrapped atom, Ne in this case, is itself a multishell system. The 1*s* and 2*s* discrete wave functions, whose binding energies are calculated to be 33.17 au and 1.71 au respectively, do not exhibit any near-degeneracy with the energy levels of C_{60} (Table4.1) and do not overlap appreciably with the C_{60} 1*s* or 2*s* wave functions; as a result they are not hybridized.

The Ne 2*p* state, on the other hand, with energy 0.89 au, does overlap the C_{60} 2*p*, which is bound by 0.62 au, and is hybridized, much like the He 1*s* case. The situation is shown in Figure 4.4 where it is seen that the hybridized wave functions of the combined Ne@C_{60} system, labeled $2p^+$ and $2p^-$, are roughly a 50-50 admixture of Ne 2*p* and C_{60} 2*p*.

The binding energies of the two hybridized *p*-states of the Ne@C_{60} system are found to be 0.64 au and 0.66 au; quite close to the unperturbed 2*p* state of free C_{60}. This is substantially the same as the He

case, discussed above, and occurs for the same reason: The Ne potential perturbs the C_{60} by only a small amount percentagewise, but the C_{60} potential exerts a significant perturbation on the Ne atom, thereby resulting in the hybridized levels being much closer to unperturbed C_{60} than unperturbed Ne.

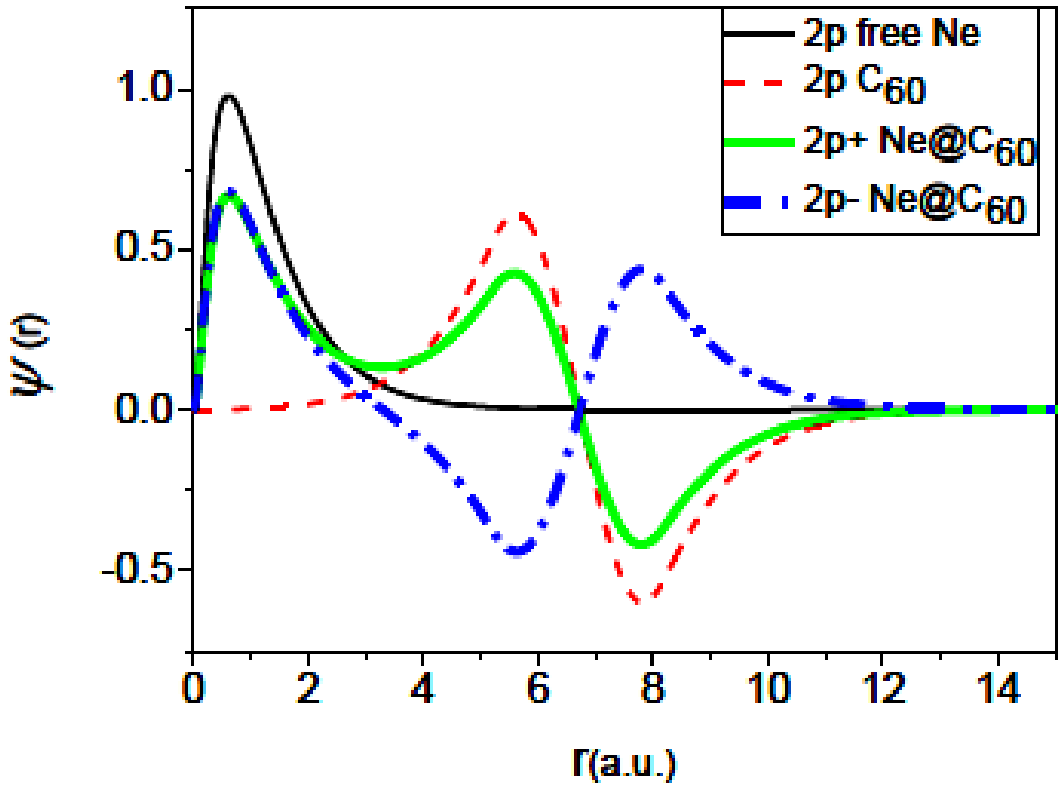

Figure4.4 Wave functions of 2s of free Ne, 2s of C_{60} and hybridized states of Ne@C_{60}

The cross sections for the free Ne and C_{60} 2p states, the states that mix to form the hybrids, are shown in Figure 4.5, along with the hybridized state cross sections. The free Ne 2p cross section is seen to be relatively flat and featureless, except for the autoionizing resonances leading up to the 2s ionization threshold; these are $2s \rightarrow kp$resonances. The non-resonant cross section is seen to be a bit below 10 Mb over the entire range shown. The free C_{60} 2p, on the other hand shows a cross section which maximizes at close to 100 Mb in the 20 eV (plasmon) region; and shows another maximum in the 35 eV region, the region of the second C_{60} plasmon, which is somewhat obscured by a Cooper minimum just at 40 eV. The $2s \rightarrow kp$ resonances are also seen in both the $2p^+$ and $2p^-$ cross sections occur at higher photon energy than is the case in free Ne. This occurs because the Ne 2s threshold energy in Ne@C_{60} increases by about 2.5 eV, as

compared to free Ne; thus, the resonances are about 2.5 eV higher. Note that these resonances occur at exactly the same energies in the $2p^+$ and $2p^-$ cross sections, as they must; the resonance energies are a property of the resonances themselves, not the channels that they decay to. However, it is clear that the manifestation of these resonances in rather different in the $2p^+$ and $2p^-$ cross sections, as seen in Figure 4.5. In any case, in the threshold (plasmon) region, it is seen from Figure 4.5 that both the $2p^+$ and $2p^-$ cross sections are larger than the free C_{60} $2p$ cross section, similar to what was found for the $He@C_{60}$ case. And as in the He case, the reason for this is the interchannel coupling of these channels with the photoionization channels of C_{60} that contribute to the plasmons.

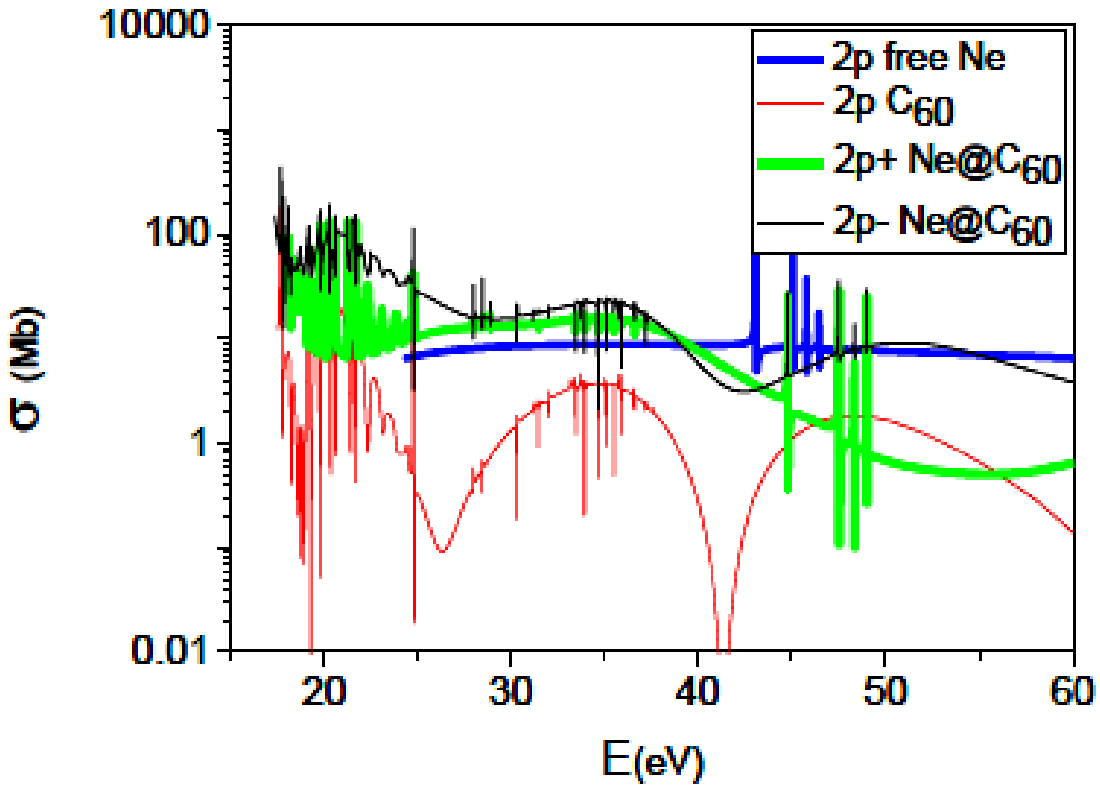

Figure4.5 Cross sections of 2p of free Ne, 2s of C_{60} and hybridized states of $Ne@C_{60}$

At the higher energies, the cross section is dominated by the atomic $2p$-like behavior since the C_{60} shell cross sections are much smaller here, as seen in Figure 4.6. In addition, the confinement oscillations in both $2p^+$ and $2p^-$ cross sections are quite evident. These behaviors are quite the same as was seen in the $He@C_{60}$ case, and for the same reasons. The fact that the C_{60} shell cross sections for the $2p$ (and other)

channels are so small in the higher photon energy region is a result of the delocalization of the valence orbitals. With increasing energy, the matrix element is generated closer and closer to the nucleus, and delocalized orbitals by their very nature, have small amplitude near the nucleus. Actually, the model potential used herein over-emphasizes this effect somewhat by "smearing out" the effect(s) of the 60 carbon nuclei of the C_{60}. However, even using a more realistic model, these delocalized orbitals would not have much amplitude in the vicinity of the carbon nuclei, so the argument remains valid; at the higher energies the cross sections of the delocalized C_{60} states will be much smaller than the cross sections of the atomic orbitals, hybridized or not.

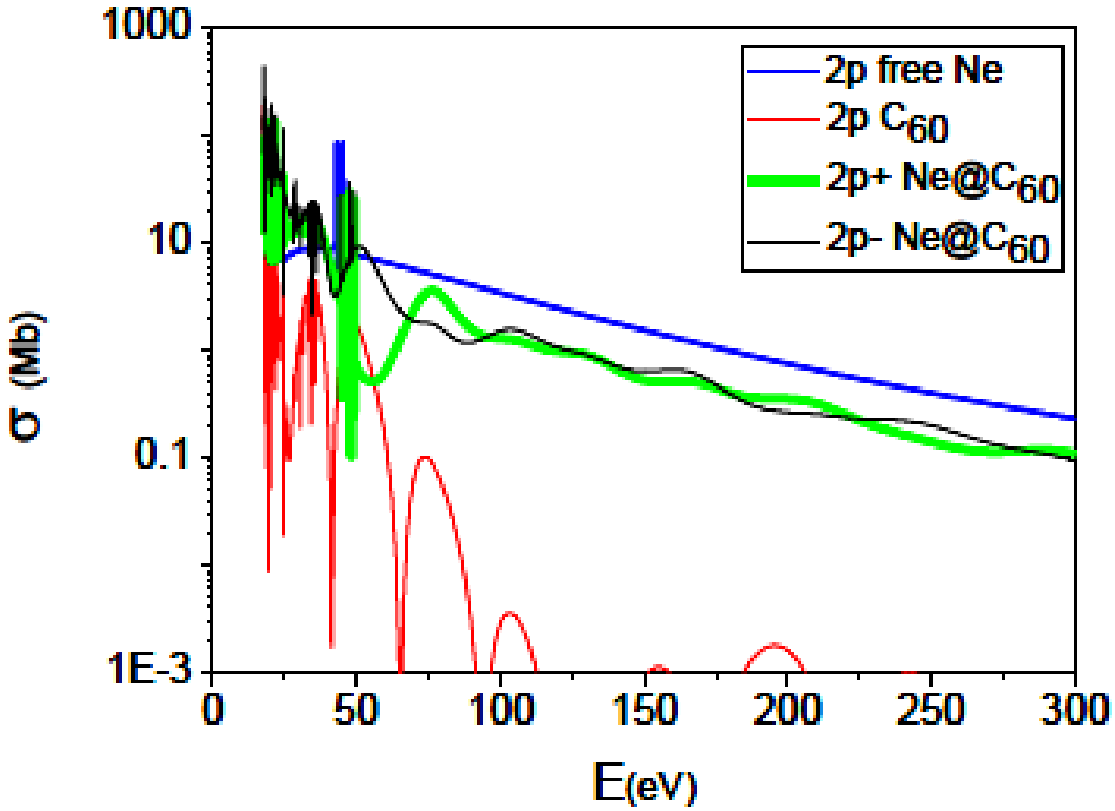

Figure4.6 Cross sections of 2p of free Ne, 2p of C_{60} and hybridized states of Ne@C_{60} at higher energies

The 2*s* wave function of Ne is not hybridized in Ne@C_{60}, as discussed above. Furthermore, its ionization threshold is well above the plasmon region, so the C_{60} cross section is small which means that one wouldn't expect much in the way of interchannel coupling. In other words, the 2*s* photoionization cross

section of confined Ne should be pretty much like the cross section for free Ne, except for the confinement oscillations brought about by the geometry of the confinement. This is exactly what happens, as seen in Figure 4.7. These results are quite similar to what is predicted using a simple static model of the C_{60} potential on the trapped atom where interchannel coupling with C_{60} shell photoionization channels is omitted [57].

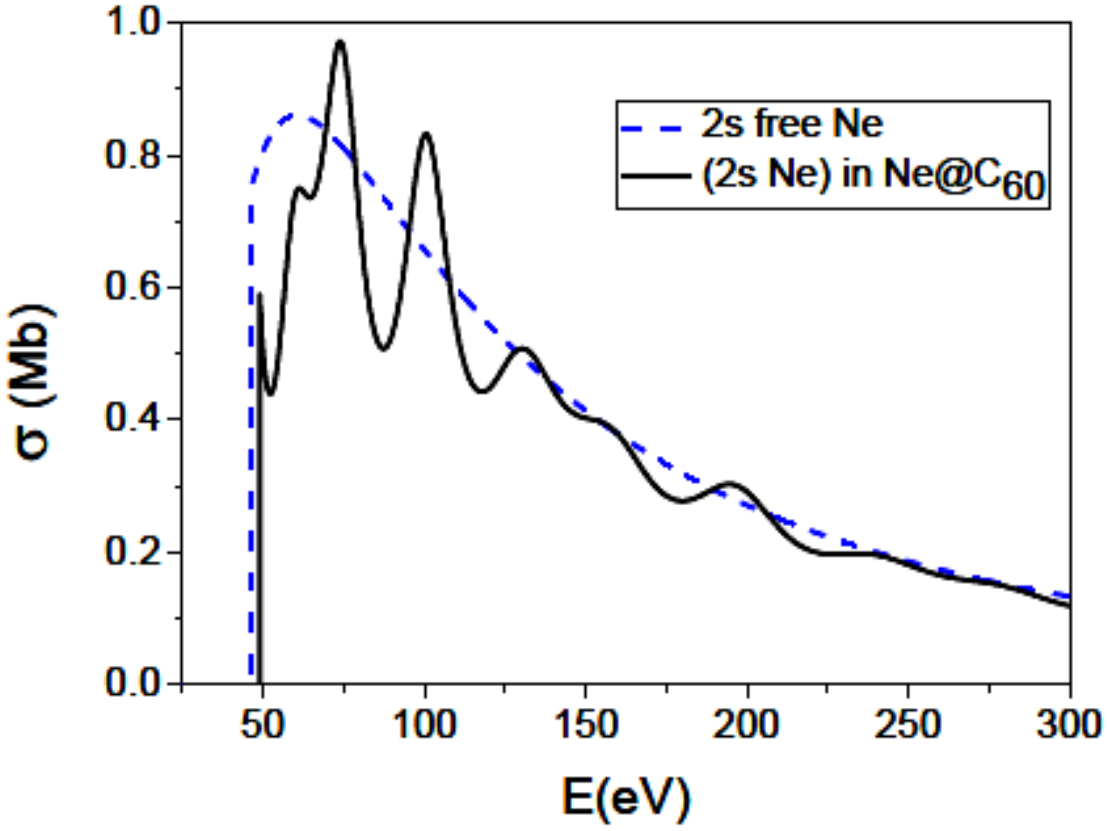

Figure4 0.7 Cross sections of 2s of free Ne, 2s of Ne inside Ne@C_{60}

The confinement resonances are seen to decrease in amplitude with increasing energy, just as the simple model predicts [54,55,56]. This agreement with the simple model further suggested by the 1s cross section of the trapped Ne atom, shown in Figure 4.8. Here again, an atomic-like cross section is seen, modulated by confinement resonances. It must be pointed out, however, that, since the 1*s* photoionization of the carbon atoms of the shell are omitted from the present calculation, any interchannel coupling of the Ne 1*s* cross section with the C 1*s* from the shell is, of course, omitted. But, interchannel coupling is only im-

portant when a channel with a small cross section is degenerate with a large one [57]. In this case, since the Ne 1*s* threshold is well above the C 1*s* threshold, the total cross section for the1*s* of all 60 carbon atoms of the shell, which can be estimated from the cross section for free carbon [58,59], is only slightly larger than the Ne 1*s* cross section. Thus, the omission is not likely to have a significant effect on the 1*s* photoionization of trapped Ne. In any case, scrutiny of the 1*s* and 2*s* photoionization of encaged Ne gives a good indication of where the simple model might be useful.

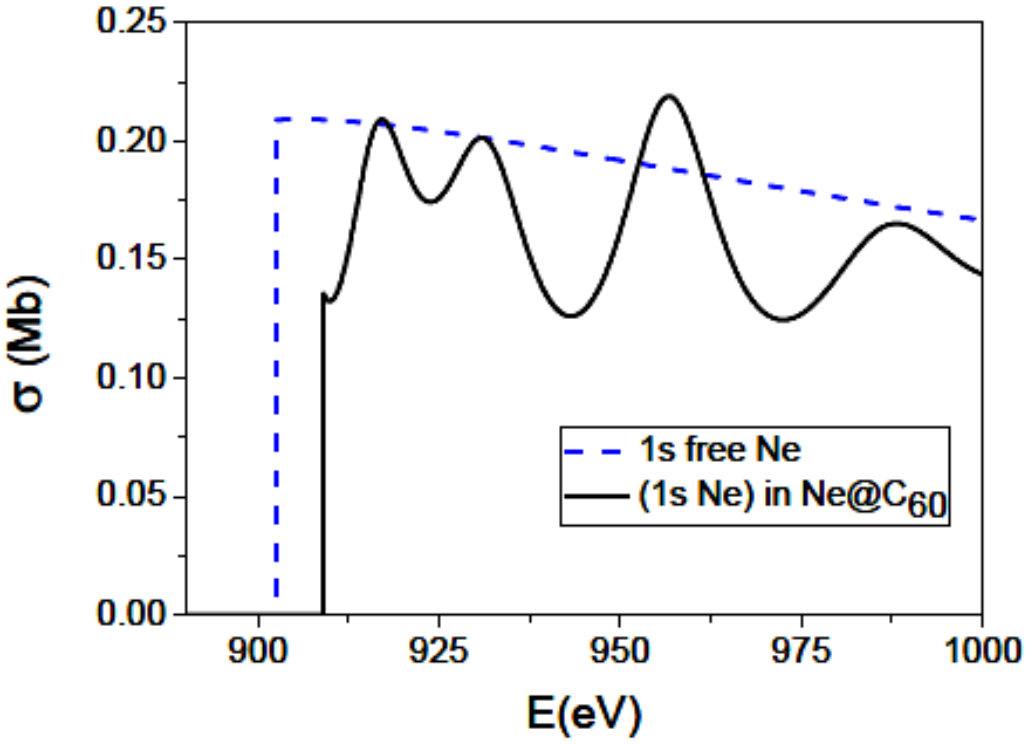

Figure4.8 Cross sections of 1s of free Ne, 1s of Ne inside Ne@C_{60}

4.3.3. Ar@C_{60}

A previous calculation of 3*p* photoionization of Ar@C_{60} has been reported [47] using the same methodology as used herein, but completeness dictates that some of that presentation should be repeated. The situation for caged argon, Ar@C_{60}, is somewhat different than the previous cases in that no significant hybridization results in this case [47]. Of the Ar wave functions, only the 3*p* orbital shows any hybridization at all, as shown in Figure 4.9. Due to the entrapment, the C_{60} 2*p* orbital acquires a small "image" of the atomic 3*p* wave at small distances, and the Ar 3*p* wave function exhibits a bit of the C_{60} 2*p* wave function at in-

termediate distance from the center of the molecule. In other words, although they are slightly perturbed, the Ar 3*p* and C_{60} 2*p* wave functions retain their essential characters in the Ar@C_{60} molecule.

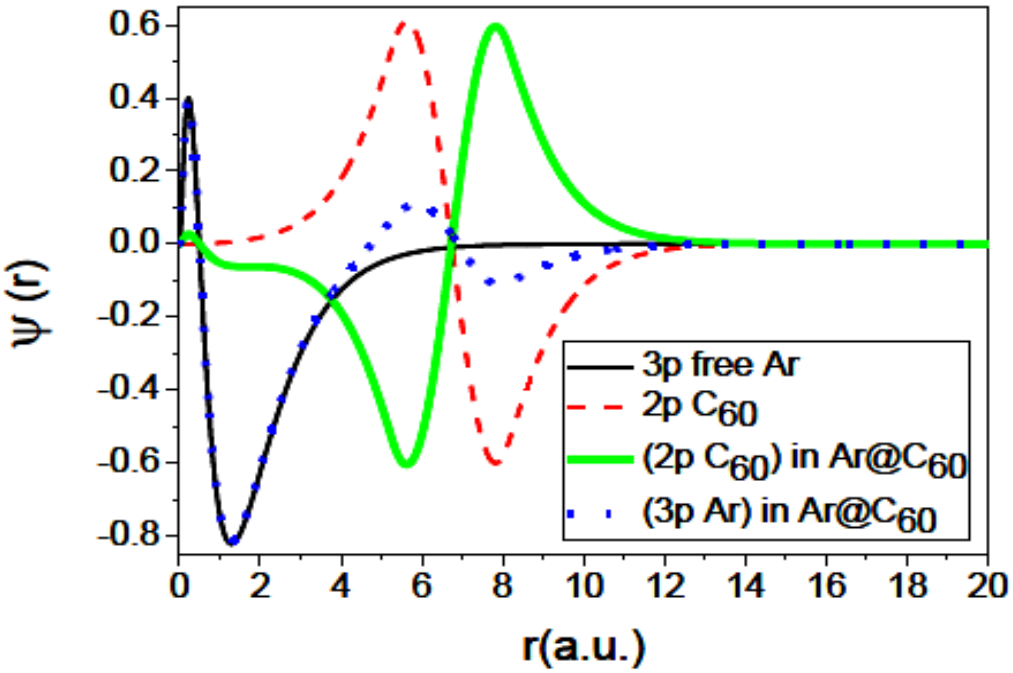

Figure4.9 Wave functions of 3p of free Ar, 2p of C_{60} and atomic and shell states inside Ar@C_{60}

The 3*p* photoionization cross sections for free and confined Ar are shown in Figure 4.10 where a remarkable difference between the two is noted; the confined 3*p* cross section is almost two orders of magnitude larger that its counterpart in free Ar. With increasing energy, this difference gets smaller, but remains until about 40 eV, or just above the higher-energy plasmon in C_{60}. To emphasize how large this difference really is, the integrated oscillator strength for the 3*p* of free Ar from threshold to 40 eV is found to be about 4.85, or most of the six electrons in the 3*p* subshell. By way of comparison, the integrated oscillator for 3p of the confined atom is 60.2! This is greater than the total number of electrons in the Ar atom, not merely the six of the 3p subshell. Thus, since there is no appreciable hybridization of the 3*p* discrete wave function, this phenomenon must be due to correlation in the final (continuum) state of the photoionization process, interchannel coupling with the C_{60} photoionization channels. Furthermore, since the shell contains 240 non-localized electrons, it is evident that an appreciable fraction of the strength is transferred

to the Ar 3*p* channel *via* interchannel coupling. Mathematically, this can be represented using the Fano continuum configuration interaction formalism [60]. Defining the unperturbed (free) Ar 3*p* dipole matrix element as $\mathcal{D}_{3p}(E)$, and the perturbed matrix element (perturbed by interchannel coupling) as $M_{3p}(E)$, then the perturbed matrix element, at energy *E*, is given by

$$\mathcal{M}_{3p}(E) = \mathcal{D}_{3p}(E) + \sum_{nl} \int dE' \frac{\left\langle \psi_{nl}(E') \middle| \frac{1}{r_{3p,nl}} \middle| \psi_{3p}(E) \right\rangle}{E - E'} \mathcal{D}_{nl}(E') \,, \qquad \textbf{(4.4)}$$

where ψ_{3p} and ψ_{nl} are the unperturbed final continuum state wave functions for 3*p* photoionization of free Ar and *nl* photoionization of the C_{60} shell, $r_{3p,nl} = |r_{3p} - r_{nl}|$, and the sum is over all of the delocalized electrons of the C_{60} shell. In the threshold region, where the perturbed 3*p* cross section is so much larger than the unperturbed, the second term in (4.4), the interchannel coupling term, dominates owing to the strength of the matrix elements of the delocalized electrons, $\mathcal{D}_{nl}$, which collectively form the huge plasmon in this energy region. With increasing energy, the interchannel coupling contributions become smaller, as the $\mathcal{D}_{nl}$ decrease with energy and the energy denominator in (4.4) reduces the contributions from the low-energy plasmon region, and by 40 eV, interchannel coupling is relatively unimportant.

Looking at the higher energy region, shown in Figure4.10, the Cooper minimum [61] in the free 3*p* cross section is seen in the 40 eV region, and this Cooper minimum is reproduced in the confined cross section just a few eV higher. Above the Cooper minimum region, the free and confined cross sections are quite similar, except for the confinement oscillations exhibited by the confined cross section. Since the Cooper minimum is so sensitive to any kind of interaction with the system or correlation effect [62], it is clear that the effect(s) of the cage on the 3p cross section is quite small, from the energy of the Cooper minimum region and above; this indicates further that the simple static model should be adequate in this energy region. Also evident in both the free and confined 3*p* cross sections are the 3*s*→*kp* resonances which appear as window resonances in both cases; these window resonances are known experimentally for the free Ar atom. However, it is also seen that these resonances show up at lower photon energy in the confined case,

reflected the fact that the Ar 3*s* subshell is less bound in the confined case. It is also seen that the confinement affects not only the position of these resonances, but their detailed shape and width as well, thereby indicating that the interaction with the confining shell affects, not only the binding energies of the confined atom, but the dynamics of transition processes as well.

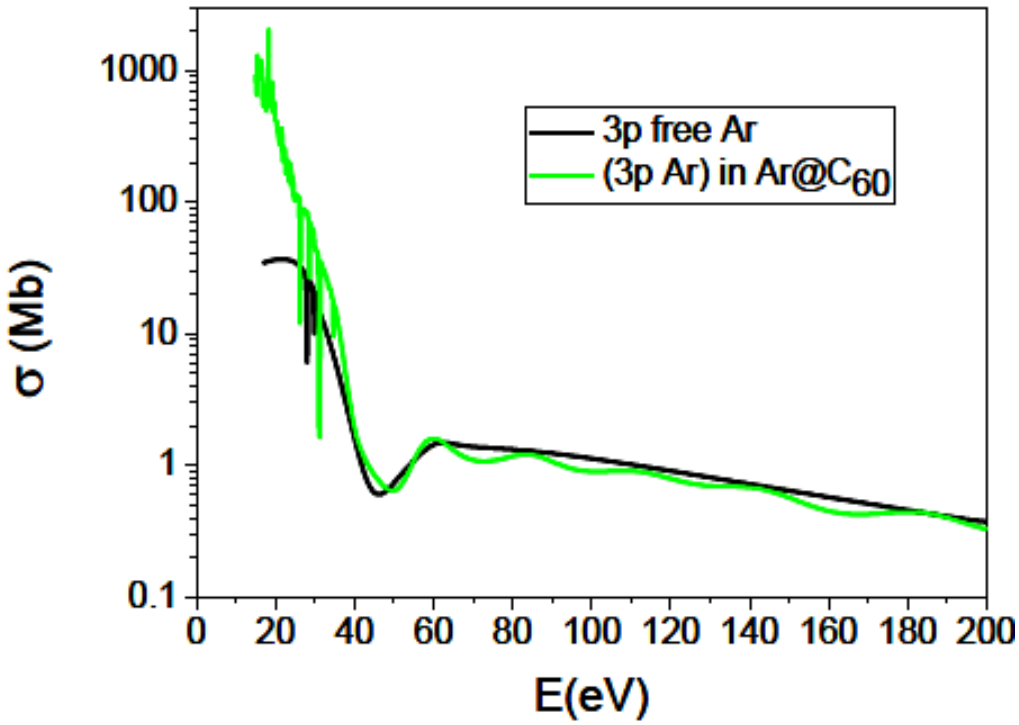

Figure4.10 Cross sections of 3p of free Ar and 3p Ar inside Ar@C_{60}

The calculated photoionization cross section of the 3s subshell of free and confined Ar is presented in Figure4.11. For free Ar, the dominant feature in the cross section is a very deep Cooper minimum at about 40 eV. It is known that this feature results from interchannel coupling within the free Ar atom [63]; the result also agrees reasonably well with experiment [64]. In the confined case, at the lower energies, near the 3*s* ionization threshold, the 3*s* cross section is enhanced considerably, by a factor of five or so, owing to interchannel coupling with the photoionization channels of the C_{60} shell. This is similar to what happens for 3*p*, as discussed above, but the effect is much smaller since the shell cross sections drop very rapidly above the first plasmon at about 20 eV. Furthermore, the confinement oscillations are clearly seen in the confined

Ar 3*s* cross section above about 30 eV and, as expected, their amplitudes diminish with increasing energy. The details of the Cooper minimum are altered somewhat from the free case owing to a combination of the dynamical effects of interchannel coupling, along with the confinement oscillations.

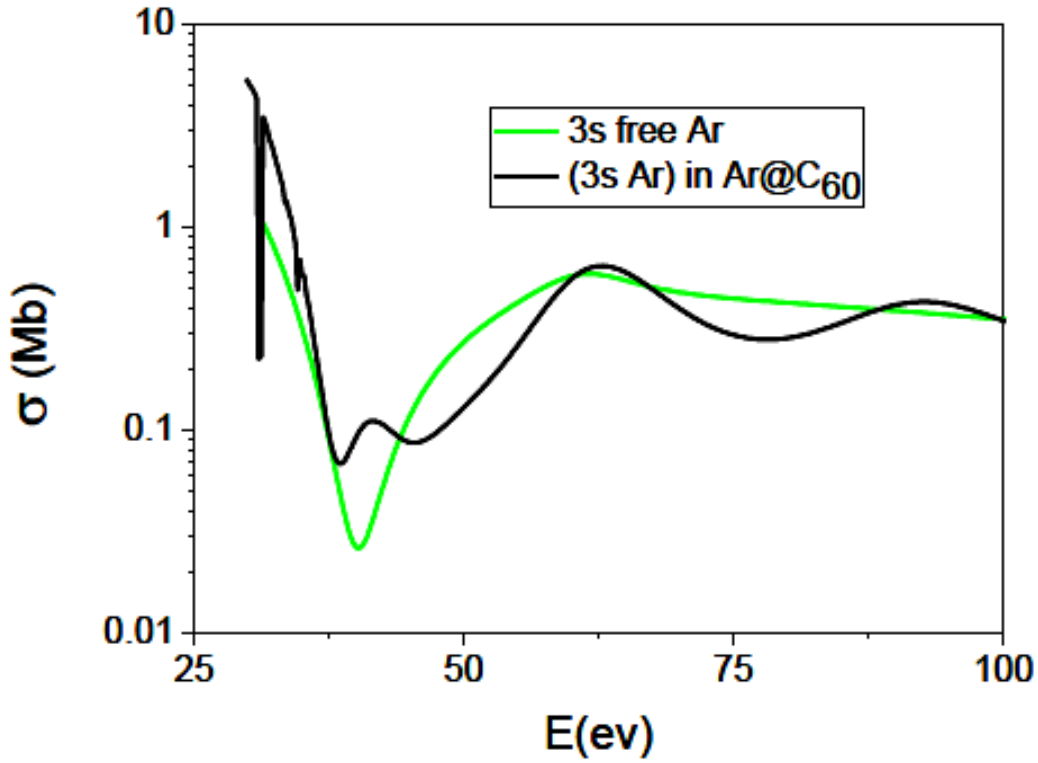

Figure4.11 Cross sections of 3s of free Ar and (3p Ar) inside Ar@C_{60}

4.3.4. Kr@C_{60}

The situation for Kr is rather similar to that for Ar. The 4*p* wave function of Kr and the 2*p* orbital of C_{60} are *very slightly* hybridized, as shown in Figure 4.12; this is almost exactly like the situation for Ar. In addition, also like Ar, the outer n*s*, the 4*s* in this case, is not hybridized at all. The calculated free and confined Kr 4*p* cross sections are shown in Figure 4.13 in the lower energy region where it is seen that interchannel coupling in the confined case increases the cross section by almost two orders of magnitude in the threshold region; as in the Ar case, this occurs because the photoionization cross section (matrix element) for the C_{60} channels in the plasmon region, just below 20 eV, is so much larger than the atomic cross section. At the end of the plasmon region, about 40 eV, this inequality no longer exists and the free and confined cross section more or less come together, except for the confinement resonances for the trapped atom. The win-

dow resonances, $4s \rightarrow kp$, just below the opening of the 4s channel are also seen in the free cross section, and at lower energies in the confined cross section reflecting the decrease in binding energy engendered by the confinement.

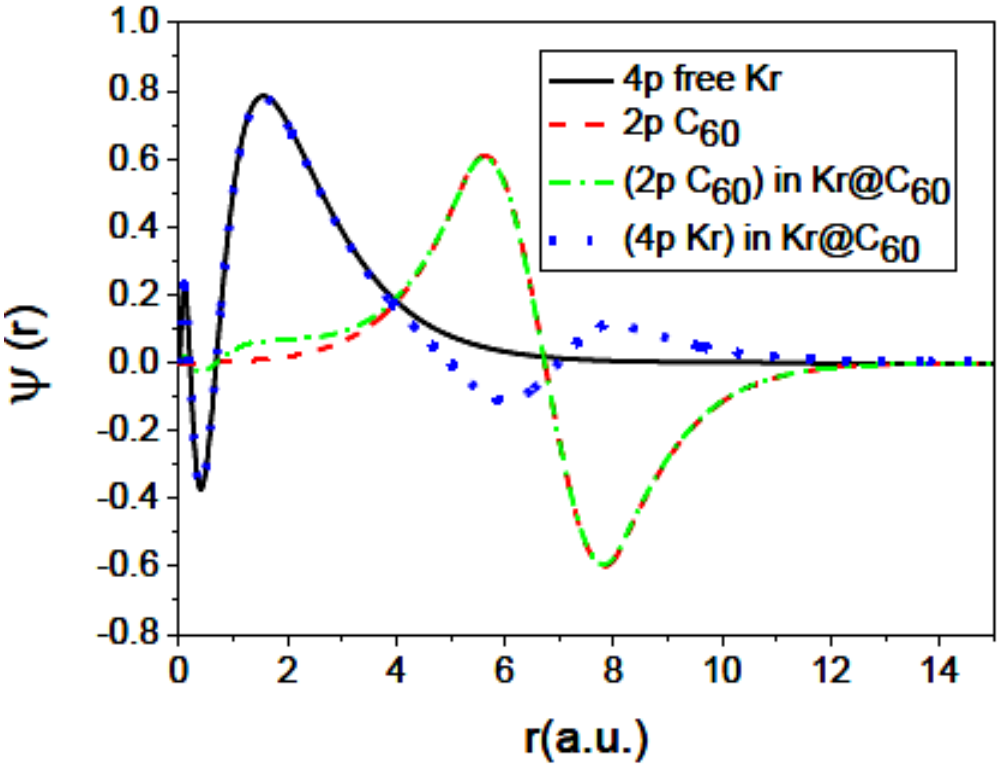

Figure4.12 Wave functions of 4p of free Kr, 2p of C_{60} and atomic and shell states inside Kr@C_{60}

At higher energies, shown in Figure 4.14, a broad Cooper minimum is seen in both free and confined cross sections along with strong resonances in the 100 eV region, just below the 3d threshold, in both cases. Then a second maximum in the cross sections are seen as they recover from the Cooper minima. Thus, above about 40 eV, except for confinement resonances and shifts in energy due to the cage potential, the free and confined results are almost the same; this means that in the energy region from 40 eV, the simple static model should be a reasonable approximation, in this case.

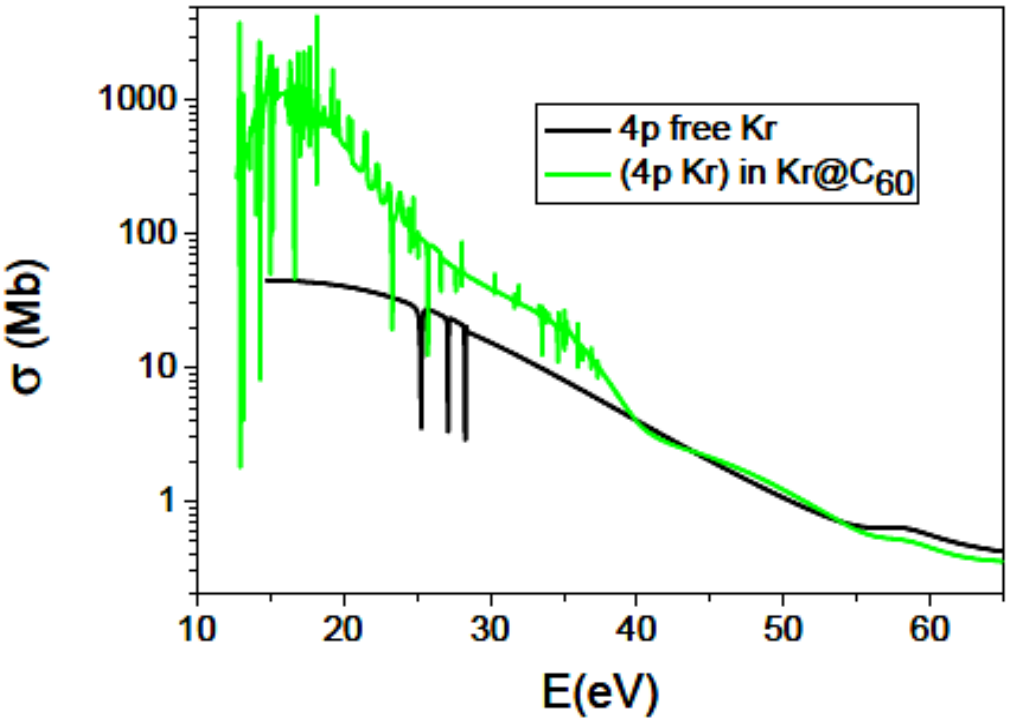

Figure4.13 Cross sections of 4p of free Kr and 4p Kr inside Kr@C_{60}

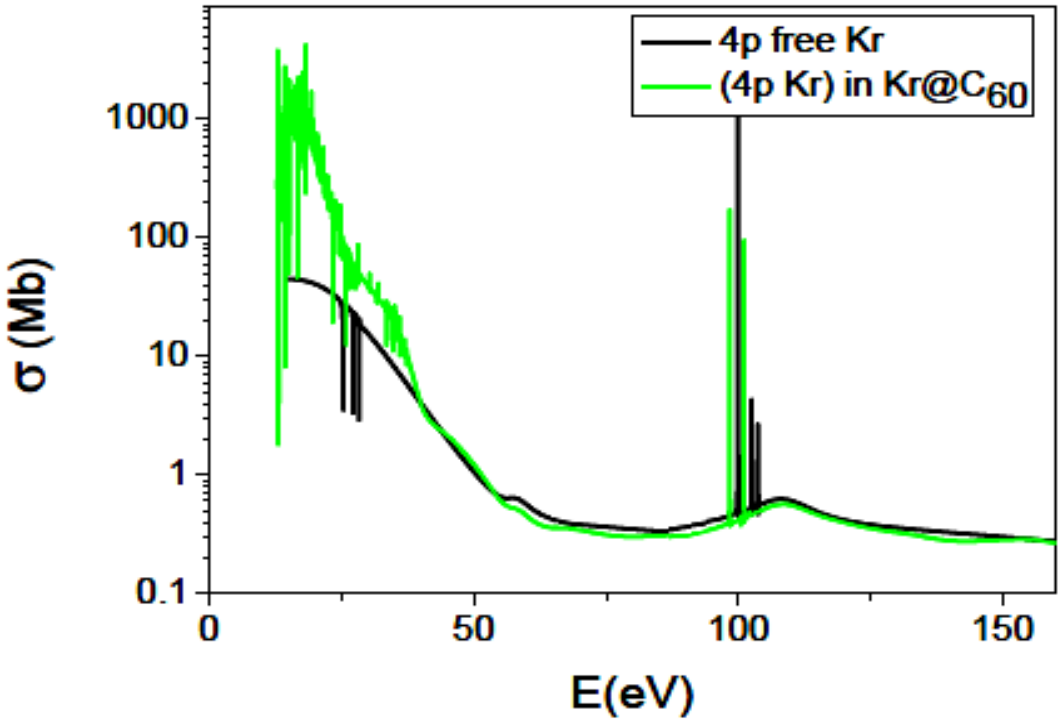

Figure4.14 sections of 4p of free Kr and 4p Kr inside Kr@C_{60} at higher energies

The 4*s* cross sections are shown in Figure 4.15, and they behave rather like the 3*s* of Ar. In the threshold region, about 25 eV, the confined cross section is enhanced *via* interchannel coupling by a factor of about four. And this enhancement decreases with increasing energy as we move to the edge of the plasmon region at about 35 eV. Both free and confined cross sections are seen to exhibit Cooper minima; again the primary cause of these Cooper minima is interchannel coupling among the atomic photoionization channels, but the Cooper minimum in the confined case is perturbed by the confinement potential along with the attendant confinement oscillations.

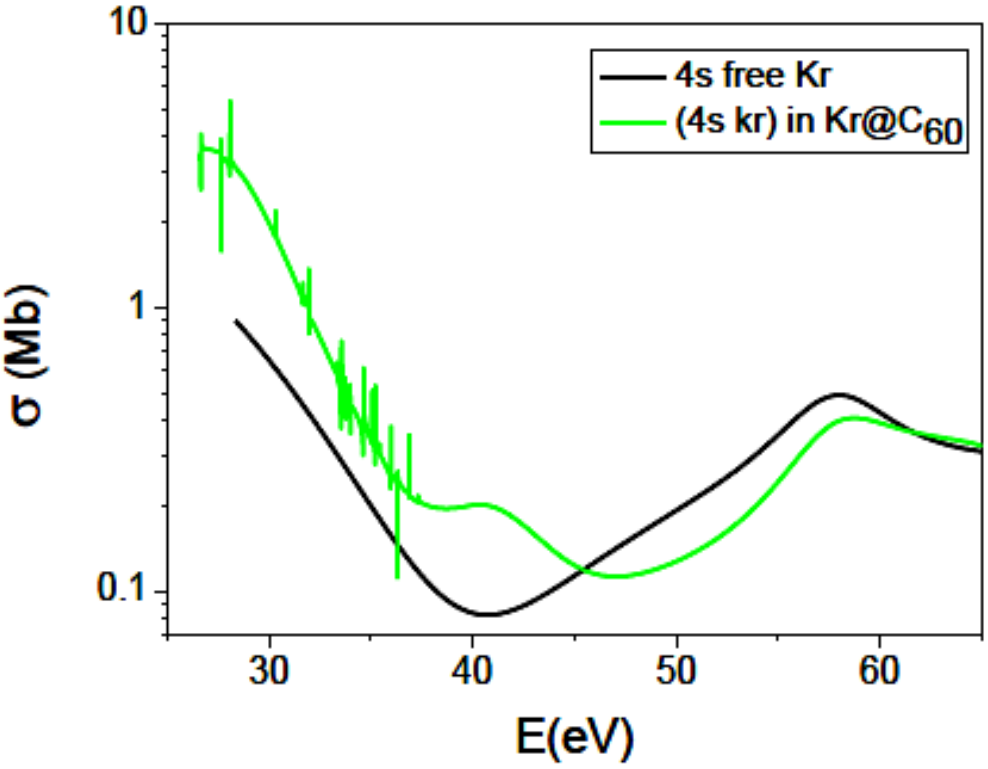

Figure4.15 Cross sections of 4s of free Kr and 4p Kr inside Kr@C_{60}

A similar situation is exhibited for Kr 3*d* photoionization as seen in Figure 4.16. Owing to the $d \rightarrow f$ shape resonance [65], the cross section for free Kr is rising from threshold. And, since the threshold energy, over 100 eV, is so far above the plasmon region of C_{60}, interchannel coupling is of essentially no consequence. Thus, the cross section for the confined case is essentially just the free cross section modulated by

confinement oscillation, clearly seen in Figure 4.16. Evidently the high initial-state angular momentum (this is the first *d*-state encountered) engenders no new behavior related to confinement.

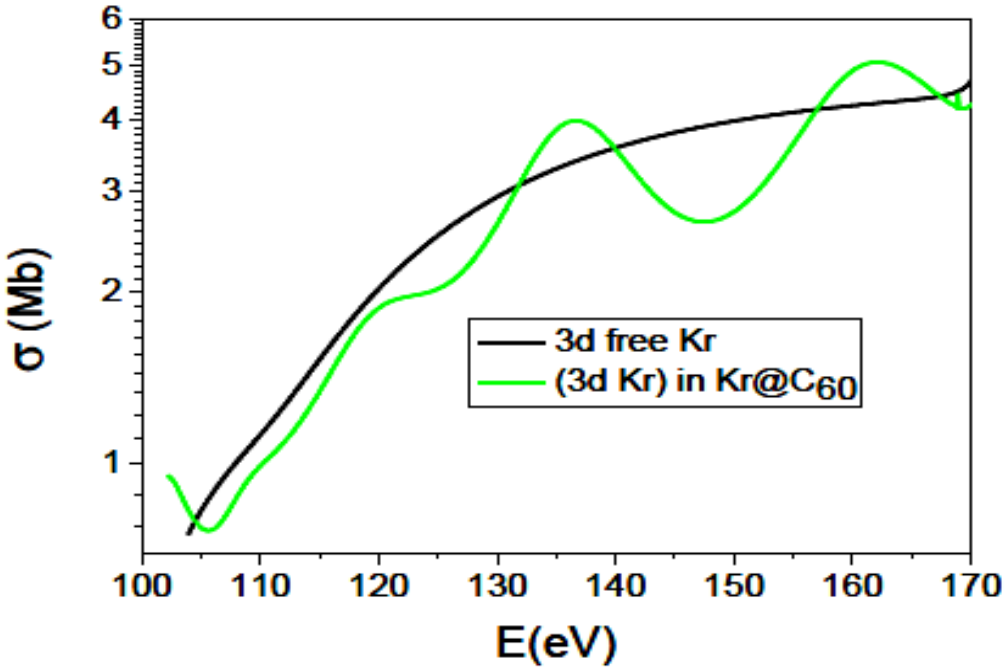

Figure4.16 Cross sections of 3d of free Kr and 3d Kr inside Kr@C_{60}

4.3.5. Xe@C_{60}

Some aspects of the photoionization of confined Xe have been reported on previously [46] but some repetition is necessary herein to fully depict the evolution along the sequence of noble gas atoms. Similar to Ar and Kr, the outer *p*-subshell, 5*p* in this case, is only slightly hybridized, as seen in Figure 4.17.

Unlike the previous two cases, however, the outermost s-subshell, 5s, displays significant hybridization, as shown in Figure 4.18. The hybridization is with the 2*s* of C_{60}, just as was the case with confined He, discussed above. The mixing is seen to be roughly 50-50. The theoretical binding energy of Xe 5*s* is calculated to be 0.839 au, which is reasonably close to 2*s* binding energy in free C_{60} of 0.645 au (Table 4.1). The binding energies of the hybridized orbitals, $5s^{+}$ and $5s^{-}$, are 0.733 au and 0.665 au; the latter is close to the free C_{60} 2*s* binding energy, but the former is roughly half way between the two. This is different than the previous cases of hybridization where the hybridized orbitals were found to have binding energies quite

close to the free C_{60} component. This is because in this case, the atomic potential, which supports 54 electrons, is not so very small compared to the shell potential.

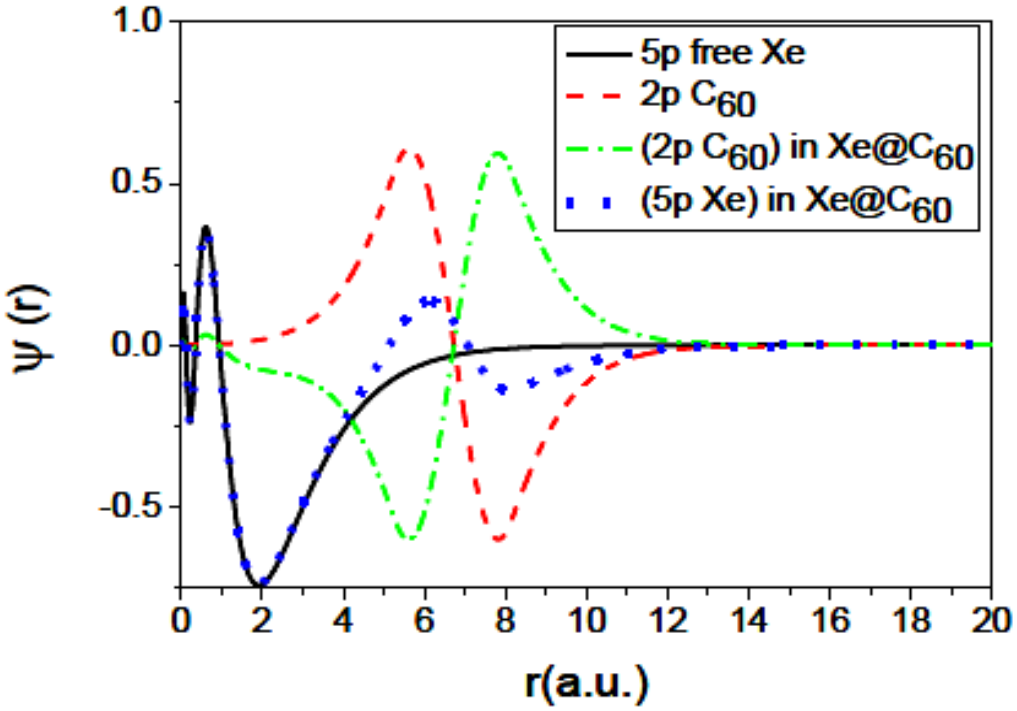

Figure4.17 Wave functions of 5p of free Xe, 2p of C_{60} and atomic and shell states inside Xe@C_{60}

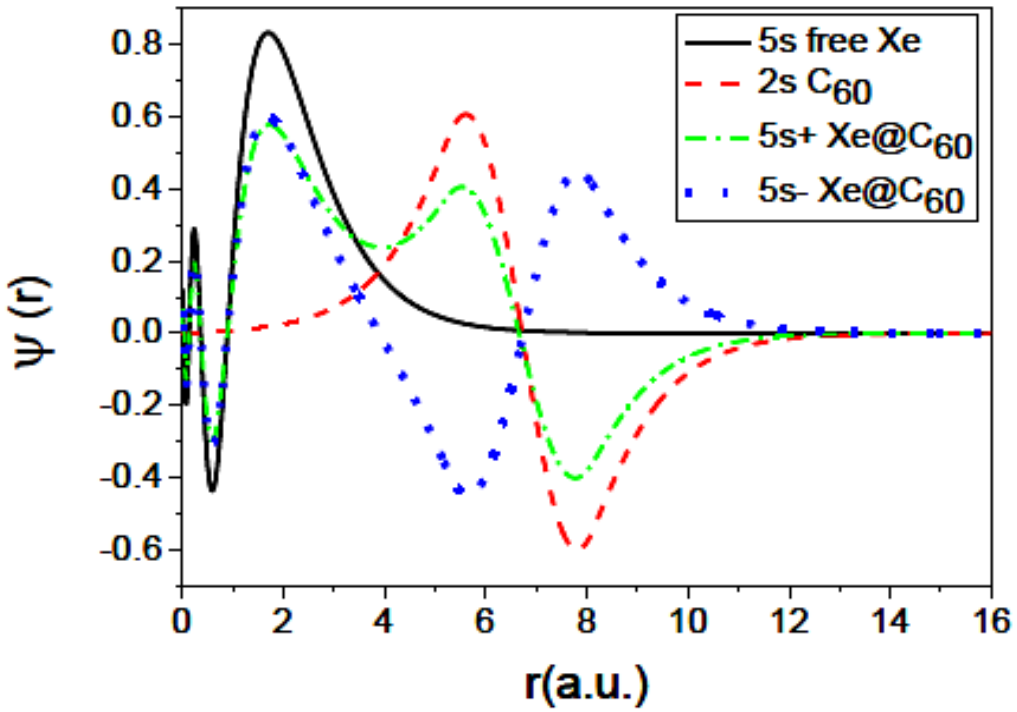

Figure4.18 Wave functions of 5s of free Xe, 2s of C_{60} and hybridized states of Xe@C_{60}

The calculated free and confined 5*p* cross sections are displayed in Figure 4.19, and a picture similar to the corresponding outer n*p* subshell in Ar and Kr is seen. As in those cases, the confined cross section is almost two orders of magnitude larger than the atomic cross section owing to interchannel coupling with the huge C_{60} plasmon excitations; The confined 5*p* cross section displays the effects of coupling with both of the plasmons, the larger one at the lower energies and the smaller one at the higher energies. Above the energy region of the plasmons, the confined cross section is similar to the free 5*p* cross section, except for the confinement oscillations. The window resonances, $5s \rightarrow kp$, seen in the atomic cross section below the opening of the 5s channel, are difficult to pick out in the confined cross section since they occur in a region of many resonances involving transitions to hole states in the C_{60} shell. There must actually be two sets of resonances, a $4s^{+} \rightarrow kp$ series and a $4s^{-} \rightarrow kp$ series, but they do not appear to show up as window resonances in the confined case. This differs from the Ar and Kr cases, evidently because of the hybridization of the 5s orbital in confined Xe. This is an effect of hybridization that has not been known previously.

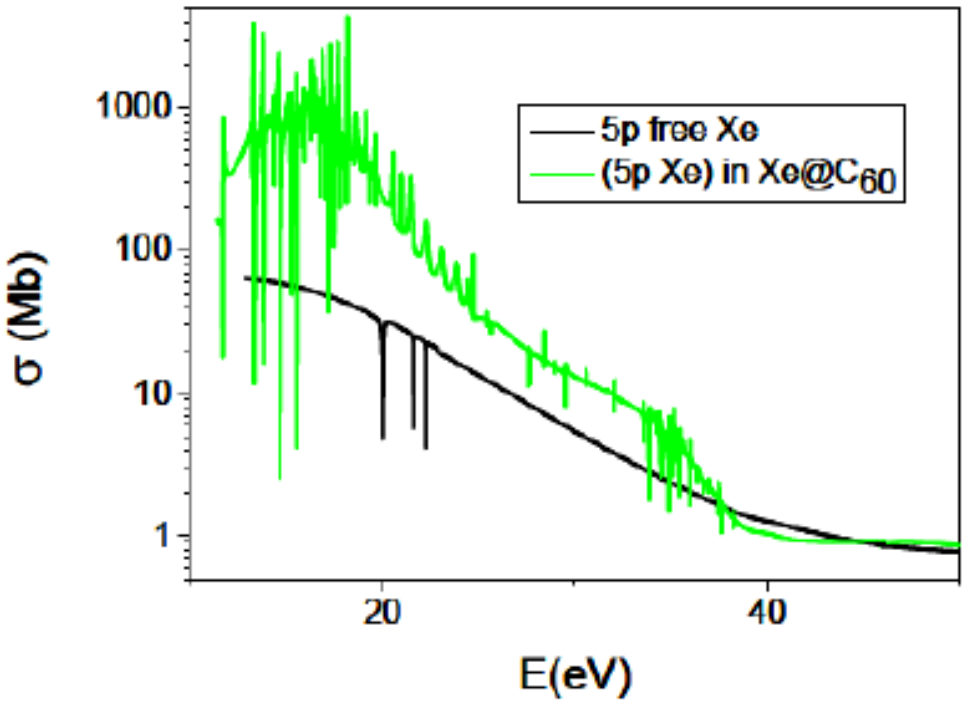

Figure4.19 Cross sections of 5p of free Xe and 5p Xe inside Xe@C_{60}

The cross sections for the hybridized $5s^+$ and $5s^-$ states of the combined $Xe@C_{60}$ system are shown in Figure 4.20, along with the cross sections of 5*s* of free Xe and 2*s* of free C_{60}. It is striking that both the $5s^+$ and $5s^-$ cross section are approximately an order of magnitude larger than the cross sections of the free Xe and free C_{60} constituents of these hybridized states. Clearly then, interchannel coupling in the final continuum states also plays a crucial role in the determination of these cross sections. In fact, evidence of the influence of the C_{60} plasmons is seen in the maxima in the 20 eV region and the maxima a bit below 40 eV. In any case, this is another instance of both the initial state and the final state of a photoionizing transition losing their identity in the combined system.

The 4*d* cross sections for the free and confined systems are presented in Figure 4.21. Since the 4*d* threshold energies are well above the plasmon region, no important interchannel coupling effects of the 4*d* cross section with the shell channels are expected, and none are seen. However, significant confinement oscillations are evident. Note that confinement oscillations in the 4*d* subshell of $Xe@C_{60}$ have been observed experimentally [10,11] and show prominent peaks at photon energies of about 90 eV and 110 eV, as compared to the present results which show the peaks at roughly 100 eV and 120 eV. This discrepancy indicates that, although the present calculations are qualitatively correct, there are some quantitative deficiencies. The major contribution to the difference is probably due to the error in the 4*d* binding energy which is too large for free Xe by about 7.5 eV, 75 eV vs. 67.5 eV [64]. Assuming that the same difference persists for the confined atom, this accounts for 75% of the difference; in other words, the peaks are only off by about 2.5 eV as a function of photoelectron energy. The remaining discrepancy is probably due to the use of a jellium spherical square well to approximate the field of the 60 C^{4+} ions of the C_{60} shell. In any case, the notion that confinement oscillations might be mythical, as suggested recently [66], is certainly not borne out. In addition to the smooth nonresonant cross section, Rydberg resonances are seen in the 150 eV and the 190 eV regions of the cross sections. These are the resonances leading up the 4*p* and 4*s* thresh-

olds, respectively. The resonances are displaced slightly between the free and confined cross sections owing to the slight differences in threshold energies engendered by the confinement.

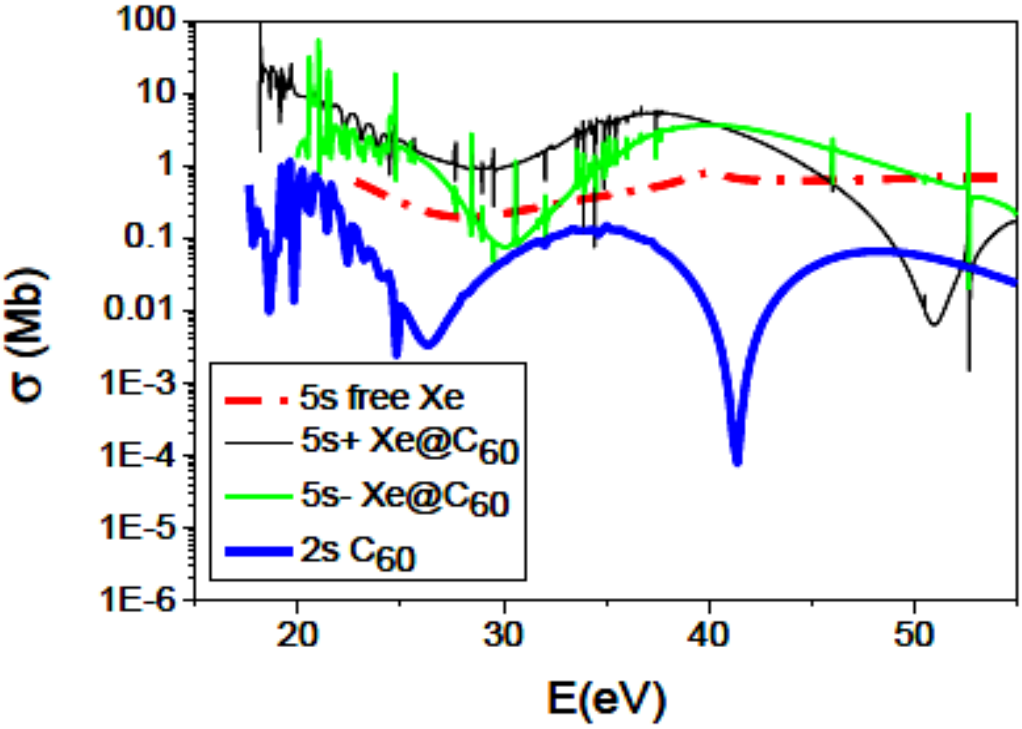

Figure4.20 Cross sections of 5s of free Xe, 2s of C_{60} and hybridized states

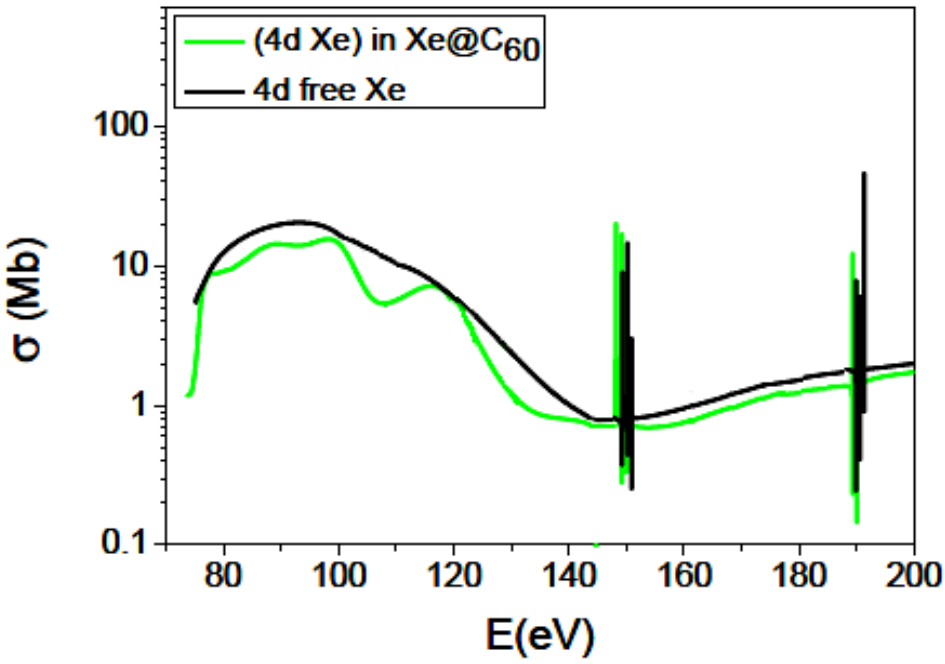

Figure 4.21 Cross sections of 4d free Xe and 4d Xe inside Xe@C_{60}

Lastly, the free and confined 4p cross sections are shown in Figure 4.22. The 4p cross sections are small and the confined cross section similar to the free, except for the confinement oscillations. However, the confined cross section is everywhere about 10% below the free cross section indicating that the confinement induces more than simply a modulation about the free cross section. Most likely, the small overall decrease in cross section arises from small differences in interchannel coupling among the atomic photoionization channels. The Rydberg resonances below the opening of the 4*s* channel are seen in this case, just as in the 4*d* cross section.

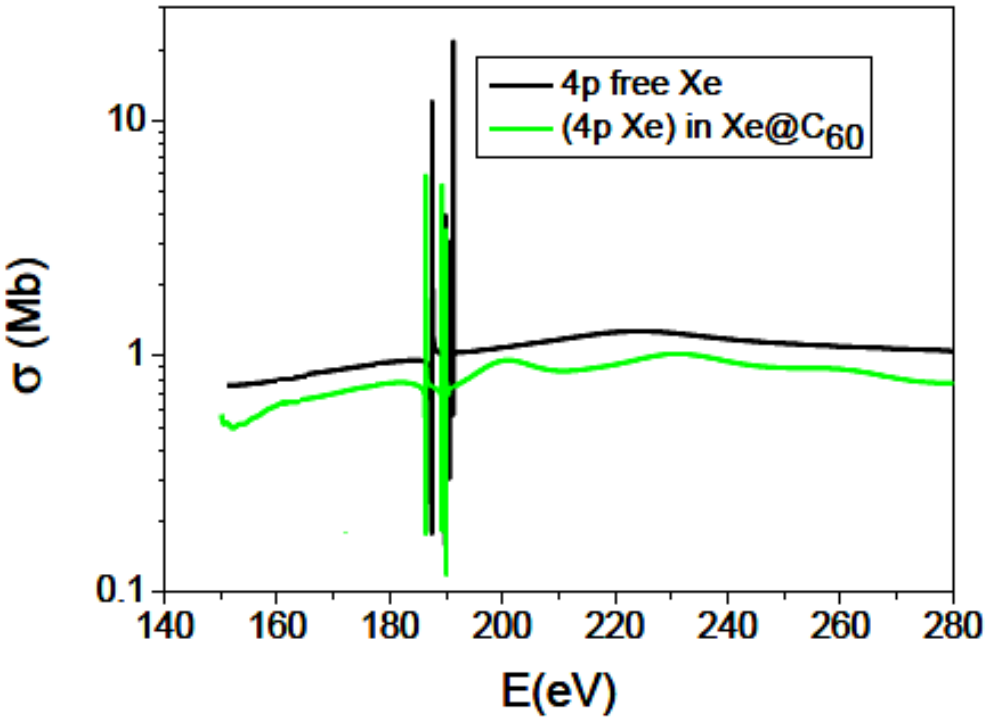

Figure4.22 Cross sections of 4p free Xe and 4p Xe inside Xe@C_{60}

4.4. Valence photoionization of small alkaline earth atoms endohedrally confined in C_{60}

4.4.1. The ground state

Table 4.2 lists LDA single-electron configurations of Be@C_{60}, Mg@C_{60} and Ca@C_{60} using Coulomb notation, and identifies the nature of *s* and *p* orbitals. Several of these orbitals invoke additional radial

nodes in order to satisfy the Pauli Exclusion Principle. However, with only exceptions of the atomic valence orbitals, effects of these extra nodes on the shape of other orbitals are extremely weak, virtually retaining these orbitals rather pure. The radial component of the LDA potentials, calculated by the occupancy weighted averaging of all the orbitals of an endofullerene, are presented in Figure 4.23(a) for the three systems. As expected, the depth of the atomic cusp gradually increases as the size of the atom grows. But the potential in the C_{60} shell region remains unchanged. This is because, even though the orbital-specific potentials (not shown) corresponding to Pauli-modified atomic valence levels do alter over the shell region, the effect washes out in the averaging process, since these orbitals being *s*-type hold only two electrons.

Figure 4.23(b) shows the radial probability densities of the valence electrons which are 2*s*, 3*s* and 4*s*, respectively, for the three free atoms. We use the symbol $\eta s@$, with $\eta = 2,3,4$, to denote the levels of the confined atom, while technically these wavefunctions are 4*s*, 5*s* and 6*s* of the compound system due to the mixing induced by two additional nodes (Table 4.2). As seen in Figure 4.23(b), the relative strength of the mixing grows with the increase of the atomic size, consequences of which on the photoionization mechanism over the plasmon active energy region and beyond will be revealed in the following section. In Figure 4.23(a), the positions of the corresponding binding energies of captive atomic levels are included, the explicit values of which along with those for free atoms are noted in Table 4.3, that suggests the decrease of binding energies from the mixing. We also show in Figure 4.23(a) a few highlying π (single-noded) and σ (nodeless) C_{60} states in order to aid our later discussions.

Table 4. 2. Ground state configurations of the endofullerene compounds.

Be@C_{60}	**Mg@C_{60}**	**Ca@C60**
1*s* (Be 1*s*)	1*s* (Mg 1*s*)	1*s* (Ca 1*s*)
2*s* (C60 1*s* + a weak atomic node)	2*s* (Mg 2*s*)	2*s* (Ca 2*s*)
3*s* (C60 2*s* + a weak atomic node)	2*p* (Mg 2*p*)	2*p* (Ca 2*p*)
4*s* (Be 2*s* + two shell nodes) (2*s*@ Be)	3*s* (C60 1*s* + two weak atomic nodes)	3*s* (Ca 3*s*)
higher *l* states are C60 states	3*p* (C60 2*p* + one weak atomic node)	4*s* (C60 1*s* + three weak atomic nodes)
	4*s* (C60 2*s* + two weak atomic nodes)	3*p* (C60 2*p* + two weak atomic nodes)
	4*p* (C60 3*p* + one weak atomic node)	4*p* (Ca 3*p* + one weak shell node)

	5*s* (Mg 3*s* + two shell nodes) (3*s*@ Mg)	5*s* (C60 2*s* + three weak atomic nodes)
	higher *l* states are C60 states	5*p* (C60 3*p* + two weak atomic nodes)
		6*s* (Ca 4*s* + two shell nodes) (4*s*@ Ca)
		higher *l* states are C60 states

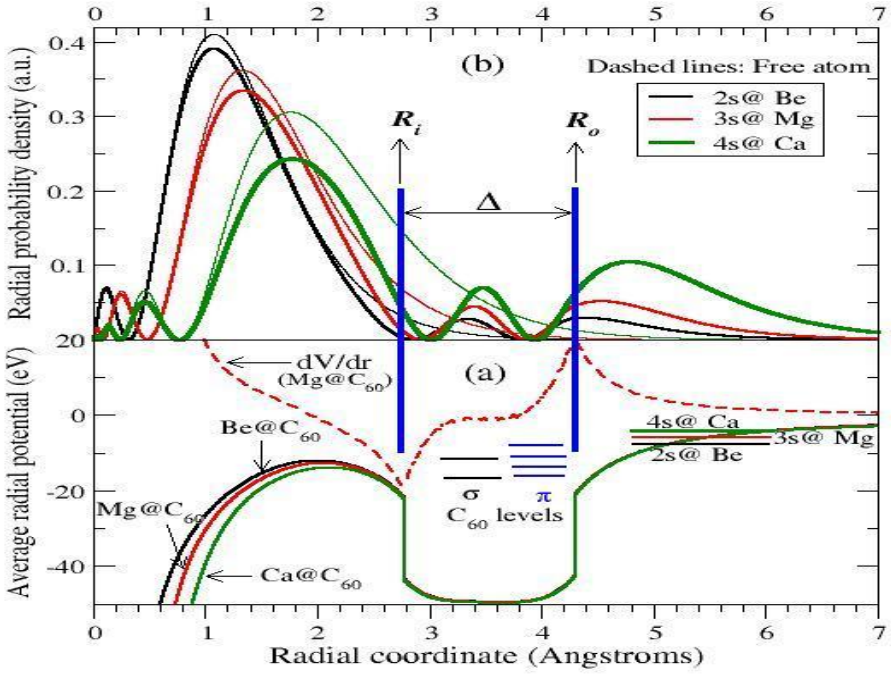

Figure4.23 (a) Average radial LDA potentials for systems: Be@C_{60}, Mg@C_{60}, and Ca@C_{60}. (b) Radial probability densities of free and confined atomic levels. The positions of inner and outer edges of the C_{60} hull are also indicated

The radial derivative of the potential, a measure of the photoionizing force, is shown for the case of Mg@C_{60}. The valence levels of the three confined atoms and some high-lying π and σ levels of C_{60} are indicated. Radial probability densities of free and confined atomic levels are shown in figure4.23 (b). The positions of inner and outer edges of the C_{60} hull are also indicated.

Table 4. 3. Valence binding energies (eV) of free and confined atoms.

	Be@C_{60}	Mg@C_{60}	Ca@C60
ηs	-9.49	-7.94	-6.25
ηs@	-7.57	-5.87	-4.04

4.4.2. Low energy plasmonic region

Figure 4.24 shows the TDLDA cross sections for the valence levels ηs@ of the three confined atoms, along with their free atomic counterparts, for photon energies up to 30 eV (Mounted on the broad

cross section shapes of the confined atoms are narrow single-electron autoionizing resonances). First, a confinement induced general trend of the Cooper minima, appearing at the above-threshold region, to shift higher in the energy is noted. Second, the energy range in Figure 4.24 is also the region where the C_{60} giant plasmon is excited. Therefore, the results also show dramatic enhancements in the ionization of confined atoms, peaking at about 16 eV, which are expected from the atom-C_{60} dynamical multielectron coupling [46,47,48]. However, the degree of this enhancement is clearly different from one system to another; in particular $2s@Be$ exhibits the largest cross section while $3s@Mg$ the smallest. In order to uncover the reason of this trend, consider the TDLDA dipole matrix element in equation (4.3), denoted by $\mathcal{M}_{\eta s@}$ in a decomposed single and multi electron picture,

$$\mathcal{M}_{\eta s@}(E) = \mathcal{D}_{\eta s@}(E) + \Delta\mathcal{D}(E), \tag{4.5}$$

where $\mathcal{D}$ is the (LDA) matrix element involving the single electron operator z. The structure of $\Delta\mathcal{D}$, which obviously involves $\delta V'$ (4.2), can be alternatively expressed in the well known Fano scheme based on a perturbative interchannel coupling framework [47] as,

$$\Delta\mathcal{D}(E) = \sum_{nl} dE' \frac{\left\langle \psi_{nl}(E') \left| \frac{1}{\vec{r}_{\eta s@} - \vec{r}_{nl}} \right| \psi_{\eta s@}(E) \right\rangle}{E - E'} \mathcal{D}_{nl}(E'). \tag{4.6}$$

In equation (4.6), $\psi_{\eta s@}(E)$ and $\psi_{nl}(E)$ are the unperturbed final continuum channel wave functions of $\eta s@$ and nl photoionization channels respectively, and the sum is over the photoionization channels of the atom *plus* all the delocalized electron (coherent) channels of the C_{60} shell. Separating out the atomic channels from the sum and associating those terms with the LDA matrix element $\mathcal{D}_{\eta s@}$ we can rewrite equation (4.5) as,

$$\mathcal{M}_{\eta s@}(E) = \mathcal{M}_{\eta s}^{atom}(E) + \Delta\mathcal{D}_{C_{60}}(E), \tag{4.7}$$

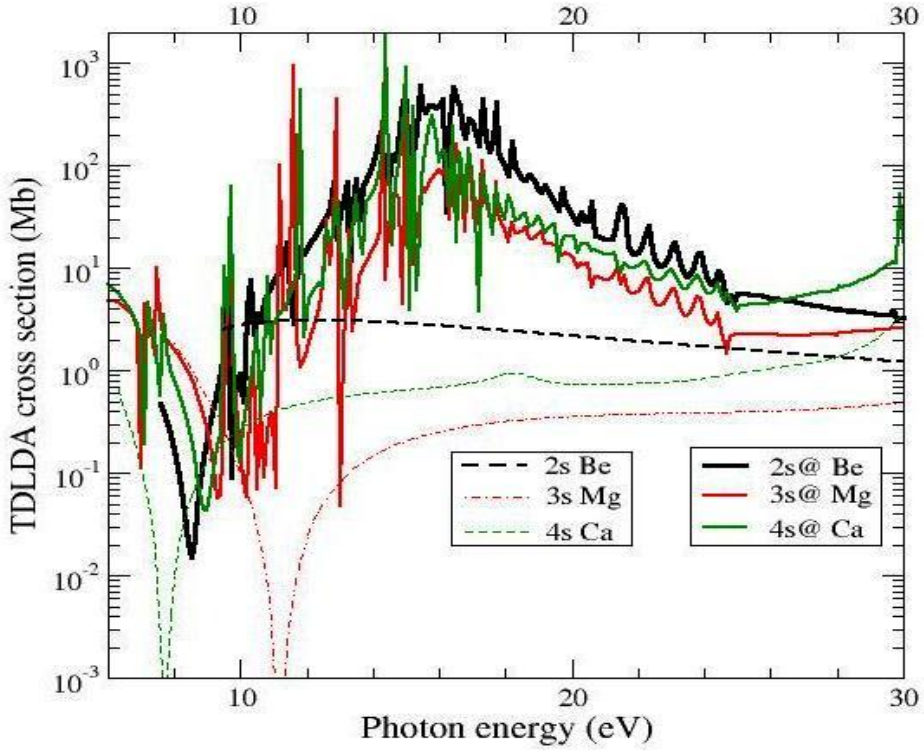

Figure4.24 The valence ionization cross sections corresponding to confined and free atoms, for the three endofullerenes, calculated in TDLDA over the C_{60} plasmon region

where the first term on the right hand side is approximately the TDLDA matrix element of the free atom and the second term, represented by equation (4.6) but without the atomic channels, embodies the plasmonic enhancement. The $\eta s@$ photoionization cross section, $\sim\left|\mathcal{M}_{\eta s@}\right|^2$, in TDLDA therefore involves the coherent superposition of the atomic TDLDA and the enhancement contributions:

$$\sigma_{\eta s@} \approx \sigma_{\eta s}^{atom} + \left[\mathcal{M}_{\eta s}^{atom^*}\,\Delta\mathcal{D}_{C_{60}} + \mathcal{M}_{\eta s}^{atom}\,\Delta\mathcal{D}_{C_{60}}{}^*\right], \qquad \textbf{(4.8)}$$

in which $\Delta\sigma_{C_{60}}\sim\left|\Delta\mathcal{D}_{C_{60}}\right|^2$.

The matrix element within the integral of equation (4.6) is known as the interchannel coupling matrix element. Going from Be to Mg to Ca, the increasing mixing of $\eta s@$ initial state wave function with C_{60} orbitals (Figure4.23(a)) ensures increasing overlaps, resulting in higher values of the interchannel coupling matrix elements. However, along the same atomic sequence there also arises a different effect that counters this trend as follows. Figure 4.23(b) (and Table 4.3) indicates a gradual de-

crease of the $\eta s@$ binding energies from Be to Ca, causing the valence level energetically moving away from the C_{60} σ and π occupied bands (indicated in Figure 4.23(b)). Since the proximity of the ionization thresholds of interacting channels produces stronger overlaps between their continuum wavefunctions, the effect described above will lower the value of the coupling from Be to Ca. It is therefore expected that the competition of these two compensatory effects will keep the value of $\Delta\mathcal{D}_{C_{60}}$, and hence $\Delta\sigma_{C_{60}}$, largely unaltered. Consequently, the comparative differences in $\sigma_{\eta s@}$ up the sequence will primarily be influenced by the free atomic matrix element $\mathcal{M}_{\eta s}^{atom}$ via the interference term in the square bracket on the right hand side of equation (4.8). That is exactly what is found: the free atomic TDLDA matrix elements $\mathcal{M}$ must have increased from Mg to Ca to Be, since their cross sections in Figure 4.24 increase likewise. Therefore, from the above argument, this must also be the trend for the enhanced cross sections of the confined atoms, as clearly seen in the same figure.

4.4.2. High energy oscillatory region

At photon energies above the plasmonic range (roughly >50 eV) the valence $\eta s@$ ionization cross sections show oscillations as a function of the photon energy as seen in Figures 4.25(a–c) for the three systems considered; the curves are seen to oscillate around the corresponding free atom ηs cross sections. Since the many-electron effects largely weaken over this energy region, the single-electron LDA results, obtained by excluding the component $\delta V'$ of the induced potential in equation (4.2), are enough to describe this oscillatory behavior. In Figures 4.25(a) and 4.25(b) we also present results from reference [16] for Be@C_{60} and Mg@C_{60} that compare fairly well with the current LDA results within the limitation of their differences in formalism; for Ca@C_{60}, reference [16] includes a multiconfiguration splitting, making its comparison with our jellium-based result rather difficult.

Within the LDA framework the physical mechanism producing the oscillations can be qualitatively described by the *acceleration* gauge formalism. In this formalism, the dipole photoionization amplitude from equation (4.3), but ignoring correlations, can be expressed as,

$$\mathcal{D}_{nl} \sim \left\langle \phi_{kl'} \middle| \frac{\partial V}{\partial r} \middle| \phi_{\eta s@} \right\rangle, \tag{4.9}$$

which embodies the notion that the electron in the potential $V(r)$requires a force $\frac{\partial V}{\partial r}$ to escape the system. This ionizing force offered by the average radial potential of the compound is displayed in Figure 4.23(a), but only for Mg@C_{60}, which produces characteristic peaks at the inner and the outer edges, $R_i(= 2.70\text{Å})$ and $R_o(= 4.29\text{Å})$, of the C_{60} hull, suggesting the possibility of photoemissions from these locations. Note further in Figure 4.23(a) that, a rather strong force is also available in the central atomic region where the potential changes rapidly. Therefore, since the bound wavefunction $\phi_{\eta s@}$ are non-vanishing over all these force-sites, as is evident from the probability densities presented in Figure 4.23(b), the photoemissions will actually occur from all three sites, significantly interfering with each other owing to the coherence. Additionally, the reflection of the atomic photoelectrons from the hull edges will further enrich the interference, adding features in the modulation that can be best deciphered by the Fourier photo-spectroscopy [67], as we demonstrate in figure 4.25.

The detailed expressions of the general structure of the matrix element, has been derived earlier [67,68]. Following reference [68], we obtain the $\eta s@$ ionization amplitude at energies above the C_{60} plasmon region, as

$$\begin{aligned}\mathcal{D}_{\eta s@}(E) \sim \mathcal{D}_{\eta s@}^{atom}(k) + A_{\eta s@}^{refl}(k)\left[e^{-ikD_o}e^{-iV_0\frac{2\Delta}{k}} - e^{-ikD_i}\right] \\ + A_{\eta s@}^{hull}(k)e^{-i\frac{V_0}{k}}\left[a_i e^{-ikR_i} - a_o e^{-ikR_o}\right]\end{aligned} \tag{4.10}$$

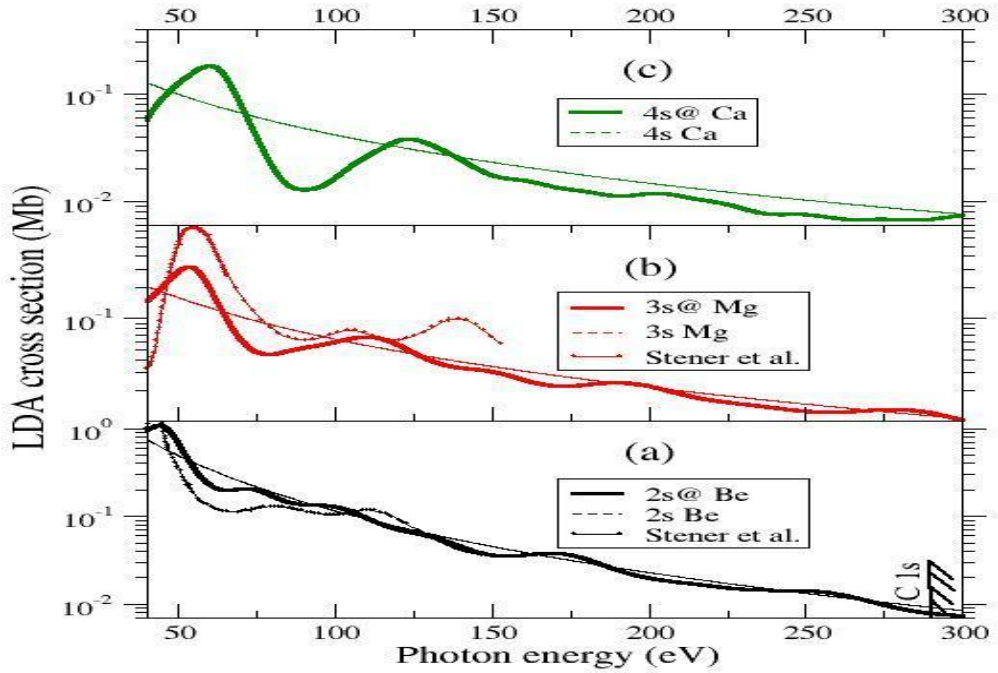

Figure4.25 LDA cross sections of the confined and free atomic valence levels for (a) Be@C_{60}, (b) MgC_{60} and (c) Ca@C_{60}. For the former two systems previous results by Stener et al. [39] are also presented for comparison. The carbon 1s ionization threshold is noted.

in which the photoelectron momentum $k = \sqrt{2(E - \epsilon_{\eta s@})}$ in atomic units, V_0 is the average depth of the hull potential, and a_i and a_o are the values of $\eta s@$ wavefunction at, respectively, R_i and R_o. In equation (4.10), $\mathcal{D}_{\eta s@}^{atom}$ is very nearly equal to the ηs matrix element of an isolated atom and the second term on the right hand side denotes the reflection induced oscillations in momentum space with frequencies $\mathcal{D}_i$ and $\mathcal{D}_o$, the inner and the outer diameter of the hull; the factor $exp\ (-iV_0 \frac{2\Delta}{k})$ rapidly becomes unity with increasing *k*. The third term on the right hand side represents the portion of the overlap integral over the hull region, producing two collateral emissions from the hull edges, where non-zero ionizing forces exist (Figure 4.23(a)); as evident, these contributions produce two frequencies, R_i and R_o, in momentum space. Going from confined Be to Ca, since the $\eta s@$ probability density over the central region slowly diminishes with its corresponding increase in the hull region, the values of a_i and a_o also grow, as Figure 4.23(b) indicates. This evolutionary behavior places, in general, a larger emphasis on the oscillation character of the cross section along the sequence – a feature clearly exhibited in Figure 4.25: oscillations are weakest and strongest respectively for 2s@ Be and 4s@ Ca.

The determination of the cross section involves interferences among atomic, reflective and collateral hull ionization modes. Upon squaring the modulus of equation (4.10) we find,

$$\sigma_{\eta s@} \approx \sigma_{\eta s}^{atom} + \mathcal{D}_{\eta s@}^{atom} \otimes \mathcal{D}_{\eta s@}^{refl} + \mathcal{D}_{\eta s@}^{atom} \otimes \mathcal{D}_{\eta s@}^{hull} , \quad \textbf{(4.11)}$$

where $\mathcal{D}^p \otimes \mathcal{D}^q = \mathcal{D}^{p*}\mathcal{D}^q + \mathcal{D}^p\mathcal{D}^{q*}$, which represents the interferences. Note that since both reflective and collateral effects are generally small relative to the direct ionization, we have disregarded the quadratic reflective, quadratic collateral and reflective-collateral interference terms in equation (4.11). Evidently, the cross section contains the same frequencies as in the matrix element equation (4.10): $\mathcal{D}_i$, $\mathcal{D}_o$ from the reflective and R_i, R_o from the collateral emissions. This is in clear contrast to the known oscillations in free C_{60} [53]. In Figure 4.26 the Fourier transform magnitudes (FTM) of confined-to-free cross section ratios for $\eta s@$ ionizations of the three systems are shown. These *reciprocal* spectra yield four peaks at the expected radial positions. The height of each peak represents the strength of the respective oscillation via the factor in front of the corresponding oscillatory term in equation (4.10). We note the following: (i) the reflective structures are generally smaller than the collateral ones for all the systems. This is because while with increasing photoelectron momentum the reflection probability decreases, a faster electron can better resolve the force structure at the hull edges. (ii) The collateral peaks become progressively taller going from Be to Ca, since a_i and a_o are increasingly larger along the sequence (Figure 4.23(b)). (iii) In general for all three systems the R_o collateral peak is higher then the R_i peak, since $a_o > a_i$ without exceptions.

State-selective measurements of photoelectrons from confined atoms can in principle be carried out by the standard technique of electron spectroscopy. But, the photon energy must not intrude on the carbon *K*-shell continuum to ensure that the C^{4+} core is not ionized. Hence, we examined if the FTM of cross section ratios for energies *not* exceeding 290 eV is capable of delineating the effect. Barring some off-sets, the peak positions are very well reproduced (Figure 4.25), implying that the effect should be discernible in the experiment and must be included to interpret the data.

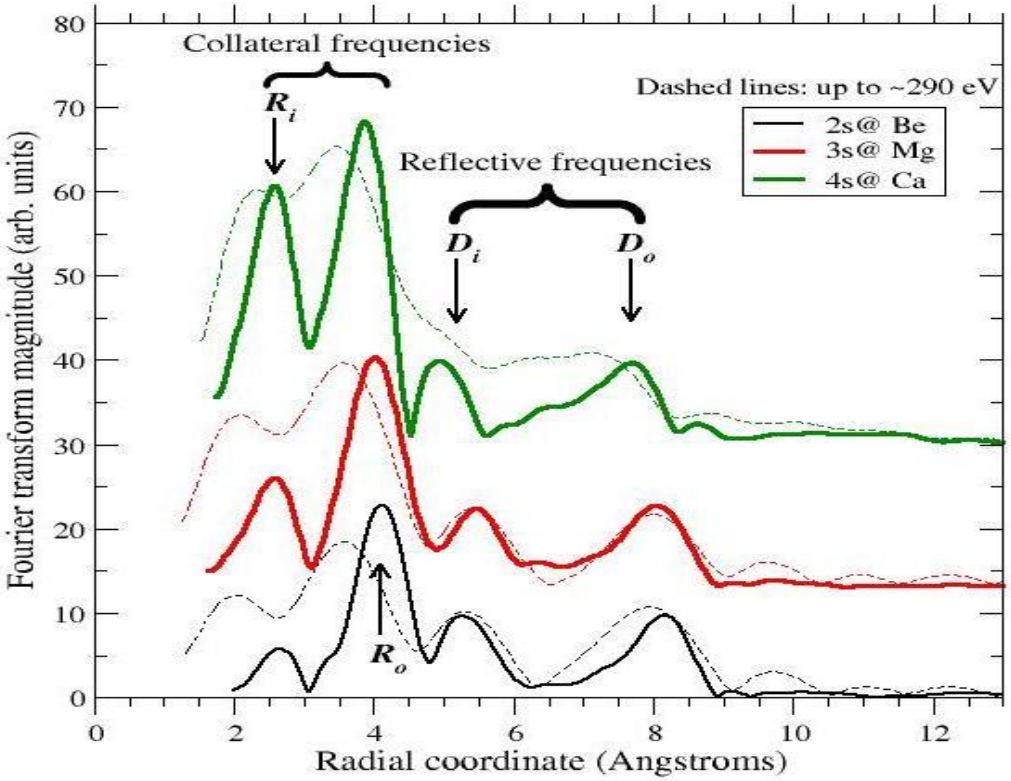

Figure4.26 Fourier transform magnitudes of confined-to-free LDA cross section ratios over extended and limited (up to carbon K edge) energy ranges

4.5. Photoionization of Small Fullerenes C_n (n=28, 32, 40, 44, 50)

4.5.1. Introduction

In experimental atomic physics many interesting phenomena are observed due to correlated electron motion. For infinitely extended object, surface or bulk matter, electron correlations induced collective phenomena, that are describe in terms of plasmons. For large system like carbon clusters one type of plasmon excitation are describe as a surface resonance of negative charge density (delocalized electrons) oscillates like fluid against the positive background (ions). For C_{60} in gas phase, a giant resonance of this surface plasmon was first observed around 20 eV photon energy [69]. Theoretically, this resonance was predicted by calculating the response of the C_{60} system to the external electromagnetic field using random-phase approximation [70]. Also due to the spherical symmetry of the C_{60} in some other theoretical approximation this resonance are reported [71,72].

A different class of photoionization cross section calculations of C_{60} has emerged that considered each carbon atom in C_{60} has 4 delocalized electrons, and 60 C^{4+} ions formed a classical jellium shell [51,73,9]. In this model, the ion cores are fixed in the C_{60} structure and the dynamics of the 240 delocalized remaining electrons are treated self-consistently. The description of this surface plasmon resonance requires inclusion of many body effects by electron correlation. In two ways these correlations can be included: (i) the random phase approximation (RPA) (ii) time dependent local density approximation (TDLDA), both types of calculations have revealed the surface plasmon resonance [70,51,74,75]. The new photoionization cross section calculation using jellium-based TDLDA for single ionized C_{60} have shown the second surface plasmon resonance around 40 eV [17], that has good agreement with recent experimental result for this second resonance [76]. Also, using the same method, calculations have been done for endohedral fullerene (Atome@C_{60}) by putting different atoms at the center of C_{60} [49,77]. In these calculations very interesting phenomenon known as hybridization, due to the overlap of the near degeneracy same symmetry wave functions of the trapped atom and C_{60} shell, is happened, that completely changes the photoionization cross sections of the mixed states.

In this section, using the same method as above (jellium-based TDLDA), we describe our calculations and present results for the photoionizations of small fullerenes C_n (n=28, 32, 40, 44, 50). The reason that we choose these fullerenes is that for all of them the near spherical isomers can be found [78,79,80,81,82] so that approximating them as spherical is justified.

4.5.2.Total cross section

The total photoionization cross sections calculated in the TDLDA for each fullerene are represented in figures 4.27-4.31. For all the cases two regions of enhancement, surface plasmon resonances, around 20 ev and 40 eV can be seen. A phase-coherent interchannel coupling mechanism is found to cause enhancements in subshell cross sections, the constructive superposition of enhancements from

various subshells exactly at the energies of plasmon excitations generates the collective resonances. The first one that has lots of autoionization resonances is known as giant dipole surface plasmon resonance [17]. The second plasmon resonance is far weak. This structure was reported in the recent experiment-theory joint study on C_{60} ions [9], and also for neutral C_{60} [76]. Furthermore, these resonances for all cases are down shifted in energy with increasing the number of carbon atom in fullerenes (table 4.4).

Table 4. 4. Positions of the plasmon resonances in a variety of small fullerenes.

Fullerene	First plasmon resonance(eV)	Second plasmon resonance (eV)
C_{28}	20.00	41.96
C_{32}	17.96	39.94
C_{40}	17.48	39.83
C_{44}	15.92	39.69
C_{50}	15.46	37.14

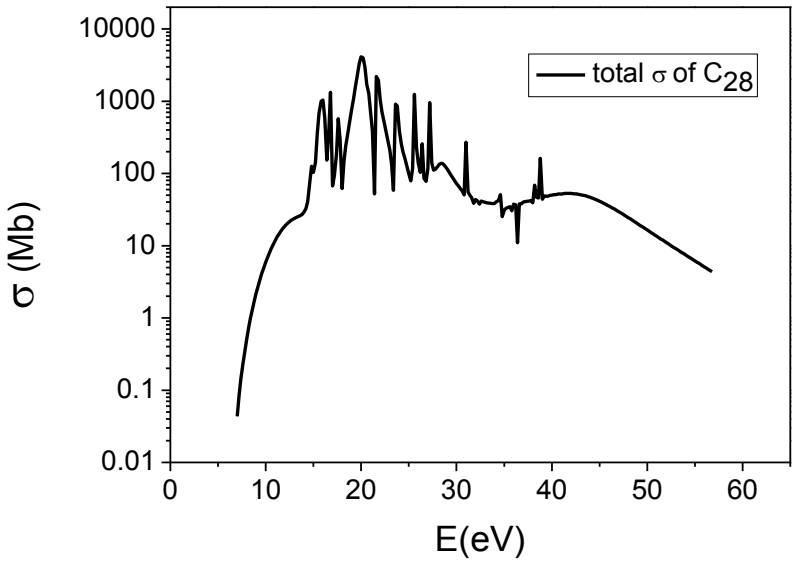

Figure4.27 Total cross section of C_{28}

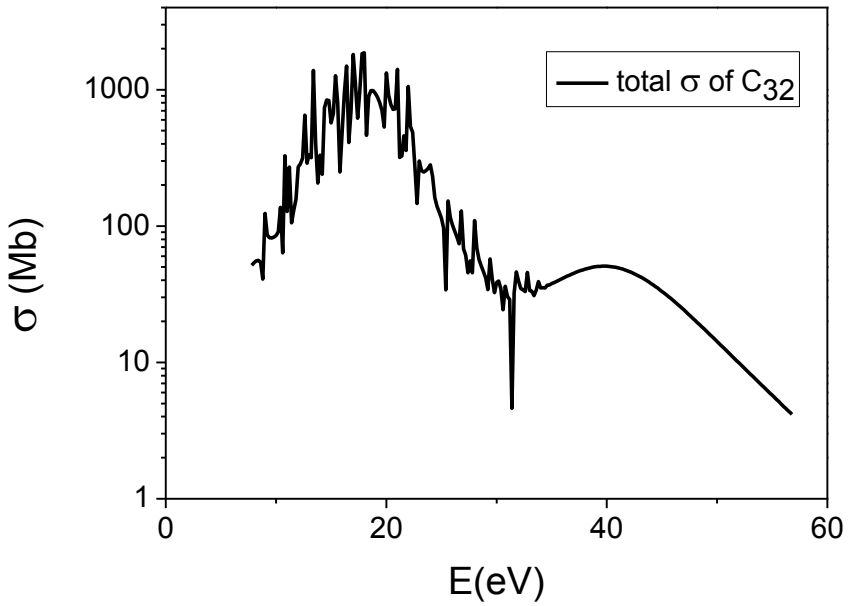

Figure 4.28 Total cross section of C_{32}

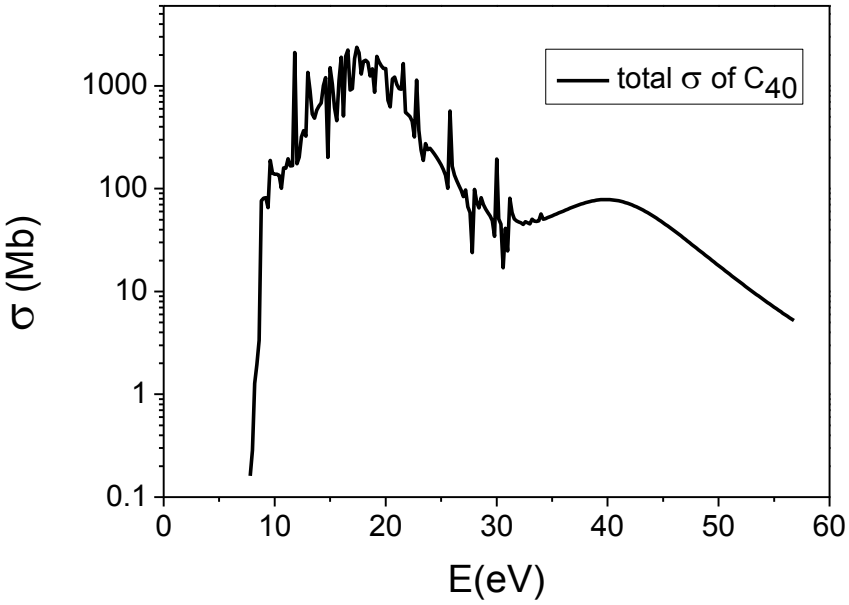

Figure 0.29 Total cross section of C_{40}

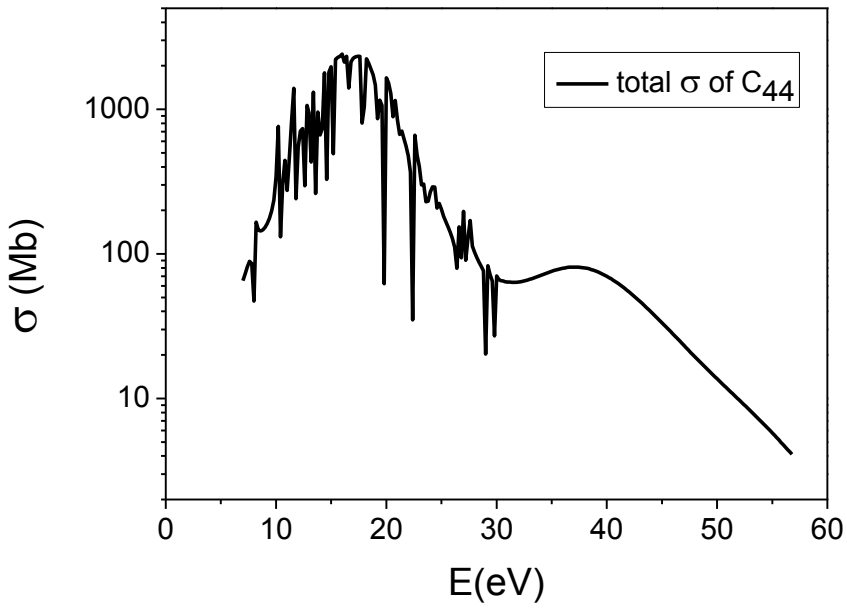

Figure0.30 Total cross section of C_{44}

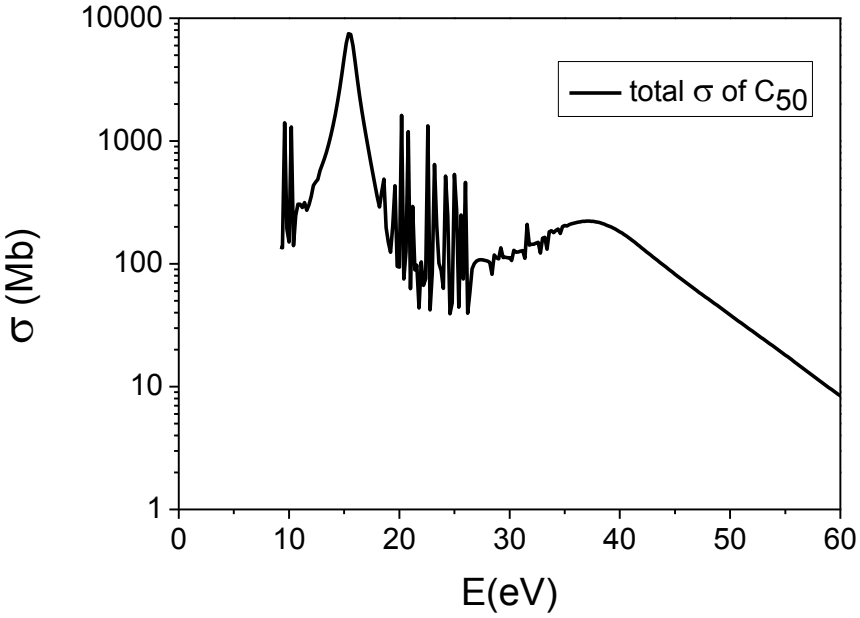

Figure4.31 Total cross section of C_{50}

4.5.3.Oscillator strength

Since the total oscillator strength for a photoabsorption process equals the number of electrons in the target [83], this means that, in these cases generally, the oscillator strength should be increasing with increasing number of electron (4 × n). But this sum is true for the sum over two regions, discrete and continuum, and the present calculation is only over the continuum region ; however, knowing the total, the split of oscillator strength between these two regions can be made, as shown in table 4.5.

Table 4. 5. Distribution of oscillator strength between discrete and continuum region for small fullerenes.

Fullerene	Oscillator strength in continuum	Oscillator strength in discrete
C_{28}	101.1	112-101.1=10.9
C_{32}	95.9	128-95.9=32.1
C_{40}	133.9	160-133.9=46.1
C_{44}	157.2	176-157.2=18.8
C_{50}	149	200-149=51

In the table it is seen that oscillator strength in the continuum generally increases with the number of electrons, but this increase is certainly not monotonic. This illustrated that, to understand the oscillator strength distribution, the detailed molecular structure must be understood and not simply the number of electrons.

4.6. Resonant Auger-intercoulombic hybridized decay in the photoionization of endohedral fullerenes

Intercoulombic decay (ICD), originally predicted by Cederbaum [84] and observed initially for Ne clusters [85], is a unique, naturally abundant nonradiative relaxation pathway of a vacancy in atom A in a cluster or molecule. An outer electron of A fills the vacancy and the released energy, instead of emitting a second electron of A as in standard Auger ionization, transfers to a neighboring atom B *via* Coulomb interactions to ionize B. Repulsion between holes in A and B may lead to fragmentation. Over the last decade and a half, a wealth of theoretical [86] and experimental [87] research has gone into studying ICD processes in weakly bound atomic systems. These involve the observation of ICD in rare gas dimmers [88], rare gas clusters [89], surfaces [90], and small water droplets [91,92]. ICD followed by resonant Auger decay has been identified in Ar dimers using momentum resolved electron-ion-ion coin-

cidence spectroscopy [93,94]. Ultrafast ICDs of a dicationic monomer in a cluster to produce a cluster tricataion [95] or multiply excited homoatomic cluster [96] were predicted. Also, time domain measurements of ICD in He [97] and Ne [98] dimers have recently been achieved. Besides fundamental science contexts, low energy ICD electrons find potential medical applications in the treatment of malignant cells [99].

Of particular interest is the resonant ICD (RICD) where the precursor excitation to form an inner-shell vacancy is accomplished by promoting an inner electron to an excited state by an external stimulant, generally electromagnetic radiation [100,101] or, more recently, charge particle impact [102]. A theoretical study of RICD followed by Ne $2s \rightarrow np$ excitations in MgNe clusters suggested the leading contribution of RICD among other interatomic decay modes [103]. Photoelectron spectroscopy with Ne clusters for $2s \rightarrow np$ excitations measured the signature of RICD processes [100]. Similar excitations in the double photoionization of Ne dimers were utilized to observe RICD by tracking the formation of energetic Ne^+ fragments [101]. Most recently, strong enhancement of the $HeNe^+$ yield, as He resonantly couples with the radiation, is detected [104], confirming an earlier prediction [105].

Atoms confined in fullerene shells forming endofullerene compounds are particularly attractive natural laboratories to study RICD processes. There are two compelling reasons for this: (i) such materials are highly stable, have low-cost sustenance at the room temperature and are enjoying a rapid improvement in synthesis techniques [106]; and (ii) the effect of correlation of the central atom with the cage electrons have been predicted to spectacularly affect the atomic photoionization [47]. A first attempt to predict ICD in endofullerenes was made by calculating ICD rates for $Ne@C_{60}$ [107]. While some speculation on the role of Coulomb interaction mediated energy transfer from atom to fullerene to broaden Auger lines has been made [108,109], no studies, theoretical or experimental, of RICD resonances in the ionization cross section of endofullerenes have been performed. Furthermore, ICD of endofullerene molecules can uncover effects not yet known. This is because: (i) endofullerenes being

spherical analogues of asymmetric dimers consisting of an atom and a cluster can also induce reverse RICD processes, the decay of cluster innershell excitations through the continuum of the confined atom, of uniquely different character than the forward RICD; and (ii) possibilities of atom-fullerene hybridized final states, predicted to exist abundantly in these systems [50,77], can significantly alter the properties of intercoulombic processes.

In this research, we show that for an Ar atom endohedrally sequestered in C_{60}, ICD pathways of photogenerated innershell holes, both in the central atom and the fullerene, can coherently mix with degenerate *intracoulombic* Auger pathways to produce final states with *shared* holes in atom-fullerene hybrid levels. Figure 4.32 presents a schematic of the process which illustrates this hitherto undetected mode that can be called the resonant hybrid Auger-intercoulombic decay or RHA-ICD.

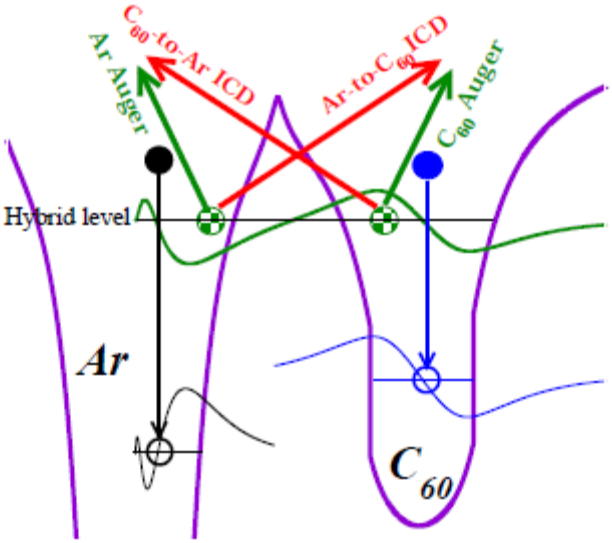

Figure 4.32 Schematic of coherent mixings of onecenter Auger decays (green) of core holes with responding ICDs (red) in the spectra of Ar-C_{60} hybrid electrons

A jellium based time-dependent local density approximation (TDLDA), with the Leeuwen and Baerends (LB) exchange-correlation functional to produce accurate asymptotic behavior for ground and continuum states (109), is employed to calculate the dynamical response of the system to the external electromagnetic field produced by the incident photon. The Ar nucleus is placed at the center of the

sphere where the chemically inert noble gas atom is known to localize. In solving the Kohn-Sham equations to obtain the ground state wave function, a few essential optimizations were adopted [46]. The model has enjoyed earlier success in co-discovering with experimentalists a high energy plasmon resonance [9], interpreting the energy-dependent oscillations in C_{60} valence photo-intensity data [53], and predicting giant enhancements in the confined atom's photoresponse from the coupling with C_{60} plasmons [47]. Significant ground state hybridization of Ar $3p$ is found to occur with the C_{60} $3p$ orbital, resulting in two levels, $(Ar + C_{60})3p$ and $(Ar - C_{60})3p$, from respectively, the symmetric and antisymmetric modes of mixing, the spherical analogs of bonding and antibonding states in molecules or dimmers,

$$(Ar \pm C_{60})3p = |\phi_{\pm}\rangle = \sqrt{\alpha}\,\left|\phi_{3pAr}\right\rangle \pm \sqrt{1-\alpha}\left|\phi_{3pC_{60}}\right\rangle, \quad \textbf{(4.12)}$$

where $\alpha \approx 0.5$. Such atom-fullerene hybridization was predicted earlier [50] and detected in a photoemission experiment on multilayers of Ar@C_{60} [110]. In fact, the hybridization gap of 1.52 eV between $(Ar + C_{60})3p$ and $(Ar - C_{60})3p$ in our calculation is in good agreement with the measured value of $1.6 \pm 0.2\ eV$ [110]. We use the symbol $nl@$ to denote the levels of the confined atom and $@nl$ to represent the levels of the doped C_{60}.

Figure 4.33 shows the 3p photoionization cross section of free Ar calculated using TDLDA. Two Auger window-resonances at 27.2 eV and 28.6 eV correspond to regular autionizing states formed by two lowest innershell excitations $3s \rightarrow 4p, 5p$. We also present in Figure 4.33 the cross sections for C_{60} $@7h$, which is the highest occupied (HOMO) level of C_{60} π symmetry (one radial node), and for $@2s$, which is the state at the bottom of the π band. Both these cross sections exhibit a host of routine autoionizing resonances corresponding to C_{60} innershell excitations which also appear in the C_{60} total cross section (shown) at about the same energies. Three rather weak features, labeled as A, B, and C in Figure 4.33, are noted in the $@7h$ and $@2s$ curves which do not have partners in the free C_{60} cross section. However, these are Ar-to-C_{60} ICD resonances, resulting from the decay of Ar $3s@$ vacancies from $3s@ \rightarrow$

$3p@, 4p@, 5p@$ excitations, through C_{60} $@7h$ and $@2s$ continua. Slight red-shifts in the position of these resonances compared to their free Ar counterparts are due to some adjustments in $3s$ ground and np excited energies arising from confinement. Note that these structures are from participant RICD processes only, as the spectator RICD is not included within TDLDA.

Figure 4.34 displays cross sections, over the same energy range of Figure 4.33, for the endofullerene hybrid levels, $(Ar \pm C_{60})3p$. Features A, B, and C in these curves are resonances that

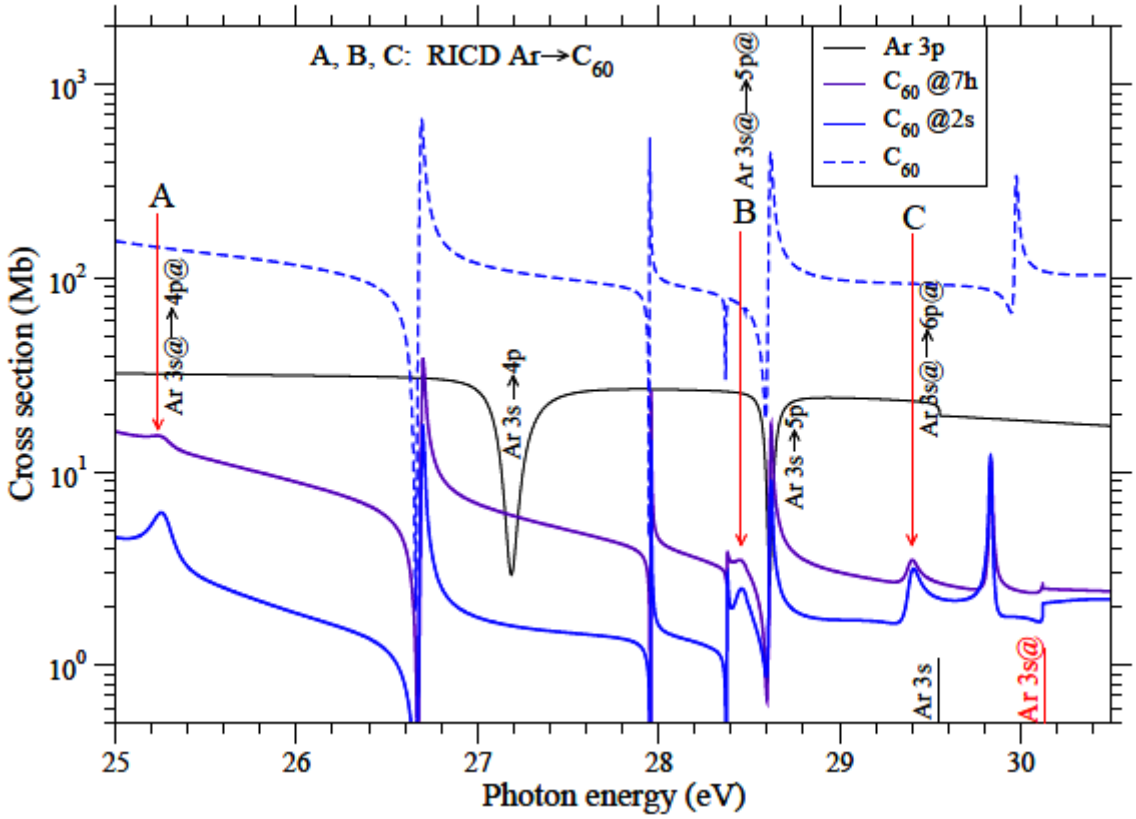

Figure4.33 Photoionization cross sections of free Ar 3p and empty C_{60} compared with the results for C_{60} @7h and @2s levels in Ar@C_{60}. Three Ar-to-C_{60} ICD resonances (labeled as A,B,C) amongst regular autoionizing resonances are identified in the C_{60} @7h and @2s cross sections.

emerge from the decay of $3s@ \rightarrow 3p@, 4p@, 5p@$ excitations through the continuum of these hybrid levels. These features are similar in shape to the autoionizing resonances in free Ar $3p$ (included in Figure 4.34) and appear at the same Ar-to-C_{60} RICD energies (Figure 4.33). Remarkably, they are significantly stronger, particularly for $(Ar - C_{60})3p$, than the Ar-to-C_{60} RICDs. Another dramatic effect can be not-

ed: The empty C_{60} 3*p* cross section in Figure 4.34 shows autoionizing resonances corresponding to Auger decays of C_{60} innershell vacancies. But the structures at the corresponding energies in hybrid channels from the decay of C_{60} vacancies through the hybrid continuum are order of magnitude larger than the autoionizing resonances in empty C_{60}. We particularly identify the resonances labeled as 1 to 4 in Figure 4.34. In essence, Ar and C_{60} innershell vacancies decay significantly more powerfully through the photoionization continua of $Ar - C_{60}$ hybrid levels than they do through the continua of pure C_{60} levels. These resonances are qualitatively different than the standard RICD. We show below that they emerge from a coherent interference between resonant Auger and intercoulombic channels that produce *divided* vacancies in the final state, vacancies shared by the confined atom and the confining fullerene.

The TDLDA matrix elements for the dipole photoionization of $(Ar \pm C_{60})3p$ levels, in the perturbative interchannel coupling framework introduced by Fano [60], can be written as [49],

$$\mathcal{M}_{\pm}(E) = \mathcal{D}_{\pm}(E) + M_{\pm}^{c-c}(E) + M_{\pm}^{d-c}(E), \quad \textbf{(4.13)}$$

where the single electron (LDA) matrix element $\mathcal{D}_{\pm}(E) = \langle ks(d)|z|\phi_{\pm}\rangle$; $M^{c-c}$and M^{d-c} are respectively corrections from continuum-continuum and bound-continuum channel couplings. M^{c-c} constitutes the many-body contribution of relatively smooth nonresonant ionization cross section, while the resonance structures originate from M^{d-c} [60],

$$M^{d-c} = \sum_{nl}\sum_{\eta\lambda} \frac{\left\langle \psi_{nl\to\eta\lambda}\left|\frac{1}{r_{\pm}-r_{nl}}\right|\psi_{\pm}(E)\right\rangle}{E - E_{nl\to\eta\lambda}}\, \mathcal{D}_{nl\to\eta\lambda}\ , \quad \textbf{(4.14)}$$

in which the $|\psi\rangle$ refer to interacting discrete $nl \to \eta\lambda$ and continuum $(Ar \pm C_{60})3p \to ks(d)$ *channel* wavefunctions; $E_{nl\to\eta\lambda}$ and $\mathcal{D}_{nl\to\eta\lambda}$ are LDA bound-to-bound excitation energies and matrix elements, respectively. The excited states of the endofullerene are found to be hybridized, implying that innershell electrons from pure levels are excited to the hybrid levels. But we do not expect significant differences in $\mathcal{D}_{3s\to\eta p}$ from this effect between free and confined Ar.

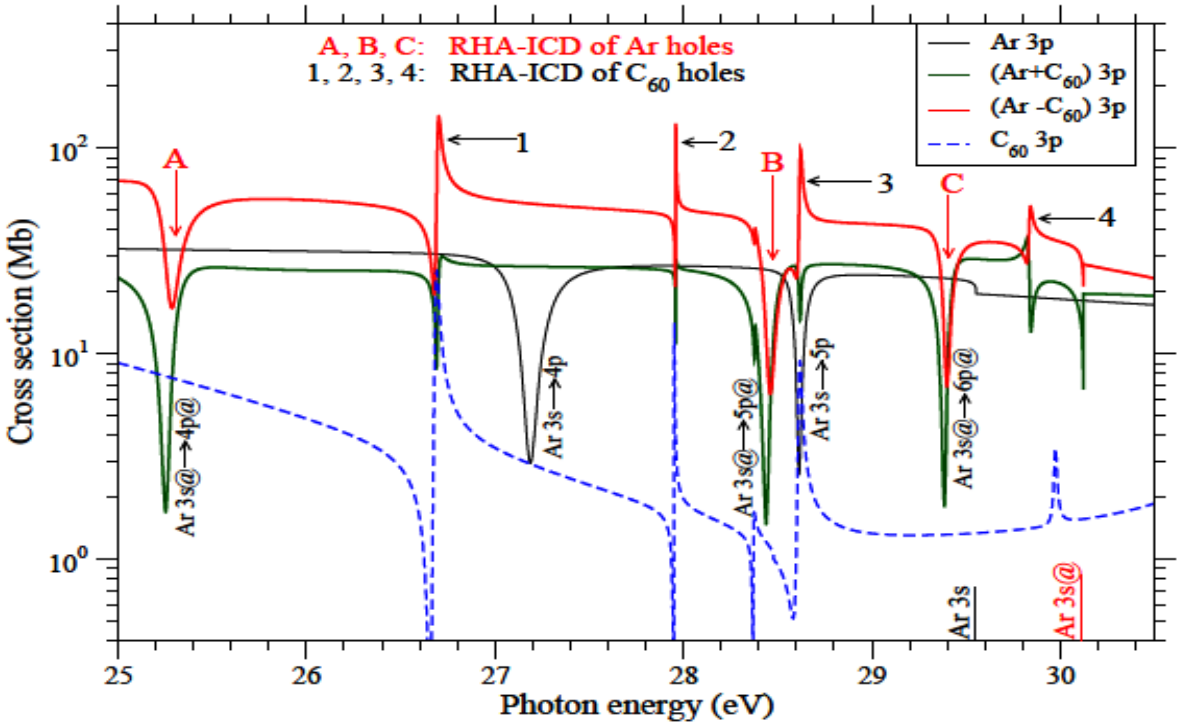

Figure4.34 Photoionization cross sections of free Ar 3p and C_{60} 3p levels compared with those of their hybrid pair

This is because, even though hybrid excited waves develop structures at C_{60} shell, the Ar 3*s* wavefunction continues to localize on Ar (Figure 4.32), qualitatively unaffecting the overlaps. Obviously, an identical reason also ensures practically unchanged C_{60} inner excitation matrix elements from the doping.

Following (4.12), the hybridization of the continuum channels in (4.14) assumes the form

$$|\psi_{\pm}\rangle = \sqrt{\alpha}|\psi_{3p@Ar}\rangle \pm \sqrt{1-\alpha}|\psi_{@3pC_{60}}\rangle\,. \qquad \textbf{(4.15)}$$

In (4.15) we used @ to indicate the inclusion of the modifications of the continuum waves of the confined Ar and doped C_{60}. Using (4.15) in (4.14), and recognizing that the overlap between a pure Ar bound state and a pure C_{60} bound state is negligible, we can separate the atomic and fullerene regions of integration to obtain. Obviously, if $nl \to \eta\lambda$ produces Ar innershell holes, resulting to resonances A, B, and C in Figure4.34, then the first term on right-hand-side of (4.16) represents the ordinary *intracoulombic* Auger decay in Ar, while the second term denotes the Ar-to-C_{60} RICD. Conversely, for C_{60}

inner vacancies (resonances 1-4 in Figure 4.34), the first and second term, respectively, present reverse RICD (C_{60}- to-Ar) and C_{60} Auger processes. The decays are shown schematically in Figure 4.32.

$$M_{\pm}^{d-c}(E) = \sum_{nl}\sum_{\eta\lambda}\left\{\begin{array}{c} \sqrt{\alpha}\,\dfrac{\left\langle \psi_{nl\to\eta\lambda}\left|\dfrac{1}{r_{\pm}-r_{nl}}\right|\psi_{3p@Ar}(E)\right\rangle}{E-E_{nl\to\eta\lambda}} \\ \pm\sqrt{1-\alpha}\,\dfrac{\left\langle \psi_{nl\to\eta\lambda}\left|\dfrac{1}{r_{\pm}-r_{nl}}\right|\psi_{@3pC_{60}}(E)\right\rangle}{E-E_{nl\to\eta\lambda}} \end{array}\right\}\mathcal{D}_{nl\to\eta\lambda} \qquad \textbf{(4.16)}$$

For the ionization cross sections, which involve the modulus squared of the amplitude, two important mechanisms play out: First, Auger and intercoulombic decay pathways in (4.16) combine coherently to induce resonances, allowing the creation of shared outershell vacancies. Therefore, this decay pathway can be called resonant hybrid Auger-intercoulombic decay (RHA-ICD). Note that both the terms in (4.16) are large, owing to substantial overlaps between innershell bound states and $(Ar \pm C_{60})3p$ hybrid wavefunctions. This partly explains why the features identified in Figure 4.34 are stronger than corresponding autoionizing and ICD resonances. Second, the resonances in the matrix element $M_{\pm}^{d-c}$ also interfere with the nonresonant part $\mathcal{D}_{\pm} + M_{\pm}^{c-c}$, (4.13), which is generally stronger for hybrid levels than pure C_{60} levels [77]. This interference, consequently, enhances RHA-ICD resonances compared to their Auger partners in pure C_{60} channels, as seen for structures 1-4 in Figure4.34. The results exhibit completely different resonance shapes for Ar-to-C_{60} RICDs (Figure4.33) compared to corresponding RHA-ICDs (Figure 4.34), although their lifetimes increase only slightly. Noticeably, the lifetime (130 fs) of the Auger feature 1 decreases to about 40 fs for the respective RHAICDs (Figure 4.34), while there is a strong shape-alteration for the feature 4. Lastly, hybrid final-state vacancies may have unique consequences for the spectator type RHAICD: the post-decay repulsive force will considerably increase compared to RICD, since a half vacancy will reside too close to a full vacancy either on Ar or on C_{60}, allowing stronger fragmentation forces.

RICD systems are visualized as natural antenna receiver pairs at the molecular scale [104] where the antenna couples to the incoming photon and transfers energy to the receiver to perform. RHA-ICD

processes, predicted here, can enhance the efficiency of the ultimate output by enabling the antenna to also contribute to the emission resonantly with the receiver through a quantum coherence. The effect may have significant utilization in nanoscale antenna technology [111].

5.CONCLUSION

Calculations of the photoionization of the outer and intermediate subshells of the noble gas atoms He through Xe, confined at the center of the fullerene molecule C_{60}, have been performed using a time-dependent local density approximation methodology. The results show confinement oscillations are predicted generally in the confined cross sections of all subshells of all atoms. In the lower energy region, the region of the plasmons in the free C_{60} cross section, it was found that interchannel coupling dramatically increased the cross sections of the entrapped atoms in all cases. Mixing between bound state wave functions of the C_{60} shell and the enclosed atom, hybridization, was found in a number of cases, but there appear to be no obvious systematics to which subshells of which atoms are hybridized. It was also noted that the binding energies of the hybridized states tended to be much closer to the energies of the C_{60} component of the hybrid, and this was explained in terms of the relative sizes of the perturbation to each state. It is important to note that these effects should be generally in evidence for the photoionization of any atom confined at the center of C_{60}.

It was also shown that at energies away from the C_{60} plasmon resonances, i.e., above the photon energy of 40 eV or so, in cases where there is little or no hybridization, that the simple static model should be adequate to describe the photoionization of confined atoms. From a practical point of view, this means inner subshells with biding energies greater than about 40 eV; not only do they miss the plasmon region, but their wave functions are so compact that there is essentially no overlap with the shell wave functions, so that no hybridization occurs.

The only relevant experimental results involve studies of the 4*d* subshell Xe@C_{60} [11]which confirmed the existence of confinement resonances. A detailed comparison [11] with essentially the same cal-

culation reported in this paper showed good qualitative agreement, but quantitative discrepancies; some of the reasons for these were discussed.

And where do we go from here? Among the improvements/enhancement that are required is a relaxation of spherical symmetry, which would allow the treated of atoms trapped inside a fullerene but off-center, and atoms confined in nonspherical fullerenes. In addition, the K-shell photoionization of the carbon atoms making up the C_{60} shell, which is omitted in the present calculation, needs to be included. Finally, at the higher photoelectron energies, where the photoelectron wave length becomes comparable with the separation of the carbon atoms in the fullerene shell, the discrete nature of these contributions to the potential must be included as opposed to a smeared-out jellium model. Clearly much work needs to be done.

This study of the photoionization of three different alkali earth atoms confined at the center of a C_{60} molecule reveals a number of insights. The phenomenon of hybridization, the mixing of atomic and shell wave functions, is seen. The details of this hybridization is, however, quite atom-dependent; it depends upon the proximity of atomic energy levels to energy levels of the confining C_{60} of the same symmetry. In all cases, in the energy vicinity of the giant plasmon in C_{60}, there is a dramatic enhancement of the valence cross section of the caged atom, an effect that is explained in terms of interchannel coupling between the C_{60} photoionization channels and the atomic channels. The analysis reveals the interference with the atomic ionization amplitude, *not* the extent of atom-C_{60} wavefunction mixing, to be the key in determining the relative enhancement that increases from Mg to Ca to Be. In addition, well above the plasmonic region, the valence cross sections of all three atoms exhibit confinement resonances, oscillations engendered by the interference of photoelectron waves emitted directly with those (i) scattered from the inner and outer boundary of the confining potential and (ii) emerged directly collaterally from these boundaries. These oscillations for each of the atoms differ in detail from one another, but the Fourier transform of the cross sections reveals geometric information on the confining shell which is, of course, exactly the same for all three

atoms. However, the orbital-mixing plays a crucial role in altering the intensity of the collateral oscillation component which grows maximally for Ca, since the mixing yields the highest number of collateral electrons for this system. Unfortunately, owing to the difficulty of producing these confined atom systems in quantity, there is as yet no experimental scrutiny of these systems. It would be highly desirable to measure these cross sections quantitatively and to look at these systems via photoelectron spectroscopy to separate individual channels. Such studies could answer many questions as well as provide a benchmark for theoretical calculations.

The photoionization cross section of small fullerenes C_n (n=28, 32, 40, 44, 50) are calculated in a TDLDA framework that include all essential many-body correlations to treat the motion of 4n delocalized electrons for each case. The carbon ion cores are represented by a spherical jellium shell. For each of them, the total cross section result shows two plasmon resonances around 20 eV and 40 eV to the photoionization cross section. Also, a phase-coherent interchannel coupling mechanism is found to cause enhancements in subshell cross sections, the constructive superposition of enhancements from various subshells exactly at the energies of plasmon excitations generates the collective resonances. Total oscillator strength is increasing with n due to the increasing in the number of electrons (4×n) in different fullerenes, C_n, but this increase is not uniform in the range 0 eV and 60 eV. The rest of the strength for each case would be either at high energies or in the discrete; and because the cross sections are very small at high energies most of the rest of the oscillator strength would go to the discrete region. The peak positions of both the plasmons are down-shifting in energy as n increases.

In addition, we used the TDLDA methodology to calculate a variety of single-electron resonances in the photoionization of $Ar@C_{60}$. Ar-to-C_{60} ICD resonances are calculated for the first time. A different class of resonances decaying into atom-fullerene hybrid final state vacancies has been found which arise from the interference of the intracoulomb autoionizing channel with an intrinsically connected intercoulomb channel. These resonances are significantly stronger than both regular ICD and Auger resonances, which make

them amenable for experimental detection. They are likely to exist generally in the ionization continuum of, not only atomic endofullerenes, but of molecules, nanodimers, and fullerene onions that support hybridized electrons as well.

In future, we need to expand our present capabilities to study more complex systems such as non-spherical carbon clusters such as non-spherical fullerens, double layer fullerens, and carbon nano-tubes, also atoms and molecules trapped inside them. Such systems have shown very interesting properties experimentally and have been suggested for a number of possible applications. We would also like to study the photoelectron angular asymmetry parameters and phase shifts. The phase shifts can be used to determine the time delay of the photoelectrons [112].

Further, while the TDLDA methodology is a useful tool to understand the qualitative behavior of a complex system, R-matrix methods would be much more quantitatively accurate. Thus, we would like to move in the direction of looking at the photoionization of fullerene and endohedral fullerenes with R-matrix; this could involve large numbers of basis states and channels in a parallelized code environment. Furthermore, for accuracy in heavy systems, we would like to employ the R-matrix version based on the Dirac Equation, so as to include relativistic interaction *ab initio*. And once done for photoionization, electron impact ionization could be done with the same codes.

Finally time-dependent behavior is becoming increasingly important, especially as experiments are now being performed at the attosecond level, particularly for short and intense laser interactions with atoms and molecules. A time-dependent R-matrix approach is an ideal methodology to attach these problems non-perturbatively. Starting with simple atoms to prove the technique, we could then move on to more complex systems. The idea would be to understand the physics of how the pulse duration and intensity affect the reaction, along with how the existence of correlation within the target system, affects the results.

REFERENCES

[1] L. Dunsch S. Yang, "Metal Nitride Cluster Fullerenes: Their Current State and Future Prospects," *Small*, vol. 3, 2007.

[2] A. S. Baltenkov, J.P. Connerade and S. T. Manson V. K. Dolmatov, "Stucture and Photoionization of Confined Atoms," *Radiation Phys. Chem.*, vol. 70, 2004.

[3] K.V.Dolmatov, *Advances in Quantum Chemistry: Theory of Quantum Confined Systems*. New York: Academic, 2009.

[4] J.P.Connerade, "Structure and Dynamics from the Nuclear to the Biological Scale," in *The Fourth International Symposium Atomic Cluster Collisions (ISACC 2009)*, Ann Arbor, 2009.

[5] C. Boehme, S. Schaefer, K. Huebener, K. Fostiropoulos, and K. Lips W. Harneit, "Room Temperature Eletrical Detection of Spin Coherence in C60," *Phys. Rev. Lett.*, vol. 98, 2007.

[6] M. E. Pearce, and A. K. Salem J. B. Melanko, *Nanotechnology in Drug Delivery*. New York: Springer, 2009.

[7] C. M. Cardona, D. M. Guldi, S. G. Sankaranarayanan, M. O. Reese, N. Kopidakis, J. Peet, B. Walker, G. C. Bazan, E. V. Keuren, B. C. Holloway, and M. Drees R. B. Ross, "Endohedral fullerenes for organic photovoltaic devices," *Nat. Mater.*, vol. 8, 2009.

[8] Y.H. Kim, A. C. Dillon, M. J. Heben, and S. B. Zhang Y. Zhao, "Hydrogen Storage in Novel Organometallic Buckyballs," *Phys. Rev. Lett.*, vol. 94, 2005.

[9] E. D. Emmons, M. F. Gharaibeh, R. A. Phaneuf, A. L. D. Kilcoyne, A. S. Schlachter, S. Schippers, A. Müller, H. S. Chakraborty, M. E. Madjet, and J. M. Rost S. W. J. Scully, "Photoexcitation of a Volume Plasmon in C60 Ions," *Phys. Rev. Lett.*, vol. 94, 2005.

[10] S. Schippers, M. Habibi, D. Esteves, J. C. Wang, R. A. Phaneuf, A. L. D. Kilcoyne, A. Aguilar, and L. Dunsc A. Müller, "Significant Redistribution of Ce 4d Oscillator Strength Observed in Photoionization of Endohedral Ce@C+82 Ions," *Phys. Rev. Lett.*, vol. 101, 2008.

[11] A. Aguilar, A. Muller, S. Schippers, C. Cisneros, G. Alna'Washi, N. B. Aryal, K. K. Baral, D. A. Esteves, C. M. Thomas, and R. A. Phaneuf A. L. D. Kilcoyne, "Confinement Resonances in Photoionization of Xe@C+60," *Phys. Rev. Lett.*, vol. 105, 2010.

[12] A. V. Korol, and A. V. Solov'yov S. Lo, "Dynamical screening of an endohedral atom," *Phys. Rev. A*, vol. 79, 2009.

[13] A. S. Baltenkov, and L.V. Chernycheva M.Ya. Amusia, "Photoionization of the subvalent subshells of noble gas endohedrals: interference of three resonances," *J. Phys. B*, vol. 41, 2008.

[14] V. K. Dolmatov and S. T.Manson, "Correlation confinement resonances in photoionization of endohedral atoms: Xe@C60," *J. Phys. B*, vol. 40, 2008.

[15] A. J. Siji, and P. C. Deshmukh, K. Govil, "Relativistic and confinement effects in photoionization of Xe," *J. Phys. B*, vol. 42, 2009.

[16] G. Fronzoni, D. Toffoli, P. Colavita, S. Furlan, and P. Decleva M. Stener, "Valence and core photoemission in M@C60 (M = Be, Mg, Ca)," *J. Phys. B*, vol. 35, 2002.

[17] H. S. Chakraborty, J. M. Rost, and S. T. Manson M. E. Madjet, "Ionization of C60 by fast bare-ion impact," *J. Phys. B*, vol. 41, 2008.

[18] Z. Chen A.Z.Msezane, "Effect of C60 giant resonance on the photoabsorption of encaged atoms," *Phys. Rev. A*, vol. 86, 2012.

[19] C.J.Joachain, *Quantum Collision Theory*.: North-Holland Publishing, September 1975.

[20] P.C.Deshmukh J.Libby, "Symmetry Principles and Conservation," *Resonance*, vol. 15, 2010.

[21] G. Breit H.A. Bethe, "Ingoing Waves in Final State of Scattering Problems," *Phys. Rev.*, vol. 93, 1954.

[22] U. Fano A.R.P. Rau, *Theory of Atomic Collisions and Spectra*.: Academic Press, 1986.

[23] H.A.Bethe E.E. Salpeter, *Quantum Mechanics of One and Two Electron Atoms*.: Plenum Pub. Corp., 1997.

[24] J.J.Sakurai, *Modern Quantum Mechanics*.: Pearson Education Inc., 1994.

[25] Bransden Joachain, *Physics of Atoms and Molecules*.: Prentice Hall, 2003.

[26] H. S. Chakraborty, P. C. Deshmukh, Steven T. Manson, O. Hemmers, P. Glans, D. L. Hansen, H. Wang, S. B. Whitfield, D. W. Lindle, R. Wehlitz, J. C. Levin, I. A. Sellin, and R. C. C. Perera E. W. B. Dias, "Breakdown of the Independent Particle Approximation in High-Energy Photoionization," *Phys. Rev. Lett.*, vol. 78, 1997.

[27] O. Hemmers, H. Wang, D. W. Lindle, I. A. Sellin, H. S. Chakraborty, P. C. Deshmukh and S. T. Manson D. L. Hansen, "Validity of the independent particle approximation: The exception, not the rule," *Phys.Rev. A*, vol. 60, 1999.

[28] J. Cooper R.N. Zare, "Angular distribution of photoelectrons," *J. Chem. Phys.*, vol. 48, 1968.

[29] P. Hohenberg W. Kohn, "Inhomogeneous Electron Gas," *Phys. Rev.*, vol. 136, 1964.

[30] L. H. Thamos, "The calculation of atomic fields," *Proc. Cambridge Phil.*, vol. 23, 1927.

[31] E.Fermi, "Un Metodo Statistico per la Determinazione di alcune Prioprietà dell'Atomo," *Rend. Accad. Naz. Lincei*, vol. 6, 1927.

[32] C.F.VonWeizsacker, "Zur Theorie der Kernmassen," *Z. Phys.*, vol. 96, 1935.

[33] Viraht Sahni, Manoj k. Harbola, Rejeev K. Pathak John P. Perdew, "Fourth-order gradient expansion of the fermion kinetic energy: Extra terms for nonanalytic densities," *Phys. Rev. B*, vol. 34, 1986.

[34] L. J. Sham W. Kohn, "Self-Consistent Equations Including Exchange and Correlation Effects," *Phys. Rev.*, vol. 140, 1965.

[35] S. Lundqvist N. H. March, *Inhomogeneous Electron Gas*. New York: Plenum Press, 1983.

[36] A.D.Buckingham, "Permanent and induced molecular moments and long-range intermolecular forces," *Adv. Chem. Phys.*, vol. 12, 1967.

[37] C.Flytzanis, *Quantum Electronics: A Treatise*. New York: Academic Press, 1975.

[38] W. Richter Y. R. Shen, *The Principles of Nonlinear Optics*. New York: John Wiley & Sons, 1984.

[39] S. T. Epstein, M. Karplus P. W. Langhoff, "Aspects of Time-Dependent Perturbation Theory," *Rev. Mod. Phys*, vol. 44, 1972.

[40] M.J. Giannoni, and M. Veneroni D. M. Brink, "Derivation of an adiabatic time-dependent Hartree-Fock formalism from a variational principle," *Nuclear Physics A*, vol. 258, 1976.

[41] W. Kohn E. K. U. Gross, "Local density-functional theory of frequency-dependent linear response," *Phys. Rev. Lett.*, vol. 55, 1985.

[42] Gerald D. Mahan, *Many-Particle Physics*. New York: Plenum Publishers, 1990.

[43] C.O. Almbladh U. von Barth, "Exact results for the charge and spin densities, exchange-correlation potentials, and density-functional eigenvalues," *Phys. Rev. B*, vol. 31, 1985.

[44] A. Zangwill Paul Soven, "Density-functional approach to local-field effects in finite systems: Photoabsorption in the rare gases," *Phys. Rev. A*, vol. 21, 1980.

[45] G. Senatore K. R. Subbaswamy, "Density dependence of the dielectric constant of rare-gas crystals," *Phys. Rev. B*, vol. 34, 1986.

[46] T. Renger, D. E. Hopper, M. A. McCune, H. S. Chakraborty, Jan-M. Rost, and S. T. Manson M. E. Madjet, "Photoionization of Xe inside C60: Atom-fullerene hybridization, giant cross-section enhancement, and correlation confinement resonances," *Phys. Rev.A*, vol. 81, 2010.

[47] H. S. Chakraborty, and S. T. Manson M. E. Madjet, "Giant Enhancement in Low Energy Photoemission of Ar Confined in C60," *Phys. Rev. Lett.*, vol. 99, 2007.

[48] M. E. Madjet, J. M. Rost, and S. T. Manson H. S. Chakraborty, "Dynamical Effects of Confinement on Atomic Valence Photoionization in Mg@C60," *Phys. Rev. A*, vol. 78, 2008.

[49] M. R. McCreary, A. B. Patel, M. E. Madjet, H. S. Chakraborty, and S. T. Manson M. H. Javani, "Valence photoionization of small alkaline earth atoms endohedrally confined in C60," *Eur. Phys. J. D*, vol. 189, 2012.

[50] M. E. Madjet, T. Renger, Jan-M. Rost, and S. T. Manson H. S. Chakraborty, "Photoionization of hybrid states in endohedral fullerenes," *Phys. Rev. A*, vol. 79, 2009.

[51] M. J. Puska R.M.Nieminen, "Photoabsorption of atoms inside C60," *Phys. Rev. A*, vol. 47, 1993.

[52] O. Gunnerson B.Lundqvist, "Exchange and correlation in atoms, molecules, and solids by the spin-density-functional formalism," *Phys. Rev. B*, vol. 13, 1976.

[53] R. Hentges, U. Becker, H. S. Chakraborty, M. E. Madjet, and J. M. Rost A. Rüdel, "Imaging delocalized electron clouds: Photoionization of C60 in Fourier reciprocal space," *Phys. Rev. Lett.*, vol. 89, 2002.

[54] V. K. Dolmatov and S. T. Manson J.P. Connerade, "On the nature and origin of confinement resonances," *J. Phys. B*, vol. 33, 2000.

[55] M. Q. Tan and U. Brcker Y. B. Xu, "Oscillations in the Photoionization Cross Section of C60," *Phys. Rev, Lett.*, vol. 76, 1996.

[56] A.Baltenkov, "Resonances in the photoionization cross section of M@C60 endohedrals," *Phys. Lett. A*, vol. 254, 1999.

[57] A. S. Baltenkov and L. V. Chernysheva M. Ya. Amusia, "Photoionization of the subvalent subshells of noble gas endohedrals: interference of three resonances," *J. Phys. B* , vol. 41, 2008.

[58] R. F. Reilman S.T.Manson, "Photoabsoption cross section for positive atomic ions with Z equal to or less than 30," *Ap. J. Supp.*, vol. 40, 1979.

[59] J. H. Hubbell and J. H. Scofield E. B. Saloman, "X-ray attenuation cross sections for energies 100 eV to 100 keV and elements Z = 1 to Z = 92," *At. Data Nuc. Data Tab. 38*, vol. 1, 1998.

[60] U.Fano, "Effects of Configuration Interaction on Intensities and Phase Shifts," *Phys. Rev.*, vol. 124, 1961.

[61] J.W.Cooper, "Photoionization from Outer Atomic Subshells. A Model Study," *Phys. Rev.*, vol. 128, 1962.

[62] A.F.Starace, "Theory of Atomic Photoionization," *Handbuch der Physik*, vol. 31, 1982.

[63] M.Amusia, *Atomic Photoeffect*. New York: Plenum, 1990.

[64] V.Schmidt, "Photoionization of atoms using synchrotron radiation," *Rep. Prog. Phys.*, vol. 55, 1992.

[65] S. T. Manson J.W.Cooper, "Photoionization in the Soft X-Ray Range : Z-Dependence in a Central Potential Model," *Phys. Rev.*, vol. 165, 1968.

[66] A. V. Korol A.V.Solov'yev, "Confinement resonances in the photoionization of endohedral atoms: myth or reality?," *J. Phys. B*, vol. 43, 2010.

[67] M. A. McCune, R. De, M. E. Madjet, H. S. Chakraborty A. Potter, "Probing photoelectron multiple-interferences via Fourier spectroscopy in energetic photoionization of Xe@C60," *Phys. Rev. A*, vol. 82, 2010.

[68] M. E. Madjet, H. S. Chakraborty M. A. McCune, "Reflective and collateral photoionization of the atom in a fullerene: Confinement geometry from reciprocal spectra," *Phys. Rev. A*, vol. 80, 2009.

[69] H. Steger, J. de Vries, B. Weisser, C. Menzel, B. Kamke, and W. Kamke I. V. Hertel, "Giant plasmon excitation in free C60 and C70 molecules studied by photoionization," *Phys. Rev. Lett.*, vol. 68, 1992.

[70] A.Bulgac, D.Tománek, and Y. Wang G.F.Bertsch, "Collective plasmon excitations in C60 clusters," *Phys. Rev. Lett.*, vol. 67, 1991.

[71] J. A. Alonso, J. M. López and M. J. Stott A. Rubio, "Surface plasmon excitations in C60, C60K and C60H clusters.," *Physica B*, vol. 183, 1993.

[72] R. A. Broglia, H. E. Roman, L. Serra, G. Colo and J. M. Pacheco F. Alasia, "Single-particle and collective degrees of freedom in C60," *J. Phys. B*, vol. 27, 1994.

[73] Göran Wendin B.Wästberg, "Many-electron effects in BaC60: Collective response and molecular effects in optical conductivity and photoionization," *Phys. Rev. B*, vol. 48, 1993.

[74] G.Y.Kashenock, R.G.Polozkov and I.A.Solov'yov V.K.Ivanov, "Photoionization cross sections of the fullerenes C20 and C60 calculated in a simple spherical model," *J. Phys. B*, vol. 34, 2001.

[75] V.K.Ivanovand A.V. Solov'yov R.G.Polozkov, "Photoionization of the fullerene ion C+60," *J. Phys. B*, vol. 38, 2005.

[76] S. Korica, G. Prumper, J. Viefhaus, K. Godehusen, O. Schwarzkopf, M. Mast, U. Becker A. Reinkoster, "The photoionization and fragmentation of C60 in the energy range 26–130 eV," *J. Phys. B.*, vol. 37, 2004.

[77] Mohammad H. Javani, Ruma De, Mohamed E. Madjet, Himadri S. Chakraborty, and Steven T. Manson Jaykob N. Maser, "Atom-fullerene-hybrid photoionization mediated by coupled d states in Zn@C60," *Phys. Rev. A*, vol. 86, 2012.

[78] Hongming Weng, Jinming Dong Hong Liu, "Electronic structure and symmetry of small clusters C28," *Journal of Molecular Structure (Theochem)*, vol. 671, 2004.

[79] M. Chen, Q. Zhang, Y.N. Chiu, S.-T. Lai M.Lin, "Ab initio study on fullerene C44 and its hydrogenates," *Electronic Journal of Theoretical Chemistry*, vol. 2, 1997.

[80] J.Boo, "An Introduction to Fullerene Structures," *J. Chem. Education*, vol. 69, 1992.

[81] M.E.Madjet Hervieux, "Many-body effects and autoionization resonances in photoionization of simple metal clusters," *Eur. Phys. J. D*, vol. 9, 1999.

[82] H.S.Chakrabortyand J.M.Rost M.E.Madjet, "Spurious oscillations from local self-interaction correction in high-energy photoionization calculations for metal clusters," *J. Phys. B*, vol. 34, 2001.

[83] E.Salpeter H.A.Bethe, *Quantum Mechanics of One and Two-Electron Atoms*. Berlin: Springer, 1958.

[84] J. Zobeley, and F. Tarantelli L.S. Cederbaum, "Giant Intermolecular Decay and Fragmentation of Clusters," *Phys. Rev. Lett.*, vol. 79, 1997.

[85] O. Kugeler, U. Hergenhahn, and T. Möller S. Marburger, "Experimental Evidence for Interatomic Coulombic Decay in Ne Clusters," *Phys. Rev. Lett.*, vol. 90, 2003.

[86] P.V. Demekhinb, P. Kolorenc, S. Scheitd, S.D. Stoycheve, A.I. Kuleff, Y.-C. Chiange, K. Gokhberge, S. Kopelkee, N. Sisourate, and L.S. Cederbaume V. Averbukh, "Interatomic electronic decay processes in singly and multiply ionized clusters," *J. Electr. Spectr. Relat. Phenom.*, vol. 183, 2011.

[87] U.Hergenhahn, "Interatomic and intermolecular coulombic decay: The early years," *J. Electr. Spectr. Relat. Phenom.*, vol. 184, 2011.

[88] A. Czasch, M.S. Schoffler, S. Schossler, A. Knapp, M.Kasz, J. Titze1, C. Wimmer, K. Kreidi, R.E. Grisenti, A. Staudte, O. Jagutzki, U. Hergenhahn, H. Schmidt-Bocking, and R. Dorner T. Jahnke, "Experimental Observation of Interatomic Coulombic Decay in Neon Dimers," *Phys. Rev. Lett.*, vol.

93, 2004.

[89] M. Tchaplyguine, M. Lundwall, R. Feifel, H. Bergersen, T. Rander, A. Lindblad, J. Schulz, S. Peredkov, S. Barth, S. Marburger, U. Hergenhahn, S. Svensson, and O. Björneholm G. Öhrwall, "Femtosecond Interatomic Coulombic Decay in Free Neon Clusters: Large Lifetime Differences between Surface and Bulk," *Phys. Rev. Lett.*, vol. 93, 2004.

[90] G.A. Grieves T.M.Orlando, "Intermolecular Coulomb Decay at Weakly Coupled Heterogeneous Interfaces," *Phys. Rev. Lett.*, vol. 107, 2011.

[91] H. Sann, T. Havermeier, K. Kreidi, C. Stuck, M. Meckel, M. Sch¨offler, N. Neumann, R. Wallauer, S.Voss, A. Czasch, O. Jagutzki, A. Malakzadeh, F. Afaneh, Th. Weber, H. Schmidt-Bocking, and R. Dorner T. Jahnke, "Ultrafast energy transfer between water molecules," *Nat. Phys.*, vol. 6, 2010.

[92] M. Braune, S. Barth, M. F¨orstel, T. Lischke, V. Ulrich, T. Arion, U. Becker, A. Bradshaw, and U. Hergenhahn M. Mucke, "A hitherto unrecognized source of low-energy electrons in water," *Nat. Phys.*, vol. 6, 2010.

[93] E. Ripani, P. Bolognesi, M. Coreno, M. Devetta, C. Callegari, M. Di Fraia, K.C. Prince, R. Richter, M. Alagia, A. Kivimaki, and L. Avaldi P. O'Keeffe, "The Role of the Partner Atom and Resonant Excitation Energy in Interatomic Coulombic Decay in Rare Gas Dimers," *Phys. Chem.Lett.*, vol. 4, 3013.

[94] H. Fukuzawa, K. Sakai, S. Mondal, E. Kukk, Y. Kono, S.Nagaoka, Y. Tamenori, N. Saito, K. Ueda M. Kimura, "Efficient Site-specific Low-energy Electron Production via Interatomic Coulombic Decay Following Resonant Auger Decay," *Phys. Rev. Lett.*, vol. 90, 2003.

[95] R. Santra L.S.Cederbaum, "Coulombic Energy Transfer and Triple Ionization in Clusters," *Phys. Rev. Lett.*, vol. 90, 2003.

[96] K. Gokhberg, S. Kopelke, and L. S. Cederbaum A. I. Kuleff, "Ultrafast Interatomic Electronic Decay in Multiply Excited Clusters," *Phys. Rev. Lett.*, vol. 105, 2010.

[97] J. B. Williams, M. Weller, M. Waitz, M. Pitzer, J. Voigtsberger, C. Schober, G. Kastirke, C. Müller, C. Goihl, P. Burzynski, F. Wiegandt, T. Bauer, R. Wallauer, H. Sann, A. Kalinin, L. Ph. H. Schmidt, M. Schöffler, N. Sisourat, and T. Jahnke F. Trinter, "Evolution of Interatomic Coulombic Decay in the Time Domain," *Phys. Rev. Lett.*, vol. 111, 2013.

[98] A. Senftleben, M. Kurka, A. Rudenko, L.Foucar, G. Schmid, A. Broska, T. Pfeifer, K. Meyer, D.Anielski, R. Boll, D. Rolles, M. K¨ubel, M.F. Kling, Y.H.Jiang, S. Mondal, T. Tachibana, K. Ueda, T. Marchenko,M. Simon, G. Brenner, R. Treusch K. Schnorr, "Time-Resolved Measurement of Interatomic Coulombic Decay in Ne2," *Phys. Rev. Lett.*, vol. 111, 2013.

[99] P. Kolorenc, A. I. Kuleff, and L. S. Cederbaum K. Gokhberg, "A new intermolecular mechanism to selectively drive photoinduced damages," *arXiv:1303.6440 [physics.atm-clus]*.

[100] S. Joshi, S. Marbuger, V. Ulrich, A. Lindblad,G. Ohrwall, O. Bj omeholm, and U. Hergenhahn S. Barth, "Quasirelativistic theory equivalent to fully relativistic theory," *J. Chem. Phys.*, vol. 2005, 122.

[101] K. Ito, Y. Hikosaka, E. Shigemasa, F. Penent, and P. Lablanquie T. Aoto, "Properties of Resonant Interatomic Coulombic Decay in Ne Dimers," *Phys. Rev. Lett.*, vol. 97, 2006.

[102] H. Gassert, M. S. Schöffler, J. N. Titze, M. Waitz, J. Voigtsberger, F. Trinter, J. Becht, A. Kalinin, N. Neumann, C. Zhou, L. Ph. H. Schmidt, O. Jagutzki, A. Czasch, H. Merabet, H. Schmidt-Böcking, T. Jahnke, A. Cassimi, and R. Dörner H.K. Kim, "Ion-impact-induced interatomic Coulombic decay in neon and argon dimers," *Phys. Rev. A*, vol. 88, 2013.

[103] V. Averbukh, and L.S. Cederbaum K. Gokhberg, "Interatomic decay of inner-valence-excited states in clusters," *J. Chem. Phys.*, vol. 142, 2006.

[104] J. B. Williams, M. Weller, M. Waitz, M. Pitzer, J. Voigtsberger, C. Schober, G. Kastirke, C. Müller, C. Goihl, P. Burzynski, F. Wiegandt, R. Wallauer,A. Kalinin, L. Ph. H. Schmidt, M. S. Schöffler, Y.-C. Chiang, K. Gokhberg, T. Jahnke F. Trinter, "Vibrationally resolved decay width of Interatomic Coulombic Decay in HeNe," *arXiv:1310.6538v2 [physics.atm-clus]*.

[105] A.B. Voitkiv, and C. Muller B. Najjari, "Two-Center Resonant Photoionization," *Phys. Rev. Lett.*, vol. 105, 2010.

[106] S. Yang, and L. Dunsch A.A. Popov, "Endohedral Fullerenes," *Chem. Rev.*, vol. 113, 2013.

[107] Vitali Averbukh and L.S.Cederbaum, "Interatomic Electronic Decay in Endohedral Fullerenes," *Phys. Rev. Lett.*, vol. 96, 2006.

[108] A.V. Korol A.V.Solov'yov, "Vacancy decay in endohedral atoms: the role of an atom's non-central position," *J. Phys. B*, vol. 44, 2011.

[109] M.Ya. Amusia A. Baltenkov, "Vacancy decay in endohedral atoms," *Phys. Rev. A 73*, vol. 73, 2006.

[110] A.P. Seitsonen, S. Ito, H. Takagi, N. Dragoe,and T. Greber M. Morscher, "Strong 3p-T1u hybridization in Ar@C60," *Phys. Rev. A*, vol. 82, 2010.

[111] L. Novotny N. van Hulst, "Antennas for light," *Nature Photonics*, vol. 5, 2012.

[112] A. Mandal, S. Saha, A. S. Kheifets, V. K. Dolmatov and S. T. Manson P. C. Deshmukh, "Attosecond time delay in the photoionization of endohedral atoms A@C60: A new probe of confinement

resonances," *Phys. Rev. A*, vol. 89, 2014.

APPENDICES

Appendix A

We want to solve the equation (1.14),

$$R'' + \frac{2}{r}R' - \frac{l(l+1)}{r^2}R + \frac{2\mu}{r^2}[E - V(r)]R = 0 \quad \textbf{(A.1)}$$

$$R_{kl}(r) = \frac{y_{kl}(r)}{r} \quad \textbf{(A.2)}$$

$$\left[-\frac{\hbar^2}{2m}\frac{d^2}{dr^2} + \left\{V(r) + \frac{1}{2m}\frac{l(l+1)}{r^2}\right\} - E\right] y_{kl}(r) = 0 \quad \textbf{(A.3)}$$

$$\left[\frac{d^2}{dr^2} + k^2 - U(r) - \frac{l(l+1)}{r^2}\right] y_{kl}(r) = 0 \qquad , \qquad U(r) = \frac{2mV(r)}{\hbar^2} \quad \textbf{(A.4)}$$

$$\left[\frac{d^2}{dr^2} + k^2 - U_l^{effective}(r)\right] y_{kl}(r) = 0 \qquad , \qquad U_l^{effective}(r) = U(r) + \frac{l(l+1)}{r^2} \quad \textbf{(A.5)}$$

As $r \to \infty$ any physical scattering potential will become very weak. And the question is that, what do we mean by weak?

Assuming the potential is weak then the solution for (A.4) can be written as,

$$y_{kl}(r) = F_l(k,r)e^{\pm ikr} \quad \textbf{(A.6)}$$

And in this assumption $F_l(k,r)$ is weakly depend on *r*. Now by substituting (A.6) in (A.5) we can have,

$$F''_r(k,r) \pm 2ikF'_l(k,r) - U_l^e(r)F_l(k,r) = 0 \quad \textbf{(A.7)}$$

$$\frac{F''_l(k,r)}{F_l(k,r)} \pm 2ik\frac{F'_l(k,r)}{F_l(k,r)} = U_l^e(r) \quad \textbf{(A.8)}$$

And because $F_l(k,r)$ is weakly depend on *r* the first term can is negligible so,

$$\frac{F'_l(k,r)}{F_l(k,r)} \sim \frac{1}{\pm 2ik}U_l^e(r) \quad \textbf{(A.9)}$$

$$F_l(k,r) = e^{\frac{1}{\pm 2ik}\int U_l^e(r)dr} \quad \textbf{(A.10)}$$

Now we can see how weak the potential should be: If the *V*(r) is Coulomb potential which means $U_l^e(r \to \infty) \to \frac{1}{r}$, then the $F_l(k,r)$ would not be independent on *r*, which means this method is not working for Coulomb potential, but it works for all potentials that in the asymptotic region go to zero faster than Coulomb potential.

So the potential should have this form,

$$U(r \to \infty) \to \frac{M}{r^{1+\varepsilon}} \quad , \quad M \text{ is constant and } \varepsilon > 0 \tag{A.11}$$

Since $F_l(k,r)$ is nearly constant we can write,

$$y_l(k,r) = F_l(k,r)e^{\pm ikr} = B_l^{(1)}(k)e^{+ikr} + B_l^{(2)}(k)e^{-ikr} \tag{A.12}$$

$$y_l(k,r \to \infty) \to c_1 \cos\left(kr - \frac{l\pi}{2}\right) + c_2 \sin\left(kr - \frac{l\pi}{2}\right) \tag{A.13}$$

Finally, we can have,

$$y_r(k,r \to \infty) \to A_l(k) \sin\left(kr - \frac{l\pi}{2} + \delta_l(k)\right) \tag{A.14}$$

$$R_l(r \to \infty) \to A_l(k) \frac{\sin\left(kr - \frac{l\pi}{2} + \delta_l(k)\right)}{r} \tag{A.15}$$

And in terms of spherical outgoing wave and ingoing wave we have,

$$R_l(r \to \infty) \to A_l(k) \frac{e^{i\left(kr - \frac{l\pi}{2} + \delta_l(k)\right)} - e^{-i\left(kr - \frac{l\pi}{2} + \delta_l(k)\right)}}{2ir} \tag{A.16}$$

Appendix B

In (30) there are linear term and quadratic term,

$$H_{linear} = -\frac{iq\hbar}{mc}\vec{A}(\vec{r},t).\nabla \tag{B.1}$$

$$H_{quadratic} = \frac{q^2}{2mc^2}(\vec{A}(\vec{r},t))^2 \tag{B.2}$$

The ratio of the quadratic term to linear term would be,

$$\frac{H_{quadratic}}{H_{linear}} \sim \frac{q^2A^2}{2mc^2}\frac{mc}{iq\hbar A} = \frac{qA}{2cp} \quad \textbf{(B.3)}$$

For small field quadratic term is much weaker than linear term.

Appendix C

Calculating the number of degenerate states:

If we consider three orthogonal axes of n_x, n_y, n_z.

The number of states in the unit of volume in this coordinate will be,

$$dN = n^2 dn\, d\Omega \quad \textbf{(C.1)}$$

And each of these states will contribute to the transition $i \to f$, with the same matrix element, $\left\langle f\left|e^{i\vec{k}.\vec{r}}\hat{\varepsilon}.\vec{\nabla}\right|i\right\rangle$. To find this number we use Box Normalization, and Born Von Karman boundary condition. In the box with the length L how many wavelength can be fit.

$$n_x\lambda_x = L \to\ n_x\frac{2\pi}{k_x} = L \to\ k_x = \frac{2\pi n_x}{L} \qquad \text{for x axis} \quad \textbf{(C.2)}$$

$$E = \frac{\hbar^2k^2}{2m} = \frac{\hbar^2}{2m}\left(k_x^2 + k_y^2 + k_z^2\right) = \frac{\hbar^2}{2m}(\frac{2\pi}{L})^2\left(n_x^2 + n_y^2 + n_z^2\right) = \frac{\hbar^2}{2m}(\frac{2\pi}{L})^2n^2 \quad \textbf{(C.3)}$$

The number of states in volume element is,

$$dN = n^2 dn\, d\Omega = n^2\frac{dn}{dE}\, dE\, d\Omega \quad \textbf{(C.4)}$$

From (C.3) we can find $\frac{dn}{dE}$,

$$\frac{dn}{dE} = \frac{mL^2}{4\pi^2\hbar^2}\frac{1}{n} = \frac{m}{\hbar^2k}\frac{L^2}{4\pi^2}\frac{k}{n} \quad \textbf{(C.5)}$$

For free electron,

$$k = \left(\frac{2mE}{\hbar^2}\right)^{1/2} \to\ \frac{dk}{dE} = \frac{m}{\hbar^2k} \quad \textbf{(C.6)}$$

So,

$$\frac{dn}{dE} = \frac{dk}{dE}\frac{L^2}{4\pi^2}\frac{k}{n} \quad \textbf{(C.7)}$$

From (C.3), $\frac{k}{n}$ can be calculated and substituted in (C.7),

$$\frac{k}{n} = \frac{2\pi}{L} \tag{C.8}$$

$$\frac{dn}{dE} = \frac{dk}{dE}\frac{L}{2\pi} \tag{C.9}$$

The number of states in volume element can be determined by substituting (C.8) and (C.9) in (C.1),

$$dN = \left(\frac{L}{2\pi}\right)^3 \left(\frac{mk}{\hbar^2}\right) dE d\Omega \tag{C.10}$$

Now the degenerate states should be calculated and added up,

$$\left[\frac{d\sigma}{d\Omega}\right]_{\hat{k}_f}^{\hat{\varepsilon}} = \int \frac{4\pi^2 \alpha \hbar^3}{m^2 \omega} \left|\left\langle f \left| e^{i\vec{k}.\vec{r}}\, \hat{\varepsilon}.\vec{\nabla} \right| i \right\rangle\right|^2 \delta(E - E_{fi})\, dN dE \tag{C.11}$$

Finally,

$$\left[\frac{d\sigma}{d\Omega}\right]_{\hat{k}_f}^{\hat{\varepsilon}} = \frac{4\pi^2 \alpha \hbar^3}{m^2 \omega_{fi}} \left|\left\langle f \left| e^{i\vec{k}.\vec{r}}\, \hat{\varepsilon}.\vec{\nabla} \right| i \right\rangle\right|^2 \left(\frac{L}{2\pi}\right)^3 \left(\frac{mk}{\hbar^2}\right) \tag{C.12}$$

Appendix D

By having the definition for Dirac delta function and Oscillator strength,

$$\delta(\omega_{0,s} - \omega) = \lim_{\Gamma_d \to 0} \frac{1}{2\pi} \frac{\frac{\Gamma_d}{2}}{\left((\omega_{0,s} - \omega)^2 - \left(\frac{\Gamma_d}{2}\right)^2\right)} \tag{D.1}$$

$$\int_0^\infty \frac{df}{d\omega} d\omega = \int_0^\infty 2\delta(\omega_{0,s} - \omega) d\omega \tag{D.2}$$

Or,

$$\int_0^\infty \frac{df}{d\omega} d\omega = \frac{1}{2} \int_{-\infty}^\infty 2\delta(\omega_{0,s} - \omega) d\omega = \int_{-\infty}^\infty \delta(\omega_{0,s} - \omega) d\omega = 1 \tag{D.3}$$

Appendix E

Form (2.57)

$$f_{fi} = \frac{2m\omega_{fi}}{\hbar}|\langle f|r_k|i\rangle|^2 \quad \textbf{(E.1)}$$

$$f_{fi}^{x} = \frac{2m\omega_{fi}}{3\hbar}|\langle f|x|i\rangle|^2 \quad \textbf{(E.2)}$$

By using (2.66) the (E.2) can be written in two forms,

$$f_{fi}^{x} = \frac{2m\omega_{fi}}{3\hbar}\langle i|x|f\rangle\langle f|x|i\rangle = \frac{2i}{3\hbar}\langle i|p_x|f\rangle\langle f|x|i\rangle \quad \textbf{(E.3)}$$

$$f_{fi}^{x} = \frac{2m\omega_{fi}}{3\hbar}\langle i|x|f\rangle\langle f|x|i\rangle = -\frac{2i}{3\hbar}\langle i|x|f\rangle\langle f|p_x|i\rangle \quad \textbf{(E.4)}$$

Now we can write oscillator strength as sum of these two terms,

$$f_{fi}^{x} = \frac{1}{2}\left(\frac{2i}{3\hbar}\langle i|p_x|f\rangle\langle f|x|i\rangle\right) + \frac{1}{2}\left(-\frac{2i}{3\hbar}\langle i|x|f\rangle\langle f|p_x|i\rangle\right) \quad \textbf{(E.5)}$$

If we sum over all final states,

$$\sum_f f_{fi}^{x} = \sum_f \frac{1}{2}\left(\frac{2i}{3\hbar}\langle i|p_x|f\rangle\langle f|x|i\rangle\right) + \frac{1}{2}\left(-\frac{2i}{3\hbar}\langle i|x|f\rangle\langle f|p_x|i\rangle\right) = \frac{1}{3} \quad \textbf{(E.6)}$$

And add three components of x, y, and z,

$$\sum_f f_{fi} = 1 \quad \textbf{(E.7)}$$

Appendix F

In uniform 3 dimension system of spin ½ Fermions, the Fermi momentum k_F is related to the density by the following relation,

$$\left(\frac{4\pi}{3}k_F^3\right)\Big/\left(\frac{(2\pi)^3}{\Omega}\right) = \frac{N}{2} \quad \rightarrow \quad 3\pi^2 n = k_f^3 \quad \textbf{(F.1)}$$

The kinetic energy of this system is,

$$T = \sum_{k<k_F}\sum_{\sigma}\frac{\hbar^2k^2}{2m} = 2\frac{\Omega}{(2\pi)^3}\int_0^{k_F} 4\pi k^2 dk\ \frac{\hbar^2k^2}{2m} = \frac{\Omega}{\pi^2}\frac{\hbar^2}{10m}k_F^5 \quad \textbf{(F.2)}$$

And the total number of the fermions would be,

$$N = \sum_{k<k_F} \sum_{\sigma} 1 = 2\frac{\Omega}{(2\pi)^3}\int_0^{k_F} 4\pi k^2 dk \ = \frac{\Omega}{3\pi^2}k_F^3 \quad \textbf{(F.3)}$$

So by substituting (F-3) and (F-1) in (F-2) the kinetic energy per unit of volume or per particle for uniform system can be calculated as follows,

$$T = \Omega\frac{3}{5}\frac{\hbar^2 k_F^2}{2m}\ n = N\frac{3}{5}\frac{\hbar^2 k_F^2}{2m} \quad \textbf{(F.4)}$$

But for non-uniform system where the density is a function of position $n(\vec{r})$, we can have the same relation as (F-1) with position-dependent the Fermi momentum,

$$n(\vec{r}) = \frac{k_F^3(\vec{r})}{3\pi^2} \quad \textbf{(F.5)}$$

And the kinetic energy would be,

$$T[n] = \int d^3r\ \frac{3}{5}\frac{\hbar^2 k_F^2(\vec{r})}{2m}\ n(\vec{r}) \quad \textbf{(F.6)}$$